

**MULTIPHYSICS DESIGN AND SIMULATION OF A TUNGSTEN-CERMET
NUCLEAR THERMAL ROCKET**

A Thesis

by

BRAD APPEL

Submitted to the Office of Graduate Studies of
Texas A&M University
in partial fulfillment of the requirements for the degree of

MASTER OF SCIENCE

August 2012

Major Subject: Nuclear Engineering

Multiphysics Design and Simulation of a Tungsten-Cermet Nuclear Thermal Rocket

Copyright 2012 Brad Appel

**MULTIPHYSICS DESIGN AND SIMULATION OF A TUNGSTEN-CERMET
NUCLEAR THERMAL ROCKET**

A Thesis

by

BRAD APPEL

Submitted to the Office of Graduate Studies of
Texas A&M University
in partial fulfillment of the requirements for the degree of

MASTER OF SCIENCE

Approved by:

Chair of Committee,	Karen Vierow
Committee Members,	Shannon Bragg-Sitton
	Paul Cizmas
Head of Department,	Yassin Hassan

August 2012

Major Subject: Nuclear Engineering

ABSTRACT

Multiphysics Design and Simulation of a Tungsten-Cermet Nuclear Thermal Rocket.

(August 2012)

Brad Appel, B.S., Purdue University

Chair of Advisory Committee: Dr. Karen Vierow

The goal of this research is to apply modern methods of analysis to the design of a tungsten-cermet Nuclear Thermal Rocket (NTR) core. An NTR is one of the most viable propulsion options for enabling piloted deep-space exploration. Concerns over fuel safety have sparked interest in an NTR core based on tungsten-cermet fuel. This work investigates the capability of modern CFD and neutronics codes to design a cermet NTR, and makes specific recommendations for the configuration of channels in the core.

First, the best CFD practices available from the commercial package Star-CCM+ are determined by comparing different modeling options with a hot-hydrogen flow experiment. Next, through grid convergence and sensitivity studies, numerical uncertainty is shown to be a small contributor to overall uncertainty; while fuel thermal conductivity, hydrogen specific heat, and fission energy deposition are found to have a large impact on simulation uncertainty. The model-form error is then estimated by simulation of a NERVA fuel element from an NRX-A6 engine test, where the peak temperature matches measured data to within 2.2%. Using a combination of Star-CCM+

and MCNP for neutronics, typical uncertainties are estimated at 3% for predicting fuel temperature, 2% for hydrogen temperature, and 5% for pressure.

The second part uses the aforementioned analysis methods in a parametric study to determine what coolant channel size and distribution is optimum for a 10 klbf-thrust cermet NTR core. By varying the channel diameter and pitch-to-diameter ratio (p/d), it is found that a diameter of 0.12 cm with a p/d of 1.8 results in the lightest core with a peak temperature of 2850 K. The study also shows that element-by-element mass flow rate zoning is the best method for handling radial power peaking. In addition, a detailed simulation of a cermet design developed at the Argonne National Laboratory shows that modifications to the historical fuel element design are required to avoid overheating.

The final part investigates the ability of Star-CCM+ to model fuel element failure modes. Through a combination of uncertainty quantification and a parametric analysis, this thesis ultimately lays a groundwork for future detailed design of cermet NTR fuel elements.

DEDICATION

To my father.

ACKNOWLEDGEMENTS

I would first like to thank my advisor, Dr. Karen Vierow, for her guidance and support throughout the research process. I owe many thanks to Dr. Shannon Bragg-Sitton for introducing me to the nuclear-space field, and supporting me in many endeavors over the past two years. I would also like to thank Dr. Jonathan Webb at the Idaho National Laboratory for his invaluable technical guidance, and James Werner for his advice and support. I am also thankful to Dr. Paul Cizmas for his help and technical advice. Finally, I would like to thank the many IT workers who make computational research possible, most notably Tami Grimmett at INL and Cory Hearnberger at Texas A&M.

TABLE OF CONTENTS

	Page
ABSTRACT	iii
DEDICATION	v
ACKNOWLEDGEMENTS	vi
TABLE OF CONTENTS	vii
LIST OF FIGURES.....	x
LIST OF TABLES	xiv
1. INTRODUCTION	1
1.1 Objectives	4
1.2 Significance of Work.....	5
2. NUCLEAR THERMAL ROCKET OVERVIEW	10
2.1 History.....	10
2.2 Conceptual Design	11
2.3 Motivation for the Cermet Fuel	14
2.4 Previous Cermet-NTR Development Programs.....	15
2.5 Historical Methods of Analysis.....	16
3 ANALYSIS METHODS	21
3.1 Parameters of Interest.....	21
3.2 Important Thermal-Fluid Phenomena	24
3.3 Operating Principles of Star-CCM+.....	27
3.4 Material Properties	29
3.4.1 Hydrogen Properties	29
3.4.2 Fuel Properties.....	36
3.5 Important Neutronics Phenomena.....	38
3.6 Operating Principle of MCNP.....	42
3.7 Method for Energy Deposition Calculation	44
3.8 Applications of New Method.....	47

	Page
4 UNCERTAINTY ASSESSMENT	50
4.1 CFD Uncertainty Quantification Methodology.....	51
4.1.1 Code Verification.....	52
4.1.2 Solution Verification	53
4.1.3 Input Sensitivity	56
4.1.4 Validation.....	57
4.2 Method Down-select Model	58
4.2.1 Mesh Type	66
4.2.2 Conformal versus Non-Conformal Mesh	68
4.2.3 Turbulence Model.....	69
4.3 Grid Convergence Assessment.....	75
4.3.1 Axial Coarsening	75
4.3.2 Grid Convergence Index.....	78
4.4 Sensitivity Coefficient Calculation.....	80
4.5 Validation Model.....	85
4.5.1 Model Setup.....	85
4.5.2 Model Results	90
4.5.3 Estimate of Model-Form Error	92
4.6 Neutronics Uncertainty Quantification.....	93
4.7 Overall Uncertainty Assessment	94
5 PARAMETRIC STUDY	96
5.1 Definitions	97
5.2 Review of Previous Parametric Studies.....	100
5.3 Design Space and Assumptions.....	102
5.3.1 Assumptions.....	102
5.3.2 Channel Configuration.....	105
5.3.3 MCNP Model.....	107
5.3.4 Rocket Performance Estimates	109
5.4 Results	113
5.4.1 Peaking Factor and Flow Rate Zones	113
5.4.2 Peak Fuel Temperatures.....	116
5.4.3 Pressure Drop.....	123
5.4.4 Core Mass	124
5.4.5 Effect of Enrichment Zoning	125
5.5 Application of Parametric Study to ANL-10k.....	131
5.5.1 Model Setup.....	131
5.5.2 MCNP Results	134
5.5.3 CFD Results.....	137

	Page
5.6 Channel Size Recommendation.....	141
6 MULTI-ELEMENT FAILURE MODE ANALYSIS	143
6.1 Important Failure Modes	143
6.2 Multi-Element Model	144
6.3 Results	146
7 CONCLUSIONS	150
REFERENCES	153
APPENDIX.....	158
VITA.....	184

LIST OF FIGURES

	Page
Figure 1.1	Mass ratio versus specific impulse for a typical Mars mission3
Figure 2.1	Conceptual drawing of a typical solid-core Nuclear Thermal Rocket..... 12
Figure 2.2	Typical fuel element cross section with 61 coolant channels 13
Figure 2.3	(a) Mesh from 1966 NASA study [21] (b) Mesh from 2007 study [22].... 18
Figure 3.1	Comparison of hydrogen Prandtl number from two different sources32
Figure 3.2	Specific heat at constant pressure (c_p) for hydrogen.....33
Figure 3.3	Thermal conductivity of hydrogen34
Figure 3.4	Dynamic viscosity of hydrogen35
Figure 3.5	Thermal conductivity of W-60v/oUO ₂ cermet fuel37
Figure 3.6	Thermal conductivity of W-UO ₂ fuel compared with NERVA fuel.....38
Figure 4.1	Overview of the contributing factors to simulation uncertainty50
Figure 4.2	Diagram of experiment from Taylor [34]60
Figure 4.3	Temperature polynomial for c_p of tungsten using data from Ref. [43].....61
Figure 4.4	Temperature regression for thermal conductivity of tungsten [43]62
Figure 4.5	Snapshot of temperature distribution in method down-select model64
Figure 4.6	Polyhedral mesh (left), tetrahedral mesh (center), and trimmer mesh (right) for the tungsten channel.67
Figure 4.7	Peak temperature as a function of average y^+ of cells at the wall73
Figure 4.8	The change in simulation results as a function of stretching factor77
Figure 4.9	Relative importance of input variables for calculating fuel temperature uncertainty82

	Page
Figure 4.10	Relative importance of input variables for calculating hydrogen temperature uncertainty 82
Figure 4.11	Relative importance of input variables for calculating pressure drop uncertainty 83
Figure 4.12	Relative importance of input variables for calculating fuel temperature uncertainty, large ΔT case 84
Figure 4.13	Typical placement of a fuel element thermocouple in the NRX-A6 test; cross-sectional view (left), and profile view (right) [35]..... 86
Figure 4.14	Extracted temperature measurements from the NRX-A6 final report 87
Figure 4.15	Snapshot of validation model temperature distribution 90
Figure 4.16	Comparison of measured and simulated axial temperature profiles for the NRX-A6..... 91
Figure 5.1	Analysis process for parametric study 96
Figure 5.2	Geometry of the triangular lattice unit cell 97
Figure 5.3	Variation of core critical mass with void fraction 99
Figure 5.4	Each of the nine cases applied to a 1.082" flat-to-flat fuel element 106
Figure 5.5	Snapshots of a typical MCNP case in the study. Profile view (left); Cross-section view (center); Channel zoom-in (right)..... 107
Figure 5.6	Radial zones used for MCNP5 mesh tally 109
Figure 5.7	Radial power profile normalized to average power 114
Figure 5.8	Axial power profile normalized to average power 115
Figure 5.9	Radial zone flow rate distribution for the ten-zone set of cases 116
Figure 5.10	Typical mesh snapshot from the parametric study 117
Figure 5.11	Typical temperature distribution in a subchannel cross section 117

	Page
Figure 5.12	Peak fuel temperatures for one mass flow rate zone 118
Figure 5.13	Peak fuel temperatures for element-by-element flow zoning 119
Figure 5.14	Peak fuel temperatures for channel-by-channel flow zoning 120
Figure 5.15	Peak fuel temperature as a function of SA/V 122
Figure 5.16	Pressure drop for the element-by-element data set 123
Figure 5.17	Mass of fuel as a function of p/d..... 125
Figure 5.18	Cross section view of radial enrichment zones (left); and zoom-in of zones (right)..... 127
Figure 5.19	²³⁵ U enrichment levels in radial zones..... 128
Figure 5.20	Radial power profiles for flat-enrichment and zoned-enrichment cases 129
Figure 5.21	SolidWorks model of an ANL-10k fuel element..... 131
Figure 5.22	Original reactor drawing (left); MCNP model cross section (right)..... 132
Figure 5.23	Zoom-in of a fuel element (top left); the reflector components (right) .. 133
Figure 5.24	Profile view of the MCNP ANL-10k model showing the movable radial reflector 133
Figure 5.25	SolidWorks snapshot of ANL-10k CFD model..... 134
Figure 5.26	R-Z profile of volumetric power deposition in the fuel..... 135
Figure 5.27	Calculated axial power profile (normalized to average power) for the ANL-10k 136
Figure 5.28	Axial temperature profiles for the ANL-10k 138
Figure 5.29	Transverse temperature distribution in the ANL-10k fuel element..... 140
Figure 6.1	Multi-element model for stress analysis 145
Figure 6.2	Equivalent solid stress in the failure mode model 147

Figure 6.3 Exaggerated displacement of fuel matrix and cladding..... 148

LIST OF TABLES

		Page
Table 1.1	Comparison of the abilities of different analysis techniques	7
Table 4.1	Experiment conditions used for benchmarking [26].....	60
Table 4.2	Simulation results for different power shape methods.....	65
Table 4.3	Simulation results for different mesh types	67
Table 4.4	Simulation results for a conformal and non-conformal mesh interface.....	69
Table 4.5	Simulation results for different turbulence models.....	71
Table 4.6	Percent errors from measurements for each turbulence model.....	72
Table 4.7	Simulation results for different axial stretching factors.....	76
Table 4.8	Simulations results for different base size refinements	78
Table 4.9	Order of accuracy, grid convergence index, and numerical uncertainty	79
Table 4.10	Simulation results for different variable perturbations	80
Table 4.11	Input uncertainties for each solution parameter for a set of assumed variable relative uncertainties.....	81
Table 4.12	Simulation inputs for validation model	89
Table 4.13	Uncertainties and errors in the validation model	92
Table 4.14	Typical total uncertainties for a large ΔT case	95
Table 5.1	Channel size and p/d for parametric study	105
Table 5.2	Critical dimensions for each channel configuration.....	108
Table 5.3	Comparison of calculated rocket performance with published calculations.....	112
Table 5.4	Performance requirements for the 10 klbf-thrust core	113
Table 5.5	Effect of combining flow and enrichment zoning for Case 5	130

	Page
Table 5.6 Comparison of results for ANL-10k	137
Table 5.7 Viable channel configurations for not exceeding a peak temperature of 2850 K.....	142
Table 6.1 Results for failure mode test case.....	146

1. INTRODUCTION

The goal of this thesis is to use modern analysis methods to provide insight into the design of Nuclear Thermal Rockets (NTRs), and to make recommendations for a safe fuel element design for a small-sized NTR.

This work is within the context of a transitioning time period for the United States in space exploration. In the post-shuttle era, we find ourselves on pause; unable to even launch our own astronauts into space, yet still in possession of the greatest collection of experts and knowhow in spaceflight that the world has ever known. There is hope that once again the political and financial resources of this country will compel NASA to push forward the limits of exploration, and there is hope that a new generation of visionary entrepreneurs can help expedite a new chapter.

One of the most logical targets for the next big era in space is Mars. To get there, we'll need to invent revolutionary technologies for propulsion and landing systems, life support, power generation, as well as for many other disciplines. The duration of the voyage itself, which can be anywhere from one to several years, will test the limits of the human psyche. Once we establish an outpost on the planet, there will be opportunities for developing exciting new strategies for living off the land – by using either the water frozen in the Martian soils or the CO₂ in its atmosphere to supply our closed-loop habitats or even produce rocket propellant. In the very long term, there are real possibilities for implementing climate change stimuli to the entire planet itself, in time

This thesis follows the style of the ASME Journal of Heat Transfer.

transforming Mars into a new Earth. The potential value of a robust manned exploration program is incalculable.

This thesis focuses on one of the key technologies that will be needed to undertake Martian (or any deep space) exploration - *interplanetary propulsion*. Travel from one orbit to another in the solar system is dictated by the amount of velocity change (“delta V”) needed to capture into a new orbit at different energy level. The ideal rocket equation, which is derived from the conservation of momentum, gives us a relationship between the delta V required for a mission, the capabilities of a propulsion system, and the required propellant mass that must be expended:

$$\frac{m_0}{m_f} = e^{\Delta v/v_e} \quad (1.1)$$

where m_0/m_f is the ratio of the initial to final spacecraft mass, v_e is the propulsion exhaust velocity, and Δv is the required velocity change. A quick look at this equation reveals the importance of exhaust velocity: Given some required Δv , the mass required to accomplish the mission decreases exponentially as the exhaust velocity increases. This is precisely where the topic of this thesis, the Nuclear Thermal Rocket (NTR), comes into play.

Figure 1.1 shows the result of the ideal rocket equation for a hypothetical Mars mission with a delta V of 6.60 km/s. On the horizontal axis is specific impulse of the propulsion system, which is a common way to describe exhaust velocity (specific impulse is the exhaust velocity divided by Earth’s gravitational acceleration). On the vertical axis is the ratio of the initial mass to the final mass of the vehicle, the difference being the propellant expended.

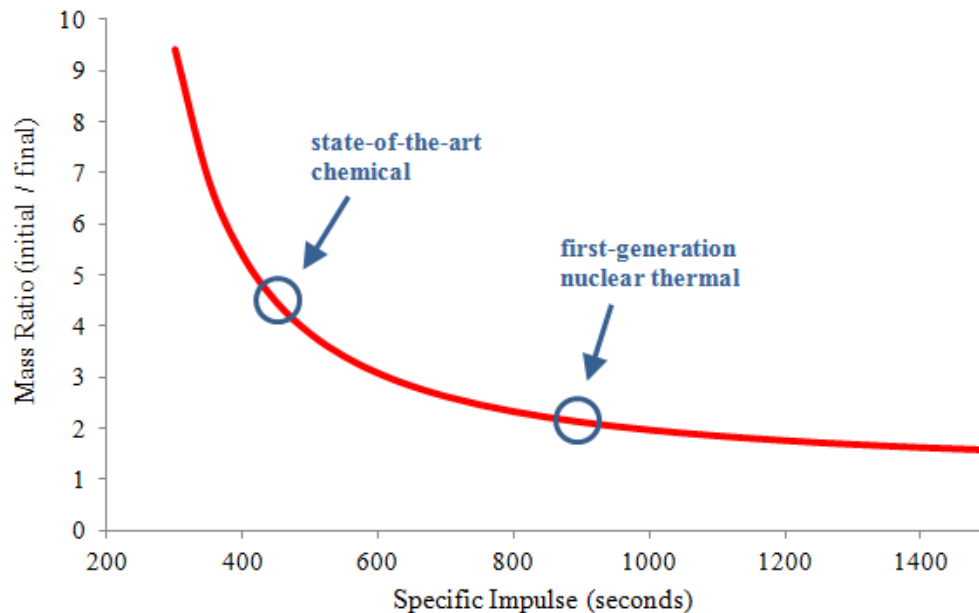


Fig. 1.1 Mass ratio versus specific impulse for a typical Mars mission

This exponential curve shows that a Mars mission with a chemical rocket will require about twice the propellant as a mission that uses a nuclear thermal rocket. This situation becomes amplified when the return trip is factored in as well. The best estimate for the number of Heavy Lift Launch Vehicle (HLLV) launches required to send a crew to Mars using chemical propulsion for the interplanetary transit is twelve [1]. If NTRs are used instead, the number of required HLLVs drops down to seven [2]. Considering that the Saturn V (the only HLLV that ever existed) cost about \$1.2 billion per launch, it is readily apparent that using NTRs for the mission saves many billions of dollars per crew.

Development of an NTR today faces many challenges, both technical and political. Some of the key technology issues include developing a fuel which has very high fission product retention, and designing a core which maximizes the rocket performance while leaving an adequate safety margin. This thesis will explore the facets of NTR core design, and apply new techniques for design and simulation. The focus will be towards the smallest-class of NTRs, with a thrust on the order of 10 klbf-thrust. This size is the most likely to be pursued as a development engine and used for a near-term science mission.

1.1 Objectives

The objectives of this thesis involve a number of tasks to recapture the design philosophy for nuclear thermal rocket cores, modernize the analysis methods for a tungsten cermet fuel element design, and make recommendations for the coolant channel configuration. The objectives, specifically, are:

1. To use modernized thermal hydraulic and neutronics modeling techniques of nuclear thermal rocket reactor cores using Computational Fluid Dynamics (CFD) and Monte Carlo neutronics.
2. To assess the uncertainty of the modern analysis methods.
3. To perform a basic parametric study on the prismatic fuel element configuration, and use the results to make specific recommendations for the coolant channel size and distribution.

4. To demonstrate a stress analysis of one of the recommended fuel element designs.

1.2 Significance of Work

The large majority of research and development on nuclear thermal rockets is four to five decades old. The original groundwork laid out by the Rover/NERVA program (see Section 2.1) and a few others from that time period is indeed a very valuable resource, but is nonetheless not on the same level of sophistication as modern nuclear technology research and development. Although many of the original design studies in the 1960's did achieve an impressive level of accuracy, the analysis and computational tools they used are no longer operational and they used many simplifying assumptions, which justifies re-developing some basic design tools and methods.

Though sporadic, there have been a few significant design efforts over the last two decades which have helped to modernize the design process for nuclear thermal rocket cores. Discussed in more detail in Section 2.5, these studies have helped to shift the NTR fuel element analysis technique from a set of de-coupled 1D and 2D problems into an integrated three-dimensional CFD simulation.

One set of authors in particular, J. Webb, W. Taitano, and B. Gross in Reference [3], have demonstrated the core-wide simulation method, in which a full-detail symmetry section of the core and periphery are simulated in one combined analysis. This study will use much of the same analysis methodology used in that effort. However, in relation to that work, this study will more closely examine the underlying fluid, heat transfer, and

reactor physics problems that make up the simulation, benchmark them where possible, and apply the technique to a specific reference design.

Three broad types of analysis have been run on nuclear thermal rocket cores, which generally require increasing demands of computing power: The first type, which is the oldest, involves breaking down the thermal-fluid system into a series of simpler 1D and 2D problems, and relying heavily on empirical correlations for parameters such as Nusselt number and pressure drop. The second type, which has become prevalent in the last five years, takes a symmetric slice of a single fuel element and runs a 3D CFD simulation which can simultaneously solve for the fuel and coolant conditions. The third type entails running a 3D CFD and neutronics simulation on a symmetric slice of the entire core and radial periphery, explicitly modeling all fluid passages and solid components. The capabilities of these three analysis strategies with respect to common objectives are summarized in Table 1.1.

Table 1.1 Comparison of the abilities of different analysis techniques

Analysis Objective	1. 1D/2D with Empirical Correlations	2. Single-Element CFD	3. Core-Wide CFD
Predict cooling channel temperatures and pressures	Has achieved +/- 5% on wall temperature [4].	Matches SNRE empirical correlations for max fuel temp to within 100 K [5].	Same capability as Limited CFD.
Predict solid stresses	Requires simplifying assumptions on geometry.	Stresses due to coatings/claddings can be calculated.	Same capability as Limited CFD, with additional stresses from adjacent fuel elements and structures.
Predict overall engine performance	Assumes an averaging technique for exit flow based on a single channel. Requires extrapolating correlations beyond their applicability.	Assumes an averaging technique for exit flow based on a single fuel element. Can provide insight into local phenomena.	All flow is modeled explicitly, requiring no assumptions or averaging. Same capability as Limited CFD, with additional detail possible.
Investigate novel cooling configurations	Requires extrapolating correlations beyond their applicability.	Can provide insight into local phenomena.	Same capability as Limited CFD, with additional detail possible.
Model the effect of detailed hardware components	Requires a separate, uncoupled analysis.	Requires a separate, uncoupled analysis.	Components are integrated into the simulation.
Couple neutronics with temperature reactivity feedback	Not possible with single channel analysis.	Not possible with single fuel element analysis.	Possible with Star-CCM+ and MCNP [6]

This thesis will primarily use Type-2 level analysis. The primary advantages gained in going from the Type-2 single-element CFD technique to the Type-3 core-wide CFD technique include the ability to account for stresses and failure modes that occur from fuel element and component interactions within the core; more accurate prediction of core performance; a coupled assessment of radial periphery components such as the pressure vessel and reflector; and the capability to couple a neutronics simulation with

temperature reactivity feedback from the CFD simulation. Essentially, the core-wide technique represents a step towards creating a “virtual reactor”, similar to the goals that are being pursued by the Oak Ridge National Laboratory and a number of partners involved with the Consortium for Advanced Simulation of LWRs (CASL) [7] [8].

The traditional Type-1 methods for analysis of an NTR core are satisfactory in many respects. Indeed, the entire NERVA program was successfully built using 1D empirical correlation-based methods. However, the 18 years of sustained funding for Rover/NERVA development was a paradigm that is not likely to return. Instead, any NTR development program in the near future will need to be lean and progress very quickly in order to avoid being lost in the cyclic shift in space exploration priorities. In addition, a far more conservative attitude towards safety prevails today, and any failures involving nuclear material will promptly fuel critics’ calls for ending the program. Under these conditions, the ability to quickly vet detailed design options will be an extremely valuable tool. The need for experimental trial and error, and therefore the risk of accidents, can be reduced.

Before the new set of analysis methods can truly be “trusted,” however, an effort must be made to quantify what level of accuracy they are capable of. This is especially critical considering the reduced safety margin that NTRs operate at, as compared to traditional power reactors. In a typical terrestrial, UO_2 fuel-pin light water reactor, the peak fuel temperature is typically 1800 K, while the fuel melting temperature is at 3120 K – a 40 % safety margin [9]. In an NTR – which also uses UO_2 , however, many researchers have proposed designs with peak fuel temperatures of 3000 K. This

represents a margin of only 4%. Although that kind of temperature is necessary in order to achieve high performance, there needs to be a high level of scrutiny applied to the analysis methods which predict such temperatures. One of the primary focuses of this research will be to assess the uncertainty that modern analysis tools can achieve when applied to an NTR fuel element.

2. NUCLEAR THERMAL ROCKET OVERVIEW

This section will give an overview of the original development of nuclear thermal rockets and the general features of an NTR design. In Section 2.3 the motivation for using a cermet fuel, as opposed to graphite fuel, will be discussed. Section 2.5 will review some of the conventional methods used for evaluating NTR fuel element performance.

2.1 History

The nuclear thermal rocket in its most familiar form was first proposed at the Oak Ridge National Laboratory by the young physicist Robert Bussard in 1953 [10]. By 1955, after further study and some political maneuvering, the Atomic Energy Commission (AEC) initiated Project Rover at the Los Alamos Scientific Laboratory (LASL). The Rover team was tasked with developing a graphite-fuel based nuclear thermal rocket engine, starting essentially from scratch. Over the course of just a few years, the Rover team quickly built and successfully operated eight NTR reactors by 1964 through the Kiwi program [10]. In the subsequent Phoebus program, three high-power reactors were tested (including the highest-power reactor *ever* built to date), and the engine and fuel configurations were refined. All testing occurred at the Jackass Flats test site in Nevada, where exhaust was captured and filtered before being released into the atmosphere. Concurrent with Project Rover was the NERVA (Nuclear Engine for Rocket Vehicle Application) program, which worked to configure the reactor designs demonstrated in Kiwi and Pheobus into an integrated rocket engine that could be used

for manned mission to Mars. The NERVA engines that were developed and tested used many flight-ready components, and by the end of the program met all requirements for the Mars mission, which was tentatively planned to follow in the years after Apollo.

Unfortunately, the Nixon administration cancelled the NERVA program in 1972, and NTRs have not seen a development program anywhere close to that scale since. But the 18-year program successfully proved that NTRs work, and leaves behind a tremendous legacy and collection of data for future generations of designers. A handful of NTR design programs have been initiated at NASA in the decades since, though the limited funding has not allowed for much significant hardware to be built. Today, NASA is engaged in a fairly large design study with an accompanying fuels research program under the Advanced Exploration Systems (AES) initiative, based mostly at the Marshall Space Flight Center and Glenn Research Center. The funding for this program in subsequent years is considered tenuous, though the general level of interest among NASA leaders in NTRs has been increasing in recent years.

2.2 Conceptual Design

The principal advantage of a solid-core nuclear thermal rocket is its ability to use hydrogen as a single propellant, instead of the byproducts of combustion that are used in chemical propulsion. The sole purpose of the nuclear reactor in an NTR, then, is to act as a heat exchanger to raise the temperature of the hydrogen as high as safely possible. Figure 2.1 is a simplified drawing of a nuclear thermal rocket that shows many of the parts that are common to most NTR designs.

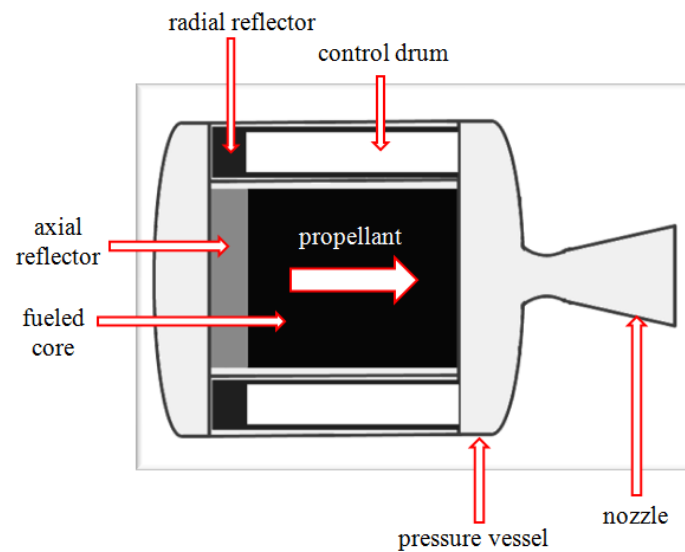


Fig. 2.1 Conceptual drawing of a typical solid-core Nuclear Thermal Rocket

The core is the active fuel region which acts as the heat source. Although there have been several types of configurations proposed, including liquid or gaseous fuel, the solid prismatic core with hexagonal fuel elements has proven to be a simple and reliable form. Each fuel element contains a number of coolant channels in a triangular lattice. An example of a typical fuel element cross section is shown in Fig. 2.2.

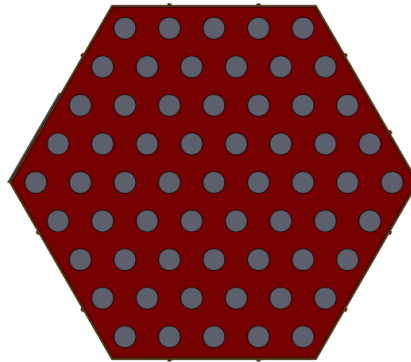


Fig. 2.2 Typical fuel element cross section with 61 coolant channels

For the small, high-power cores that are typical for space reactors, neutron leakage has a large overall effect on the multiplication factor of the reactor, or reactivity worth. It is customary to provide a relatively thick radial neutron reflector and a forward axial reflector, which serve to scatter neutrons back into the fissile core. Beryllium and beryllium oxide are common material choices for the reflectors.

One of the most convenient methods of control for the small space reactors is to absorb or allow the leakage of the neutrons entering the radial reflector. A common design is to have a boron absorber on part of the drum, which can be rotated to insert or remove reactivity.

The core and reflector regions are contained within a pressure and load-carrying vessel, which is commonly made out of a nickel-alloy or other high-temperature metal. The pressure vessel is integrated with the nozzle, and both contain a series of parallel brazed tubes which carry coolant to keep them from overheating.

Nearly all NTR designs are pressurized by a turbopump assembly, which can be powered by different cycle configurations. Common engine cycles include a bleed cycle in which hot propellant is tapped from the exit of the core and ducted to the turbine; or an expander cycle, in which the enthalpy gained from cooling the nozzle and other structural components is large enough to power the turbopump.

2.3 Motivation for the Cermet Fuel

Because of the extensive knowledge gained from the Rover/NERVA program, the “default” fuel type for an NTR is uranium carbide embedded in graphite. However, one important issue of the graphite NTR fuels that was never completely resolved is the escape of fission products from the core. The graphite fuel elements experienced a significant coefficient of thermal expansion (CTE) mismatch with their cladding [10]. Although this problem was significantly reduced over the course of the development program, the fission product emission was still at a level that would probably be unacceptable for today’s environmental standards.

An alternative to the graphite fuel that was pursued consists of uranium dioxide immersed in a tungsten matrix, creating a W-UO₂ cermet (ceramic-metal) fuel. The W-UO₂ fuel competes with and has advantages over the graphite fuel in many areas: It has comparable high temperature strength and thermal conductivity, superior chemical compatibility with hydrogen, superior response to thermal transients, and a much better matched CTE with common cladding materials [11]. Though the tungsten-cermet fuel is substantially heavier than the graphite fuel, the cermet reactors usually operate on a fast

neutron spectrum, eliminating the need for and volume associated with a neutron moderating material. As a result, fast cermet cores can be more compact and operate at a higher power density, which helps to make the engine thrust-to-weight ratio competitive with that of graphite cores.

2.4 Previous Cermet-NTR Development Programs

Although not on the level of Rover/NERVA, cermet fuels did receive a significant amount of funding and development in the 1960's. Two programs in particular, the General Electric 710 program, and the Argonne National Laboratory (ANL) Nuclear Rocket Program, rapidly advanced the technology readiness level of the cermet fuels in just a few years. Both programs independently developed the ability to manufacture full-length tungsten cermet hexagonal fuel elements and experimented with the based stabilizers and claddings. Stabilizers are necessary to minimize the ability of free uranium to form in the fuel matrix, and effectively raise the melting temperature of the fuel. The cermet element samples were run through a thorough range of testing, including thermal cycling, hot hydrogen exposure, and irradiation [12] [13]. Each program also conducted thorough design studies for tungsten-cermet based fast-spectrum NTRs. By the end of both programs, the suitability of tungsten-cermet fuel for use in an NTR was well demonstrated.

2.5 Historical Methods of Analysis

The traditional approach to modeling the core of an NTR breaks the problem down according to certain assumptions and boundary conditions, which in general include the following steps:

1. Neutronics. Power density distributions are calculated using industry-standard neutronics codes. Monte-Carlo methods are commonly used for all reactor types, while multi-group diffusion codes are sometimes used, and are well suited for fast reactors [14]. Most studies from the last ten years have used some version of the Monte Carlo N-Transport (MCNP) code developed at Los Alamos [15]. The use of MCNP allows for detailed heterogeneous effects to be modeled, and B. Schnitzler has demonstrated some of the more recent application of Monte Carlo techniques to NTR cores [16]. J. Webb et al. has also shown the capabilities to use the 3D tallies from MCNP to evaluate the energy deposition in an NTR core [3]. In some cases, a detailed neutronics calculation is substituted for a simpler approximation of the power shape [17]. This usually has the advantage of a quicker analysis time while ignoring some of the detailed heterogeneity of the reactor.
2. Fluid Heat Transfer. A peak and/or average channel analysis is performed. The fuel element with the highest power density is typically used as the basis for design, since it is expected to reach the highest temperatures. A case is also usually run for a channel exhibiting the average conditions in the core, which can

be used in estimating overall performance. A one-dimensional conjugate heat transfer problem is first solved for the cooling channels in the isolated element. Nusselt number correlations are used to predict the wall temperature of the fuel along with the bulk fluid temperature. Empirical friction factor equations are used to solve for the pressure drop. This approach was the original technique used by the Rover/NERVA program [18] and has been consistently used up until today [19]. Because of its quick solving time, this method is still the primary option used for systems and engine balance codes [20].

A study using the ELM program, a Fortran code developed to design fuel elements at the Lewis Research Center in 1992, compared these 1D empirical techniques to experimental data from the NRX-A test series, in which thermocouples were embedded into a cooling channel wall in five axial locations [4]. After attempting various applicable empirical correlations, the program came reasonably close to the experimental data, with a consistent under-prediction of the maximum wall temperature by about 200 K.

One other strategy for solving for the flow in the core is to use the porous media assumption, in which the thousands of cooling channels are lumped together by a single set of governing equations. This greatly reduces the computational power required to analyze the whole engine, allowing the flow through the core to be coupled with a compressible flow CFD simulation of the nozzle, as was done by T.S. Wang et al. [17]. However, the porous media

approach is inappropriate for assessing the detailed design of fuel elements since it does not resolve the geometric details of the cooling channels.

3. Fuel Heat Conduction. A symmetry-section of the hottest fuel element is isolated for in-depth analysis. Typically the section to be analyzed is a $1/12^{\text{th}}$ or $1/6^{\text{th}}$ cross section of the hexagonal fuel element at the axial location where the peak wall temperatures are found. It is common to run a 2D heat conduction case in order to determine the peak fuel temperature. Figure 2.3 shows examples of the mesh discretization used in two such studies [21] [22].



Fig. 2.3 (a) Mesh from 1966 NASA study [21] (b) Mesh from 2007 study [22]

A simpler version of the peak-temperature analysis assumes the problem can be represented by an axisymmetric geometry with equivalent proportions of coolant and fuel that are found in the fuel element. Using this approximation, Fourier's law of heat conduction may be solved for in one dimension thereby allowing for

a very quick analysis. This fundamental approach was used extensively during the development programs of the 1960's [23], but can still be useful today for conducting parametric studies of fuel element geometry.

4. Stress Analysis. A separate analysis may use the calculated temperatures to approximate the stresses in the fuel element. The driving stresses are generally the result of thermal expansion mismatches between the fuel and cladding, but could result from temperature and pressure gradients. During the Rover/NERVA development programs and for much of the design work since, the approach has been to simplify the fuel element geometry into an equivalent cylindrical form, on which it is easier to apply analytical stress relationships [23] [24]. These analyses are typically done in conjunction with experimental test programs.

Within the last five years, steps 2 through 4 of the traditional methods have been combined into one step, using a 3D CFD simulation of a 1/12th section of a single fuel element [25] [5] [22]. This method accounts for axial conduction in the fuel element, unlike many of the empirical methods, and can readily be used to analyze the complex flows in structural elements such as tie tubes. The three-dimensional finite volume or finite element discretization of the fuel element allows many different sets of physics (e.g. thermal diffusion and stress and strain) to be solved simultaneously. A study comparing this method to experimental data has yet to be published, but the versatility and power of coupling fluid flow, solid conduction, and stress into one simulation has been demonstrated. Stewart and Schnitzler compared the 3D CFD results with those

from the 1D empirical methods, and found they match to within 3% for predicting peak fuel temperature [5].

One of the ultimate goals in reactor simulation is to be able to couple 3D reactor physics codes with 3D CFD software. This technique has been explored in recent years. Seker et al. demonstrated a software tool for coupling MCNP5 and Star-CD for an array of Pressurized Water Reactor (PWR) fuel pins [6]; and more recently Cardoni et al. developed an independent code to couple MCNP5 with Star-CCM+, also for a PWR pin cell [26]. Although these studies successfully demonstrated the coupling capability between MCNP and Star-CCM+, the level of detail achieved is not yet on a level that is useful for comprehensive fuel element and core design. But as computational resources continue to grow in the coming years, it is likely that these methods will eventually be deployed for full-core analysis.

3. ANALYSIS METHODS

This section will explain the analysis methods and operating principles of the codes used for NTR simulation. First, the important parameters to solve for are discussed in Section 3.1. Then the governing equations for the CFD simulations are explained, followed by a discussion on thermophysical material properties. The principles of the neutronics simulations are then discussed along with the method used to obtain energy deposition information. Finally, the specific applications of these methods in this thesis are discussed in Section 3.9.

3.1 Parameters of Interest

The analysis objectives are determined by identifying all significant performance requirements and possible failure modes. The following is a discussion of each fundamental parameter, its associated requirement and/or failure mode, and the strategy for its analysis.

1. Fuel temperature. There is no minimum for the fuel temperature, but it has a clear maximum allowable temperature depending on the melting point of the fuel, which is approximately 3120 K for UO_2 . In addition, at long duration at high temperatures, more subtle failure modes such as chemical diffusion of the uranium out of the fuel matrix may occur. As discussed in the introduction, NTRs operate with a much smaller margin to the melting temperature than conventional nuclear reactors, which makes accurate prediction of fuel temperature essential. The temperature of the fuel

is a direct output of the CFD simulations in Star-CCM+ version 7.02.011, which solves a steady state heat conduction problem for the finite volume mesh [27].

Potential errors may arise from unsatisfactory spatial resolution or solution convergence. The former is addressed by conducting convergence tests on the problem mesh; the latter is addressed by ensuring enough iterations are run and examining the residuals of the governing equations and other simulation parameters for convergence. Within the CFD package used in this thesis, there is no capability to model the solid-state diffusion of uranium in the fuel; therefore that failure mode will be neglected.

2. Propellant Temperature. The core exit propellant temperature is the key driving parameter for rocket performance. It has a target clearly defined by specific impulse requirements. The details of selecting this target temperature are discussed in Section 5.3.4., but it typically lays in excess of 2600 K. The flow in each coolant channel is solved in Star-CCM+ by assuming a steady state problem with turbulent flow. Hydrogen properties are inputted with custom functions to account for high-temperature effects including dissociation. Star-CCM+ has numerous Reynolds Averaged Navier Stokes (RANS) turbulence models, and the specific model used is determined from benchmarking. The solution algorithm implemented by Star-CCM+ uses a segregated flow and energy solver, which is appropriate for mildly compressive flows [27]. The solution will result in full report of the velocity, pressure, and temperature distribution in each channel.

3. Core Pressure Drop. More-so than any other parameters, the requirement for pressure drop is tightly coupled with the overall engine cycle analysis. It has a direct effect on the required inlet pressure to the core, and the corresponding demand on the turbopump. Therefore, no specific minimum or maximum can be declared, but historical values typically range anywhere from a few tens of psi to 400 psi. The pressure distribution is a direct output from Star-CCM+. The pressure drop is defined as the difference between the coolant channel inlet and outlet pressure. Because all of the channels in the core are part of the same parallel flow system, the pressure drop will be the same in all channels.
4. Fuel Element Stress. Stress is one of the primary methods for checking structural failure modes. There are no minimums for the solid stress, of course, but there are many factors to account for in defining a maximum. Discussed further in Section 6, stress in the fuel element or cladding can be induced from high temperature gradients, coefficient of thermal expansion mismatches, and pressure differentials. The maximum allowable stress must be determined from experimentation. Star-CCM+ has a built-in solver for solid stress using finite volume cells [27]. By applying the proper material properties and boundary conditions, each of the major macroscopic causes of stress can be approximated. Star-CCM+ reports the each of the principal stresses and strains in each cell. After a solution has converged, the locations of maximum stresses can be investigated and compared with allowable levels for those materials.

The method of analysis to be used in this thesis combines neutronics with CFD and solid stress calculations, which can be termed a “combined physics” or “multiphysics-uncoupled” approach. However, as discussed in Section 2.5, there is a potential for the tools used to evolve into a multiphysics-coupled method.

3.2 Important Thermal-Fluid Phenomena

Before the governing equations specific to Star-CCM+ are discussed, the fundamental flow phenomena which are relevant to NTR core analysis are discussed in a one-dimensional context. Although the actual conservation equations which are solved are more complex, an accompanying discussion of the 1-D relationships can be instructive and allow a more intuitive interpretation into the important physics concepts taking place.

Beginning with the equations for conservation of mass, momentum, and energy, there is a wide range of assumptions and methods that may be used for solving convective heat transfer problems. The flow of high-temperature, high-speed hydrogen through the small circular channels of an NTR core may be classified as compressible flow with heat transfer and friction. The assumption of compressibility (or rather, the relaxing of the assumption of incompressibility) can be necessitated by any combination of dynamical effects such as fluid acceleration, viscous dissipation, or rotation; or temperature changes due to external heat addition or internal heat generation. Within the scope of NTR channel analysis, compressibility effects due to fluid accelerations are actually relatively minor, however. Depending on the core design, the Mach number in an NTR coolant

channel may approach $M = 0.3$, at which point the stagnation pressures from incompressible and compressible theory differ by about 2% [28]. But despite the moderate Mach numbers, compressibility from viscous (friction) effects in the channel and the external heat addition will be significant. Equation 3.1 expresses the order of magnitude of density changes that can be expected due to the combination of a temperature change and flow inertial changes.

$$\frac{\Delta\rho}{\rho} \sim \frac{\Delta T_{imposed}}{T_{ref}} + O(M^2) \quad (3.1)$$

where $\Delta T_{imposed}$ can be considered the change in temperature between the inlet and outlet of the channel, and T_{ref} may be the inlet temperature [28]. For a typical NTR channel, the temperature ratio in Eq. 3.1 easily exceeds a factor of ten, which requires that the flow be treated with compressible theory.

The flow and energy distribution of any fluid problem can be obtained by solving the conservation equations of mass, momentum, and energy, subject to the assumptions for a given application. The most general forms of these equations are introduced here, in the context of the property changes occurring within finite volume element. Eq. 3.2 is the conservation of mass [29]:

$$\frac{\partial\rho}{\partial t} = -(\Delta \cdot \rho\mathbf{v}) \quad (3.2)$$

where ρ is the fluid density, and \mathbf{v} is the velocity vector. The left hand side (LHS) represents the time rate of change of mass in the volume, and right hand side (RHS)

represents the net rate of mass addition into the volume by fluid convection. The conservation of momentum can be generally expressed as [29]:

$$\frac{\partial}{\partial t} \rho \mathbf{v} = -[\nabla \cdot \rho \mathbf{v} \mathbf{v}] - \nabla p - [\nabla \cdot \boldsymbol{\tau}] + \rho \mathbf{g} \quad (3.3)$$

where p is the pressure, $\boldsymbol{\tau}$ is a stress tensor, and \mathbf{g} is the acceleration due to gravity. The LHS represents the rate of momentum addition to a volume element; the first term on the RHS represents the rate of momentum addition by convection; the second term represents the momentum addition to a pressure gradient; the third term represents the momentum addition due to a shear stress gradient; and the fourth term represents the momentum addition due to gravity, which could be generalized to include any body force [29]. The final governing equation, the conservation of energy, is shown in Eq. 3.4 [29]:

$$\begin{aligned} \frac{\partial}{\partial t} \left(\frac{1}{2} \rho v^2 + \rho \hat{U} \right) = & - \left(\nabla \cdot \left(\frac{1}{2} \rho v^2 + \rho \hat{U} \right) \mathbf{v} \right) - (\nabla \cdot \mathbf{q}) - (\nabla \cdot p \mathbf{v}) \\ & - (\nabla \cdot [\boldsymbol{\tau} \cdot \mathbf{v}]) + \rho (\mathbf{v} \cdot \mathbf{g}) \end{aligned} \quad (3.4)$$

where \hat{U} is the fluid specific internal energy and \mathbf{q} is heat flux. The LHS represents the rate of energy increase in a volume element; the first term on the RHS represents the energy addition by convection; the second term represents the energy addition by conduction; the third term represents the work done on the fluid by pressure; the fourth term represents the work done by viscous forces; and the final term accounts for work done by external forces [29].

There are many additional approximations and relationships that are required before Eqs. 3.2 through 3.4 are solvable. Those assumptions which are most relevant to Star-CCM+ are discussed in the following section.

3.3 Operating Principles of Star-CCM+

The set of conservation equations for a fluid are often referred to as the Navier-Stokes equations, although there is some variety in the exact notation used to express them. Star-CCM+'s conventions will be used here, and Eq.3.5 represents the equation of momentum as written in the manual [27]. This equation is conserving the same properties as Eq. 3.3, but is expressed in integral form.

$$\begin{aligned} \frac{d}{dt} \int_V \rho \chi dV + \oint_A \rho \mathbf{v} (\mathbf{v} - \mathbf{v}_g) \cdot d\mathbf{a} \\ = - \oint_A p \mathbf{I} \cdot d\mathbf{a} + \oint_A \mathbf{T} \cdot d\mathbf{a} + \int_V (f_r + f_g + f_p + f_u + f_\omega) dV \end{aligned} \quad (3.5)$$

where \mathbf{a} is the area vector for a cell face, \mathbf{I} is the identity matrix, \mathbf{T} is the viscous stress tensor, and f 's are body forces due to rotation, gravity, porous media, user-defined, and vorticity confinement, respectively. All of these except f_u are insignificant for the intended application. χ is a porosity multiplier which is not relevant to the problems of interest in this thesis either, so it will be dropped in subsequent equations.

When the conservation of momentum in Eq. 3.5 is applied to a finite volume grid, the result is Eq. 3.6:

$$\frac{d}{dt}(\rho \mathbf{v} V)_0 + \sum_f [\mathbf{v} \rho (\mathbf{v} - \mathbf{v}_g) \cdot \mathbf{a}]_f = - \sum_f (p \mathbf{I} \cdot \mathbf{a})_f + \sum_f \mathbf{T} \cdot \mathbf{a} \quad (3.6)$$

where the subscript 0 denotes the conservation balance for cell 0 , and the summation domain of f includes all faces of that cell. The continuity and energy equations are discretized in a similar fashion, although they are not repeated here.

The most challenging term in Eq. 3.6 to resolve is the viscous flux, due to its chaotic nature in a turbulent flow. It is common to invoke the Boussinesq approximation to express the viscous stress tensor [27]:

$$\mathbf{T} = \mu_{eff} \left[\nabla \mathbf{v} + \nabla \mathbf{v}^T - \frac{2}{3} (\nabla \cdot \mathbf{v}) \mathbf{I} \right] \quad (3.7)$$

where μ_{eff} is the effective viscosity as the sum of the laminar viscosity, μ , and the turbulent viscosity, μ_t .

For Star-CCM+'s segregated solver, the SIMPLE (Semi-Implicit Method for Pressure-Linked Equations) solution method is used. This involves a 12-step procedure to update the fluxes and properties in each cell during each iteration. One of the key features of the SIMPLE method is that the velocity field is first estimated from initial conditions or a previous iteration, which is then used to calculate the pressure field; which is in turn used to correct and update the velocity field and fluxes. The fact that the pressure and velocity fields are not solved simultaneously has consequences on the applicability of the method to compressible flows. Since in a truly compressible flow the velocity and pressure fields will be coupled, their separation in the SIMPLE algorithm introduces the possibility of inaccuracy for flows at high Mach numbers. As a guideline, the Star-

CCM+ manual recommends that the SIMPLE solver only be applied to mildly compressive flows, and that the under-relaxation factors be reduced to slow the decoupling of pressure and velocity. The flow inside a typical NTR channel safely falls within an acceptable regime for the SIMPLE solver.

In Section 4.2.3 a variety of turbulence models are explored, but for the majority of simulations in this thesis the k-epsilon two-layer realizable model is used. This model adds two coupled equations to the conservation equations (and equation of state) to make the overall system solvable. The first equation solves for the turbulent kinetic energy, k , and the second equation solves for the turbulent kinetic energy dissipation rate, ϵ . The realizable model includes additional terms to ensure that the model always physically-possible results. The two-layer approach computes the turbulent kinetic energy in two distinct regions: the viscous sub-layer near the wall, and the main turbulent region far from the wall. The buffer layer between the two is calculated as a smoothed function.

3.4 Material Properties

3.4.1 Hydrogen Properties

Hydrogen is conveniently an excellent coolant, having one of the highest specific heat capacities of any gas. However, hydrogen's thermodynamic properties vary greatly with temperature. They have particularly complicated behavior at cold temperatures (below about 300 K) due to the existence of spin isomers, and also at high temperatures (above about 1500 K) due to molecular dissociation. Although many compilations of hydrogen properties have been published, there is no definitive source for this data.

Molecular hydrogen (H_2) exists in two spin isomer states: ortho-hydrogen in which the two protons spin parallel to each other; and para-hydrogen in which they spin antiparallel to each other. Due to the effects that this spin behavior has on the rotational energy of the molecule, orthohydrogen and parahydrogen have significantly different thermodynamic properties for temperatures below 300 K, particularly for specific heat and thermal conductivity. Density and viscosity values, on the other hand, are effectively the same for each isomer [30].

In its liquid state (below 20.3 K at one atmosphere), the equilibrium concentration is very close to 100% parahydrogen. Orthohydrogen is unstable at these temperatures, and slowly and exothermically decays to parahydrogen, an effect which must be controlled for in cryogenic storage [31]. As the hydrogen is heated, the equilibrium composition shifts to 25% para/ 75% ortho, where it remains for temperatures above 300 K [30]. This composition of hydrogen (3:1 ortho-to-para) is sometimes referred to as “normal” hydrogen. Pressure does not have a measurable effect on this composition.

At ambient temperature, the transition rate between para and orthohydrogen is relatively slow (on the order of days) unless a catalyst mechanism is present [32]. In the case of a nuclear thermal rocket engine, the liquid hydrogen is stored as 100% parahydrogen and is expected to remain in this state as it passes through the pump and the initial components in its regenerative circuit. However, the high core temperatures and presence of paramagnetic catalysts (such as stainless steel) cause a full conversion to normal hydrogen at some point in the engine which is not precisely known. Gamma and neutron radiation fields are also suspected to facilitate the conversion process.

Experiments run at LANL to investigate this effect have shown that radiation plays a minimal conversion role at low temperatures, but becomes significant for temperatures over 196 K [32].

This spin-state conversion is significant for the analysis of components for which the hydrogen flows through at cold temperatures, such as the radial reflector and pressure vessel tubing. For example, at 150 K, the thermal conductivity of parahydrogen is about 20% larger than that for normal hydrogen [30]. However, the differences in thermophysical properties between para and normal hydrogen become negligible above about 300 K (which is close to a typical core inlet temperature). Because the focus of this study is to evaluate the performance of the reactor core, and the peripheral engine components are only a secondary concern, the properties of parahydrogen will be assumed throughout all calculations. This selection is based on the much wider availability of parahydrogen data over normal hydrogen. It is noted that this choice will have no significant effect on the high-temperature core analysis, but may introduce some appreciable error into the reflector simulation.

As previously mentioned, there is a large variety of sources from which to obtain the thermophysical properties of hydrogen. A major study conducted by NASA in 1975 surveyed hundreds of reports and organized the data for each property [33]. The survey tabulates the “best data” for parahydrogen from its melting point up to 3000 K for pressures ranging from 0.01 MPa to 100 MPa, and includes estimates for the uncertainty of each parameter.

Property curves for this research were generated by transferring the tabulated data in Reference [33] into Microsoft Excel and then using Excel to calculate 4th or 5th order polynomial curve-fits. The data was also compared with the properties used in Reference [34] and Star-CCM+'s default hydrogen data as a sanity check. There was reasonable agreement between the data from McCarty [33] and Taylor [34], although Taylor's data exhibits a more severe increase in specific heat and thermal conductivity at high temperature. Figure 3.1 shows the Prandtl number calculated from both sets of data.

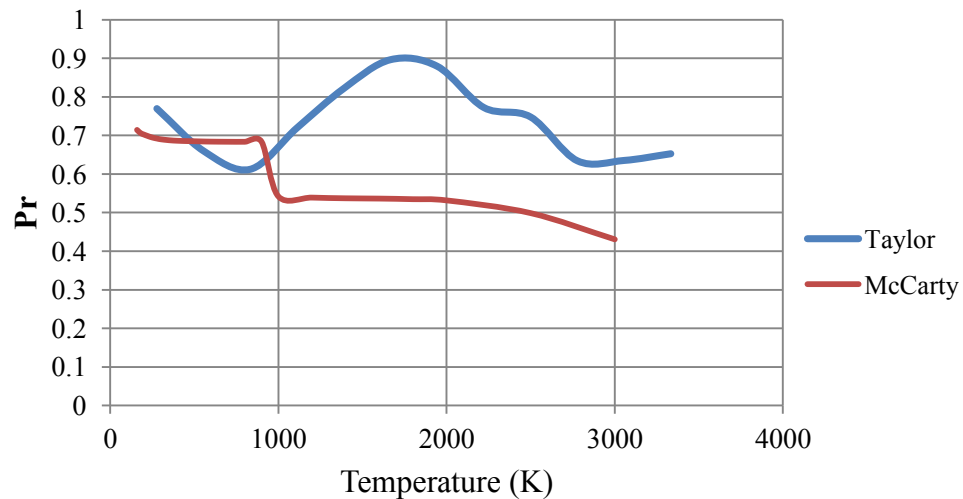


Fig. 3.1 Comparison of hydrogen Prandtl number from two different sources

Despite the discrepancies in different sources of hydrogen data, the set compiled by McCarty [33] is used since it is the most traceable. The Excel-generated polynomial is

directly inputted into Star-CCM+ as a field function. The details and uncertainties associated with each pertinent property are discussed as follows.

For the heat capacity at constant pressure, c_p , McCarty estimates the uncertainty to be very small ($\sim 0.02\%$) at low and moderate densities, but becoming significant at higher pressures and densities (3% at 5000 psia) [33]. To be conservative, the upper limit of 3% is assumed for the uncertainty. The uncertainties for the specific heat capacity at constant volume c_v and specific heat ratio γ are considered to be on a similar scale.

Figure 3.2 shows a plot of c_p for pressures of 3.5 and 7.0 MPa.

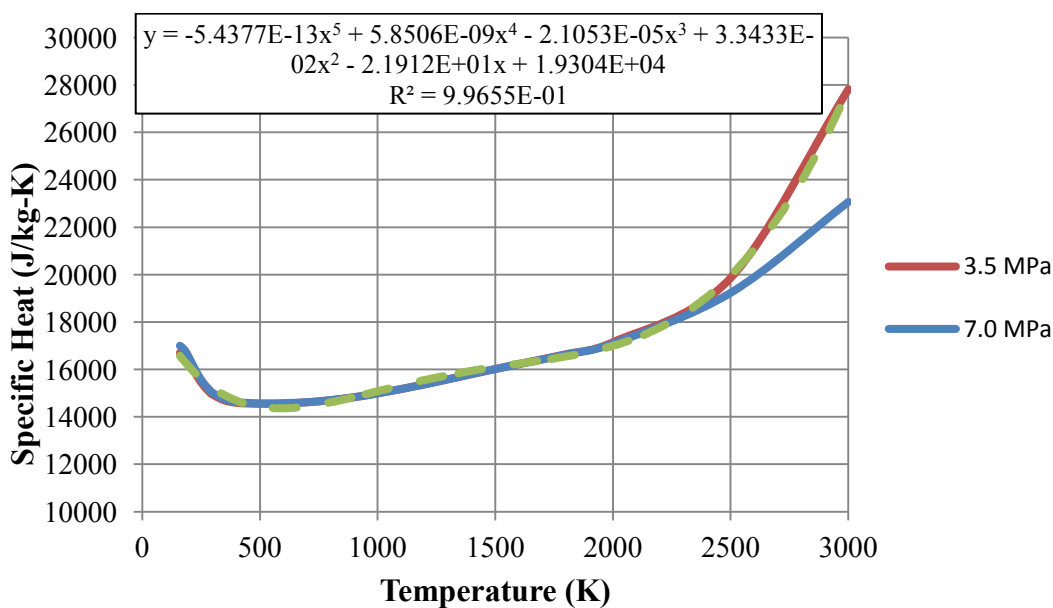


Fig. 3.2 Specific heat at constant pressure (c_p) for hydrogen

The pressure dependence of c_p begins to play a significant role above 2500 K. For the hot end of the core in the ANL-10K, the hydrogen pressure approaches 500 psi in this region. Therefore, the curve-fit polynomial used in simulations was based upon the 500 psi curve.

Figure 3.3 shows the hydrogen thermal conductivity temperature curve which is used. For hydrogen temperatures above 400 K, the uncertainty in thermal conductivity is estimated to be 10%; although it is estimated at only 3% for lower temperatures and moderate pressures [33].

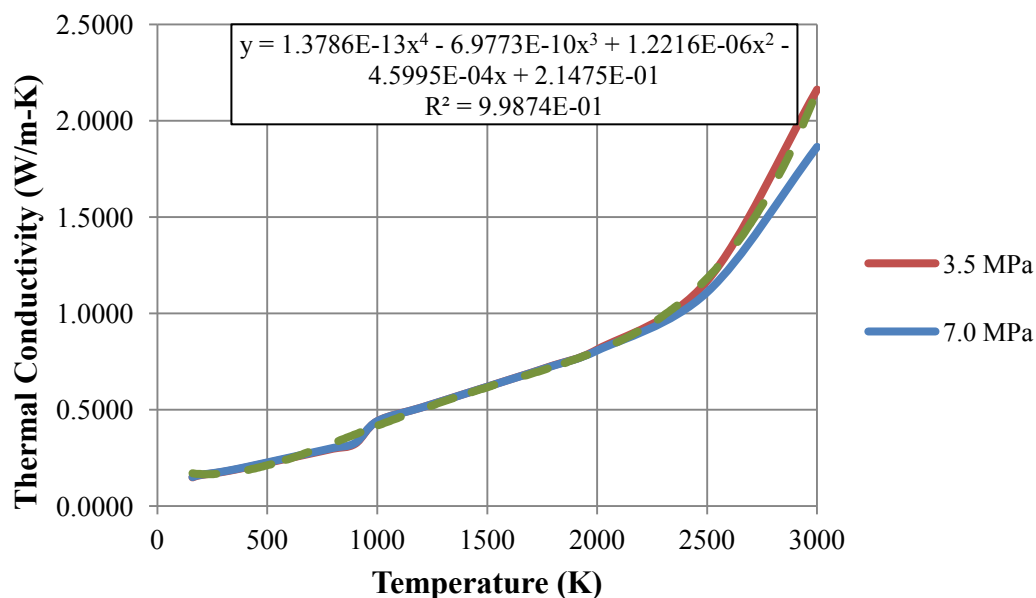


Fig. 3.3 Thermal conductivity of hydrogen

Figure 3.4 shows the hydrogen viscosity temperature curve which is used. For temperatures above 100 K and below 100 atm, which generally encompasses the range of conditions expected in an NTR core, the uncertainty in dynamic viscosity has been estimated at 5% [33].

In addition to approaching the melting point of the fuel, situations in which the hydrogen temperature increases above 3000 K are undesirable from an analysis point of view, since the uncertainty in thermophysical properties increases substantially at those elevated temperatures.

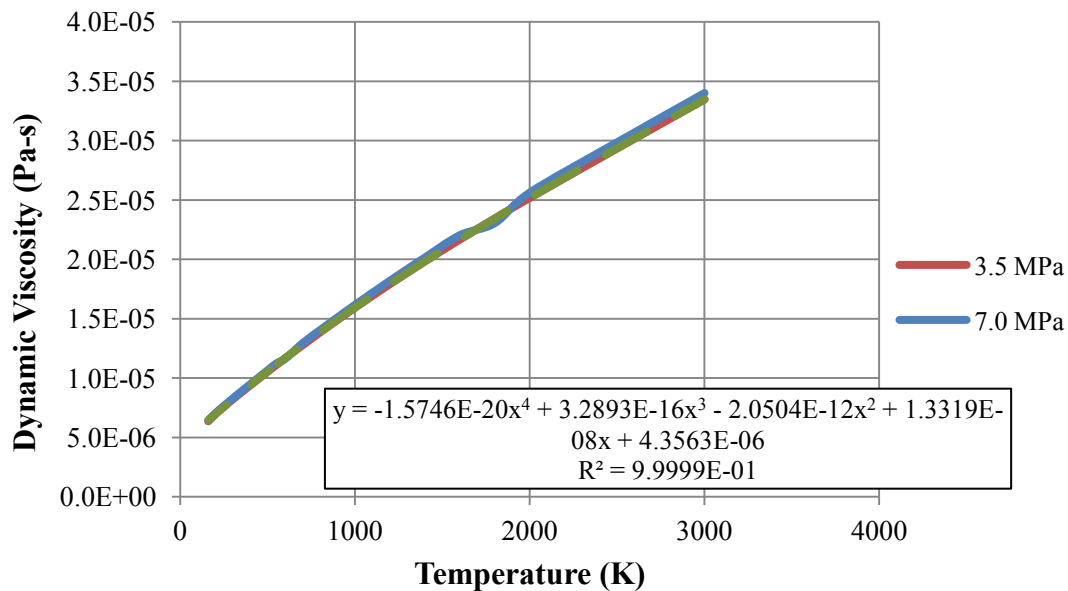


Fig. 3.4 Dynamic viscosity of hydrogen

At high temperatures hydrogen begins to dissociate, causing a significant change in its fluid properties. The presence of monatomic hydrogen offers two beneficial, yet competing, effects on the rocket performance:

1. Monatomic hydrogen has a lower molecular weight, and therefore achieves a higher exhaust velocity.
2. Dissociation of the diatomic hydrogen allows more energy to be absorbed into the propellant without an associated increase in temperature.

The relative importance of each effect depends on the degree of recombination that occurs in the nozzle. Ideally, the full-recombination case (also known as equilibrium flow) would provide the greatest boost in specific impulse. This concept received some attention during SEI in the early 1990's, with some proposing a low-pressure NTR so that dissociation could be maximized. However, CFD studies of that concept have shown that the residence time of the hydrogen in the nozzle is too short for recombination to be significant. Equilibrium nozzle flow is therefore an over-optimistic assumption [35].

3.4.2 Fuel Properties

Tungsten has the highest melting point of all refractory metals and uranium dioxide has the highest melting point of all uranium compounds, so their combination in a dispersion fuel is a logical choice [13]. Both materials have a relatively low vapor pressure and exhibit excellent chemical compatibility with each other. For confinement of the fuel and protection from the high temperature hydrogen, NTR fuels are typically

bonded directly to a cladding metal. While tungsten does have a significant capture cross section at thermal and resonant energies, the cross section is reduced enough by 0.1 MeV to allow for an efficient fast reactor.

Despite the production and testing of many W-UO₂ fuel elements during the GE-710 and ANL programs, their material properties have not been found in the available documentation. There have been two recent efforts at INL however to estimate the thermal conductivity and specific heat of the fuel. The first effort by Webb and Indrajit used the Bruggeman model to predict the conductivity and specific heat at two different concentrations of a gadolinium oxide stabilizer [36]. The second approach by Hawkes uses a finite element analysis in Abaqus of a randomly-mixed model of the component materials [37]. The resulting regressions from both approaches are plotted in Fig. 3.5.

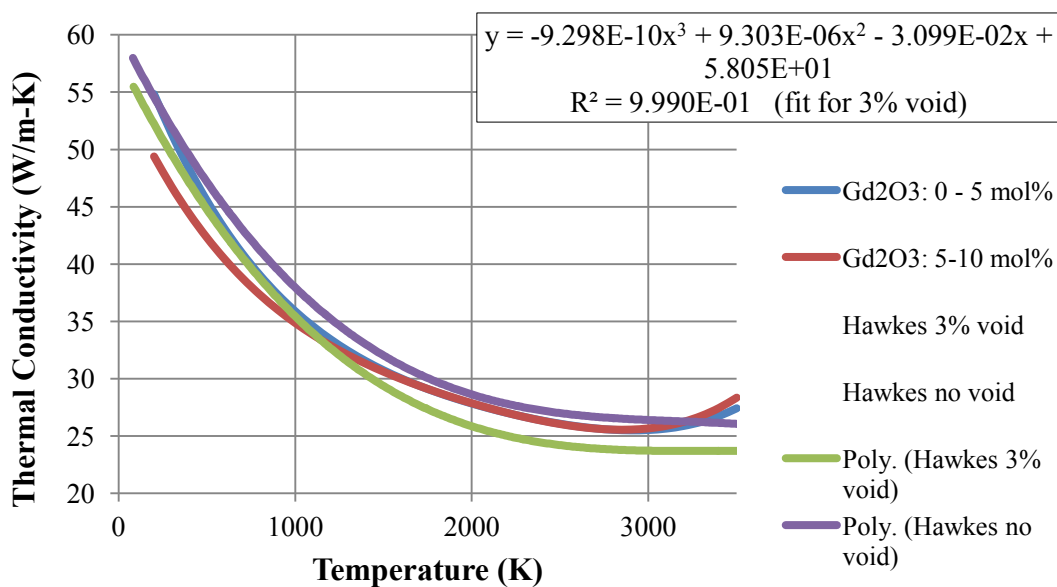


Fig. 3.5 Thermal conductivity of W-60v/oUO₂ cermet fuel

There is reasonable agreement between all models, with a spread of approximately 10% between them. As a conservative measure the lowest conductivity curve is assumed, which comes from Hawkes assuming a 3% void. Although Webb did produce an estimated specific heat curve as well, it is not necessary for the steady-state analysis pursued in this thesis.

For comparison, the estimated thermal conductivity of W-UO₂ (Hawkes 3% void) is plotted with the thermal conductivity of NERVA fuel (uranium carbide coated with pyrolytic graphite in a graphite matrix) in Fig. 3.6 [38].

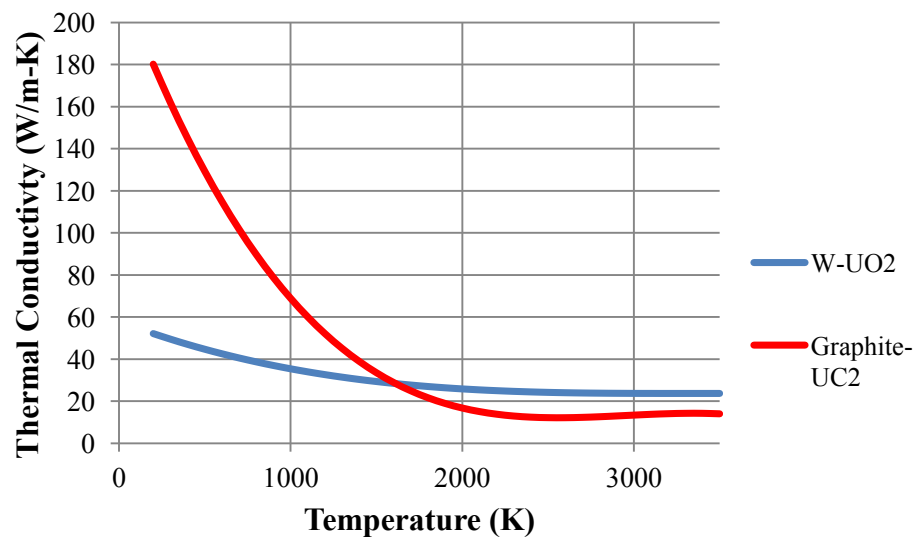


Fig. 3.6 Thermal conductivity of W-UO₂ fuel compared with NERVA fuel

Despite the uncertainties, especially at high temperature and due to the polynomial extrapolation, it appears that the cermet fuel does have a modest advantage over the NERVA fuel at high temperatures.

3.5 Important Neutronics Phenomena

It will be shown in Section 4.4 that the volumetric energy generation comprises about half of the input uncertainty that goes into a fuel temperature calculation. Therefore, an accurate prediction of core neutronics is essential.

In an analogous way to how the fluid conservation equations are developed by considering all the different processes that contribute to the total mass or momentum in a control volume – the neutron transport equation is an accounting of all the different processes that contribute to the total population of neutrons within a control volume. Except, instead of the three-dimensional control volume dealt with in the Navier-Stokes equations, the neutron transport equation solves for neutron distributions in a seven-dimensional phase space, consisting of three position components, two direction components, an energy component, and a time component. Of course, the physical mechanisms which govern the transport of neutrons are fundamentally different from that for fluids. The time-dependent neutron transport equation in integro-differential form is shown in Eq. 3.8.

$$\begin{aligned}
& \frac{1}{v(E)} \frac{d\psi(\vec{r}, E, \vec{\Omega}, t)}{dt} + \vec{\Omega} \cdot \nabla \psi(\vec{r}, E, \vec{\Omega}, t) + \Sigma_t(\vec{r}, E, t) \psi(\vec{r}, E, \vec{\Omega}, t) \\
&= \frac{\chi_p(E)}{4\pi} \int_0^\infty dE' \nu_p(E') \Sigma_f(\vec{r}, E', t) \phi(\vec{r}, E', t) \\
&+ \sum_{i=1}^N \frac{\chi_{d,i}(E)}{4\pi} \lambda_i C_i(\vec{r}, t) + \int_{4\pi} d\Omega' \int_0^\infty dE' \Sigma_s(\vec{r}, E' \rightarrow E, \Omega' \\
&\rightarrow \Omega, t) \psi(\vec{r}, E', \vec{\Omega}', t) + S(\vec{r}, E, \vec{\Omega}, t) \tag{3.8}
\end{aligned}$$

where v is the neutron speed, \vec{r} is the neutron position, E is the neutron energy, t is time, ψ is the angular flux, $\vec{\Omega}$ is the solid angle of the neutron's direction of motion, Σ_t is the total interaction macroscopic cross section, χ_p is the prompt-fission born neutron energy distribution, ν_p is the average number of neutrons born per prompt fission, Σ_f is the fission macroscopic cross section, ϕ is the neutron scalar flux, $\chi_{d,i}$ is the delayed neutron-born energy distribution, λ_i is the delayed neutron precursor decay constant of group i , C_i is the precursor atomic concentration, N is the number of precursor groups, and S is an arbitrary extraneous source. Fundamentally, this equation is expressing that the time rate increase of neutrons in a particular position, energy, and direction is equal to the production rate of neutrons in that space minus the loss rate of neutrons in that space. The first term on the LHS is the transient term; the second term is the net outleakage (a loss); the third term is the total interaction rate (a loss); the first term on the RHS is the neutron production due to prompt fission (a gain); the second term is the neutron production due to delayed precursor nuclide decays (a gain); the third term accounts for neutron in-scattering from outside-to-inside the phase space control volume

(a gain); and the fourth term represents an arbitrary source of neutrons external to the problem domain (a gain). Together, these terms account for the vast majority of neutron interactions, and Eq. 3.8 is generally applicable to any kind of nuclear reactor.

The solution strategy for the neutron transport equation will be discussed in the next section, but first, a few of the important phenomena found in a fast spectrum NTR are discussed:

1. **Spatial Flux Distribution.** From one-group neutron diffusion theory, the shape of the neutron flux in a bare cylindrical reactor represents a cosine function in the axial direction, and a zero-order Bessel function in the radial direction. Despite the complexity of a real reactor, this general flux shape still prevails, subject to local perturbations, unless deliberate design measures are taken to alter it. This shape has an associated peaking factor, due to the higher flux in the center, and given the assumption that energy generation is proportional to neutron flux.

In an NTR, it is standard to include an axial and radial neutron reflector. This has the effect of skewing the axial power towards the inlet end of the core, and producing a high-power region near the radial edge of the core. Both reflectors have the effect of reducing the peaking factor.

2. **Energy Flux Distribution.** Previous NTRs built to date have operated on a thermal or epithermal neutron energy spectrum. The average energy of neutrons causing fission in NERVA reactors ranged from 0.4 eV for Pewee to 6.5 eV for the Small Nuclear Rocket Engine (SNRE) [17]. By contrast, cermet NTRs contain no moderating materials (such as graphite), and most fissions occur at

neutron energies of several hundred keV or above. Since the average neutron has a longer mean free path in a fast reactor, the reactor spatial flux distribution is very tightly coupled across the whole core.

3. **Time-Dependent Behavior.** The fast neutron spectrum can have implications on the control of the reactor as well. Although the delayed neutron fraction is still similar to a thermal reactor, the prompt neutron lifetime is two to three orders of magnitude lower in the fast reactor. This means that, so long as reactivity changes stay under one dollar, the control of the fast NTR should not be much more difficult than a thermal NTR (except for a different thermal time constant). However, should a reactivity insertion of more than one dollar ever occur, the power excursion would happen very quickly and could be a safety issue.
4. **Burnup.** In traditional terrestrial-reactor analysis the change in core composition over a long time (days, weeks, and months) is a crucial determinant in overall reactor safety and economy. Fuel-pin swelling due to gaseous fission products and the buildup of reactivity-affecting nuclides are one of the primary failure modes considered. However, for an NTR, the entire operation time is on the order of hours, and despite the huge power densities at which they typically operate; the burnup of NTR fuel is not considered vital information for a conceptual analysis. Therefore, it is neglected in this study.
5. **Accident Scenario Safety.** There are many safety situations to consider with an NTR, during ground operations, launch, and in-space operations. One of the most important characteristics is the reactor's behavior in a launch accident – whether

it will be contained or not, and when it lands whether it will be subcritical or not. The most likely environment a reactor will land in following a launch accident is sea water, which if leaked into the core will introduce neutron moderation. Depending on the core void fraction, this moderation may or may not be enough to bring the reactor to critical. The specific threat and measures to protect against a supercritical-launch failure scenario depend on the specific reactor design.

3.6 Operating Principle of MCNP

Many methods are available for approximating solutions to the transport equation, but among the most widely used and highest-fidelity is the Monte Carlo method. The governing equation that is numerically approximated with the Monte Carlo method is the k-eigenvalue neutron transport equation, which is a modified version of Eq. 3.8 subject to the constraints of (1) Steady state operation, and (2) No external source is present, implying the core is operating in its fundamental mode. This equation is shown below.

$$[\vec{\Omega} \cdot \vec{\Delta} + \Sigma_T(\vec{r}, E)]\psi(\vec{r}, E, \vec{\Omega}) = \iint \psi(\vec{r}, E', \vec{\Omega}')\Sigma_s(\vec{r}, E' \rightarrow E, \vec{\Omega} \cdot \vec{\Omega}')d\Omega'dE' + \frac{1}{k_{eff}} \frac{\chi(E)}{4\pi} \iint \nu\Sigma_f(\vec{r}, E')\psi(\vec{r}, E', \vec{\Omega}')d\Omega'dE' \quad (3.9)$$

Equation 3.9 can be re-written in a simpler form:

$$(\mathbf{L} + \mathbf{T})\Psi = \mathbf{S}\Psi + \frac{1}{k_{eff}} \mathbf{M}\Psi \quad (3.10)$$

where \mathbf{L} is a leakage operator, \mathbf{T} is a total interaction operator, \mathbf{S} is a scattering operator, and \mathbf{M} is a fission source operator [39]. Equation 3.10 can be rearranged to give:

$$\Psi = \frac{1}{k_{eff}} (\mathbf{L} + \mathbf{T} - \mathbf{S})^{-1} \mathbf{M} \Psi = \frac{1}{k_{eff}} \mathbf{F} \Psi \quad (3.11)$$

This is now in a form that can be useful for numerical iterations. The power iteration method is posed in the following manner:

$$\Psi^{(n+1)} = \frac{1}{k_{eff}^{(n)}} \mathbf{F} \Psi^{(n)}, \quad n = 0, 1, \dots \quad (3.12)$$

Assuming that initial conditions are applied for k_{eff} and a guess for Ψ , Eq. 3.12 can be run for successive generations of particles until there is a satisfactory level of convergence.

The general numerical structure used in Monte Carlo codes such as MCNP is to simulate a “random walk” of a particle. In this method, there is first an initial assumption for the source energy and direction of a particle. Then, the free-flight distance that the particle travels is calculated using a random number weighted with the total interaction probability. At the location of the interaction, a number of parameters are calculated using probability density functions, including:

- Which nuclide the particle interacts with
- What type of interaction occurs (e.g. scatter or absorption)
- Energy and direction of the exiting particle
- Production of any secondary particles, and their energies and directions

In addition, tallies of the number of particles or other properties such as energy deposition may be recorded after each interaction.

3.7 Method for Energy Deposition Calculation

In MCNP5, the F4 or FMESH4 tally command will produce the average particle flux through each cell. For a criticality problem, the units are the average number of neutrons per cm^2 , per neutron of total flux.

$$\Phi_{F4} = \frac{\text{neutrons/cm}^2}{\text{neutron of total flux in the system}} \quad (3.13)$$

The FM4 multiplier card takes the F4 flux and does two things to it: (1) Integrates the flux with various cross-sections or other parameters over some energy range, and (2) Multiplies the result of that integration by some constant of the user's choosing. In Eq. 3.14 the output of the FM4 operation is denoted as T_{FM4} .

$$T_{FM4} = C \int_{E1}^{E2} \sigma_i(E) \Phi_{F4}(E) dE \quad (3.14)$$

In Eq. 3.14, σ_i can be any cross section (e.g. fission) and C is the multiplicative constant. T_{FM4} is what will actually be printed to the tally file ("meshtal"). In order to tally the fission energy deposition, the scalar flux Φ_{F4} [(neutrons/ cm^2)/neutron] must be integrated with the fission cross section σ_f [barns] and the energy deposited per fission Q_f [MeV/fission]. The units resulting from this integration are shown in Eq. 3.15.

$$\int_{E1}^{E2} \sigma_f [\text{barns}] \Phi_{F4} \left[\frac{n's/\text{cm}^2}{\text{total flux}} \right] Q_f \left[\frac{\text{MeV}}{\text{fission}} \right] dE = \left[\frac{\text{MeV}}{\text{total flux}} \right] \left[\frac{\text{barns}}{\text{cm}^2} \right] \quad (3.15)$$

Once the integration is done, the multiplication factor C needs to turn [MeV-barns/ cm^2 -flux] into [W/m^3]. First, the barns/ cm^2 is removed with a factor of 10^{-24} . Then, the total number of particles per second, C , is calculated using the required power, P :

$$C \left[\frac{\text{total system } n's}{s} \right] = \frac{(10^{-24})P[W]v \left[\frac{n's}{\text{fission}} \right]}{Q_f \left[\frac{\text{MeV}}{\text{fission}} \right] \left[1.6022 \times 10^{-13} \frac{J}{\text{MeV}} \right]} \quad (3.16)$$

After multiplying C by the result of the integration, the result is in units of [MeV-neutrons/s]. The final step is to multiply by the fissile atom density. MCNP will automatically multiply C by the fissile atom density [atoms/(barn-cm)] when C is specified with a negative sign in front of it. Now, the FM4 card will look like:

FM4 -C M -6 -8

where C is the result from step 4, M indicates which material number to use, the -6 specifies that the fission cross section σ_f will be integrated with the flux, and the -8 specifies that the fission energy deposition Q_f will also be integrated with the flux. If 0 is specified as the material number, MCNP will produce an average cross section based on the component atom densities that occupy the cell. This can produce skewed results if the 0 is specified for a mesh cell that occupies an unknown heterogeneous mix of materials.

The output of step 5 will be a power density, p , with units of [MeV/(barn-cm-s)]. A few unit conversions will bring this to W/m³:

$$p \left[\frac{W}{m^3} \right] = p \left[\frac{\text{MeV}}{\text{barn} - \text{cm} - \text{s}} \right] \left[1.6022 \times 10^{-13} \frac{J}{\text{MeV}} \right] \left[10^{24} \frac{\text{barns}}{\text{cm}^2} \right] \left[10^6 \frac{\text{cm}^3}{m^3} \right] \quad (3.17)$$

After writing Eq. 3.17 is becomes apparent that several terms cancel out. First, the fission energy deposition factor drops out, because it is present in the integration of step 3 and in the denominator of step 4. Next, the barns-cm² and the J-MeV conversion

factors cancel out between steps 4 and 6. As a result, the final specification for the FM4 card is:

FM4 -D M -6

where $D = P[W] \nu \left[\frac{ns}{fission} \right] \left[10^6 \frac{cm^3}{m^3} \right]$. The final tallies printed to the meshtal file will be in units of W/m^3 .

3.8 Applications of New Method

The combined CFD and neutronics methods described in the previous sections will be applied in three distinct efforts: The first is to benchmark the CFD methods against experimental data; the second is to use a simplified MCNP model and single-channel CFD simulation to perform a parametric study for guiding coolant channel design; and the third is to demonstrate a failure-mode stress analysis on one of the recommended fuel element designs from the parametric study. Each application is discussed further below.

1. **Benchmarking.** The fundamental conjugate heat transfer problem involving high temperature hydrogen will be benchmarked using two different sets of experimental data. The first set comes from a 1964 NASA experiment in which hydrogen was flowed through an electrically-heated tungsten tube [34]. The experimenters kept thorough records of the conditions of each trial, and recorded the axial temperature profile of the tungsten tube as well as the bulk fluid temperatures and pressure drop (the correlations from this investigation were in fact developed for the NERVA program). Comparison with the experimental

results will allow for an assessment of which meshing practices and turbulence models used in Star-CCM+ are most appropriate, and lend confidence to the CFD simulations.

However, the tungsten rod experiment falls short of being useful for a validation exercise due to a lack of reported experimental error. In order to better quantify the uncertainty in predicting peak fuel temperature, a second benchmarking simulation is built for comparison with measured data from an actual NERVA engine test. By analyzing the numerical, input, and experimental uncertainties that make up the validation exercise, an estimate of the overall uncertainty for temperature prediction can be obtained.

2. Parametric Study. Because no tungsten-cermet core has ever actually been built, there remains some uncertainty as to which fuel element design will meet all the performance requirements and safety margins. To address this, a parametric study will be performed to calculate the peak fuel temperature, bulk exit temperature, and pressure drop for different combinations of coolant channel size and number per element. The results will be useful for guiding trade studies on element design, and recommendations on the best channel configuration will be made.

The scope of the study will be limited to the design of a 10 klbf-thrust cermet NTR, since that is the most likely engine size to be built in the near future.

Although too small to power a piloted mission to Mars, the 10 klbf-thrust engine is the most practical size for a development program, and still offers many game-

changing advantages for unmanned deep space missions. A recent mission trade study suggested that this size would be ideally suited for a Mars sample return mission [40].

3. Multi-Element Failure Mode Analysis. While peak fuel temperature is one of the primary concerns in designing an NTR fuel element, other failure modes due to stress interactions in the fuel and cladding must be addressed as well. The common failure modes associated with a cermet NTR element can be due to any combination of temperature-gradient-induced thermal stress, coefficient of thermal expansion mismatch-induced thermal stress, and pressure-differential-induced stress. Each of these stresses will be examined in a multi-element model of one of the recommended fuel element designs from the parametric study. The primary goal of this effort is to evaluate Star-CCM+'s ability to identify stress-related problem areas; with the secondary goal of verifying the design itself.

4. UNCERTAINTY ASSESSMENT

Between the MCNP simulations, CFD simulations, and input data, there are many variables and potential sources of uncertainty that factor into calculating the performance of an NTR core. As mentioned previously, special care must be taken in particular for the NTR reactor as opposed to a typical power reactor, because of the tighter safety margins. Figure 4.1 shows the major contributors to uncertainty in the calculation of the performance of a particular core design.

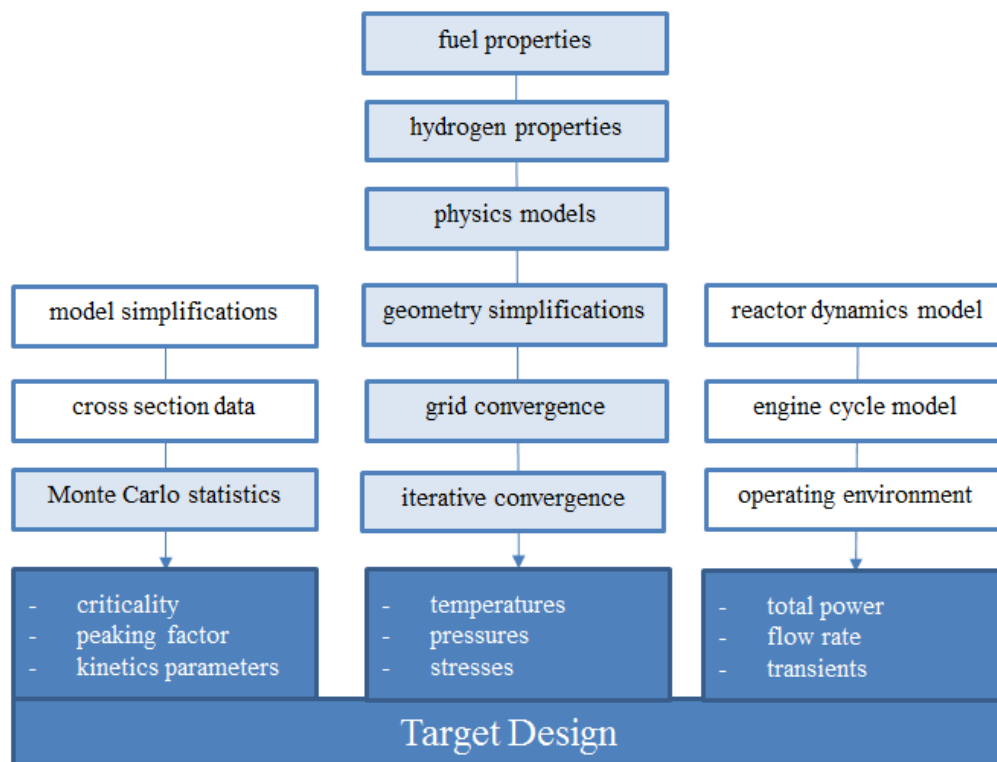


Fig. 4.1 Overview of the contributing factors to simulation uncertainty

Error sources which are shaded in light blue are addressed in this section. The other factors, though important, are of a complexity that requires a separate focused study. The uncertainties in fuel and hydrogen properties have been discussed in Section 3.4, but how much this propagates through the solution will be calculated in Section 4.4. Grid convergence will be assessed in Section 4.3, while it is explained in the next section that iterative convergence can be considered negligible. Uncertainties due to the physics models and any geometry simplifications will first be assessed by down-selecting the available physics models in Section 4.2, and then by quantifying the model error by a validation exercise in Section 4.5. The statistical uncertainty in the neutronics calculations will be discussed in Section 4.6. Finally, the net sum of these uncertainties will be discussed in Section 4.7.

4.1 CFD Uncertainty Quantification Methodology

The methods for CFD simulation uncertainty quantification in this thesis are based on the guidelines set forth in the American Society of Mechanical Engineering (ASME) standard “V&V 20 – 2009”: Standard for Verification and Validation in Computational Fluid Dynamics and Heat Transfer [41]. All notations and definitions are compliant with the conventions outlined in that standard.

The distinction must first be made between what is meant by *error* and *uncertainty*, as varying definitions may be found throughout CFD literature. For a given parameter, such as temperature or pressure, error is the difference between the measured or calculated value and the true, actual value. This quantity is in general hard to obtain and can only

be known for very particular conditions. Uncertainty, on the other hand, is an estimation of the standard deviation of the desired parameter, based upon a careful accounting of all the variables in the simulation or experiment. In this way, the uncertainty provides a range of probable values, within which lays the error.

Error and uncertainty quantification in a computational model are commonly addressed using a method of Verification and Validation (V&V). Verification encompasses two parts – code verification and solution verification, which assess the suitability of the physics model and discretization scheme. Once verification is established, validation is the practice of comparing a simulation to experimental data in order to quantify how well the model can predict the solution for a particular problem. The net error in any simulation is broadly attributed to three different sources [41]:

$$\delta_s = \delta_{model} + \delta_{num} + \delta_{input} \quad (4.1)$$

where δ_s is the total simulation error, δ_{model} is the error due to differences between the model's governing equations and the true physical behavior, δ_{num} is the error due to the numerical approximation of the governing equations, and δ_{input} is the error due to inaccuracies in input parameters, such as material properties. Each of these error sources are addressed in the following sections.

4.1.1 Code Verification

The goal of code verification is to ensure that the model is correctly solving the physics equations it is intended to, and this is typically done by comparison with analytical solutions. In this thesis, all of the CFD work uses a well-established

commercial program (Star-CCM+), and it is therefore assumed that all of the physics models that are used have already been verified. The Star-CCM+ manual includes many verification examples for users to explore [27].

4.1.2 Solution Verification

Solution verification is a means to estimate the uncertainty in the model resulting from numerical approximations. Referring back to Eq. 4.1, this would account for δ_{num} . Numerical errors can come into play due to iterative convergence and spatial convergence. However, by taking measures such as monitoring residuals and simulation variables, the iterative convergence error can usually be reduced to a point where it is two or three orders of magnitude less than spatial convergence error.

Many techniques have been proposed for assessing spatial convergence, and the Grid Convergence Index (GCI) will be used here. As outlined in ASME V&V 20, the GCI method comprises five basic steps. The first step is to establish which mesh parameter will be used as the main variable. This is not always a straight-forward choice, since the models developed for NTR channel analysis include a variety of different unstructured mesh regions which may encompass different degrees of cell stretching and other advanced effects. One suggestion for handling a complex unstructured mesh is to calculate an average cell characteristic length, h [41]:

$$h = \left[\left(\sum_{i=1}^N \Delta V_i \right) / N \right]^{1/3} \quad (4.2)$$

where ΔV_i is the volume of cell i , and N is the total number of cells.

The next step in the GCI method is to choose three values of the mesh variable to simulate, and select which simulation output parameter will be the basis for judging convergence. The mesh sizes can be any ratio to each other, although it is recommended that the minimum ratio is 1.3 [41]. For the conjugate heat transfer problems typical in NTR channel analysis, several solution parameters need to be tracked. Parameters of interest that are most relevant are the peak fuel temperature T_{\max} , the bulk hydrogen exit temperature T_{exit} , and the overall pressure drop ΔP . These selections are made because they are highly sensitive values which depend on the solution of the fluid region, the solid region, and the interface between the two. The convention for notation will be to denote the arbitrary parameter of interest as ϕ and the three mesh sizes as h_1 , h_2 , and h_3 (where $h_1 < h_2 < h_3$) [41].

The third step is to calculate the “observed” order of accuracy, p , of the model based upon the following equations.

$$p = \left[\frac{1}{\ln(r_{21})} \right] \left[\ln \frac{\varepsilon_{32}}{\varepsilon_{21}} + q(p) \right] \quad (4.3)$$

$$q(p) = \ln \left(\frac{r_{21}^p - s}{r_{32}^p - s} \right) \quad (4.4)$$

$$s = 1 \cdot \text{sign}(\varepsilon_{32}/\varepsilon_{21}) \quad (4.5)$$

where r_{21} is the ratio h_2/h_1 , r_{32} is the ratio h_3/h_2 , ε_{21} is $\phi_2 - \phi_1$, and ε_{32} is $\phi_3 - \phi_2$. The order of accuracy is a fundamental characteristic of a discretization scheme which indicates the behavior of the truncation error in relation to grid size [42]. For example, in a first-order scheme, the truncation error decreases in direct proportion with the grid size, Δx .

In a second-order scheme, the error will decrease more efficiently with the square of the grid size, $(\Delta x)^2$. The higher the order the better, and any order less than one would indicate an unstable discretization scheme.

The fourth step in the GCI process is to extrapolate the output parameter, ϕ , based on the first two simulations [41]:

$$\phi_{ext}^{21} = \frac{(r_{21}^p \phi_1 - \phi_2)}{(r_{21}^p - 1)} \quad (4.6)$$

Finally, the fifth step is to calculate the relative error and GCI as follows [41]:

$$e_a^{21} = \left| \frac{\phi_1 - \phi_2}{\phi_1} \right| \quad (4.7)$$

$$GCI_{fine}^{21} = \frac{F_s e_a^{21}}{r_{21}^p - 1} \quad (4.8)$$

For unstructured mesh problems, it is considered conservative to use an F_s of 3.0 (for structured grids a value of 1.25 is commonly used) [41]. The numerical uncertainty is then estimated:

$$u_{num} = \frac{GCI}{1.15} \quad (4.9)$$

It is common for the GCI calculation to be performed on a simplified version of the full-detail simulation it is representing – this is referred to as the nominal problem [41].

4.1.3 Input Sensitivity

The δ_{input} term accounts for all the uncertainties due to model inputs, such as material properties or boundary conditions. These uncertainties will be assessed using the Sensitivity Coefficient Method. This is also sometime referred to as the “local” method since it deals with relatively small perturbations in input values, in contrast to “global” methods such as Monte Carlo analysis. The basic idea in the sensitivity coefficient method is to calculate the change of some simulation parameter of interest with respect to an input parameter, and then multiply that derivative by the uncertainty of the input parameter. This relationship is written as [41]:

$$u_{input}^2 = \sum_{i=1}^n \left(\frac{\partial S}{\partial X_i} u_{X_i} \right)^2 = \sum_{i=1}^n \left(\bar{X}_i \frac{\partial S}{\partial X_i} \frac{u_{X_i}}{X_i} \right)^2 \quad (4.10)$$

where S is the simulation output parameter of interest, X_i is the input parameter, \bar{X}_i is the nominal input parameter value, and u_{X_i} is the uncertainty associated with that parameter. The source of the input uncertainties can come from a variety of places, and are frequently tabulated along with the original data or reported by the original experimenter.

The sensitivity coefficient in Eq. 4.10 can be calculated using a finite difference method in parameter space [41]. In this process, a baseline simulation run is first performed using the nominal input value \bar{X}_i , and then an additional run is performed with the input parameter perturbed by ΔX_i (so that the input value is $\bar{X}_i + \Delta X_i$). This first-order difference equation is written as

$$\frac{\partial S}{\partial X_i} = \frac{S(\bar{X}_i + \Delta X_i) - S(\bar{X}_i)}{\Delta X_i} \quad (4.11)$$

Care must be taken in selection of the input perturbation ΔX_i . If it is too small it may be affected by round-off error; too large and the truncation error of the first-order approximation may become significant. Once each uncertainty is determined, the relative importance of each input variable can be expressed using the importance factor, IF [41]:

$$IF = \frac{1}{u_{input}^2} \left(\bar{X}_i \frac{\partial S}{\partial X_i} \frac{u_{X_i}}{X_i} \right)^2 \quad (4.12)$$

4.1.4 Validation

The preceding discussions on grid convergence and input sensitivity account for estimates of δ_{num} and δ_{input} in Eq. 4.1. An estimate of the final piece, δ_{model} , is achieved by comparison of the simulation with experimental data. A validation experiment, ideally, will have carefully quantified conditions, data, and uncertainty, and represent the full complexity of the model. Experimental uncertainties may be systemic, such as a known bias in a thermocouple reading; or random, resulting from the unexplained variation of a repeated measurement. The details of estimating measurement uncertainty are not discussed in depth here, but, following ASME convention, will be accounted for within a value u_D . The validation uncertainty is then defined as [41]:

$$u_{val} = \sqrt{u_{num}^2 + u_{input}^2 + u_D^2} \quad (4.13)$$

If the simulation-predicted value of some parameter is S , and the experimentally-measured value is D , then the error between them is $E = S - D$, where E is known as the validation comparison error. Once E and u_{val} are known, the method for estimating δ_{model} becomes somewhat subjective. The relationship between all the uncertainty parameters is summarized in Eq. 4.4.14 [41]:

$$E = S - D = \delta_{model} + \delta_{num} + \delta_{input} - \delta_D \quad (4.14)$$

Of all the above variables: E is known; δ_{num} , δ_{input} , and δ_D are not known but their standard uncertainties (u_{num} , u_{input} , u_D) are; and δ_{model} is the primary unknown. Because none of the actual errors are known, the best that can be done is to calculate a range of probable values for δ_{model} , based on an assumed distribution of the standard uncertainties (e.g. constant or Gaussian). Essentially, E is an estimate of δ_{model} , and u_{val} is the standard uncertainty of that estimate.

The main outcome of the validation exercise is an assessment of the accuracy of the simulation methods. By assuming a particular distribution for the errors, error bars for a particular solution parameter can be determined.

4.2 Method Down-Select Model

Modern CFD packages such as Star-CCM+ present the user with many choices for meshing techniques, physics models, and solver settings. In order to parse through the different options and determine which are most appropriate for the NTR core application, a heat transfer experiment from 1964 was simulated [34]. The experiment

was originally performed for the Rover program in order to derive 1D empirical correlations for Nusselt number and friction pressure drop for high temperature hydrogen flows. In this case, it is used in order to tune the settings for CFD simulation.

It should be noted that this comparison to measured results only serves as a guide on the choice between the different models, but cannot be considered as a reliable assessment of the accuracy of the models. Since the uncertainty in the measurements is unknown (the actual peak temperature could be 100 degrees higher or lower, for example), the judgment on the accuracy of any models is reserved for the validation case which is investigated in Section 4.5.

A sketch of the experimental setup taken from the original report is shown in Fig. 4.2. It consisted a thin tungsten channel nine inches long which was resistively heated using a 15 kW power supply. Cold hydrogen would be injected into a mixing plenum and a pre-inlet tube in order to ensure developed flow before it entered the heated tungsten section. Bulk hydrogen temperature and pressure data were recorded at the inlet and outlet of the test section, and an axial temperature profile of the solid channel was measured using a combination of thermocouples and optical pyrometers. A series of three refractory radiation shields surround the test section in order to protect the surrounding chamber. A total of 23 different tests were run with both helium and hydrogen, and varying amounts of input power and mass flow rate.

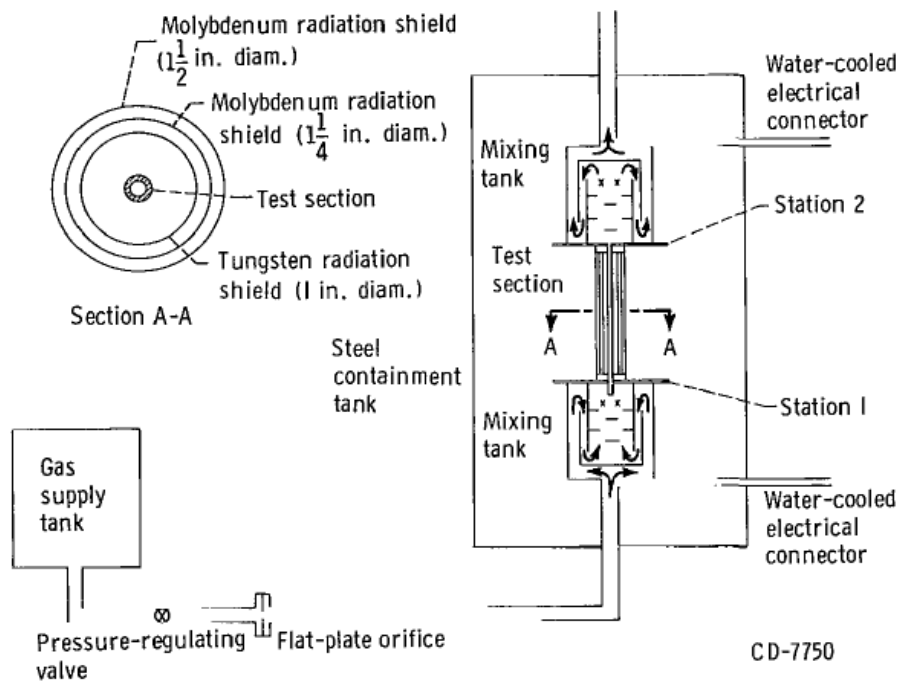


Figure 1. - Schematic diagram of arrangement of test apparatus.

Fig. 4.2 Diagram of experiment from Taylor [34]

The three tests which exhibited the closest conditions to an NTR channel were selected for benchmarking. Table 4.1 shows the setup parameters for each test.

Table 4.1 Experiment conditions used for benchmarking [34]

Run #	Mass Flow Rate (kg/s)	Inlet Pressure (kPa)	Current (amp)	Voltage Drop (V)	Power Deposited (kW)
20	0.000471	364.9	1244	8.85	11.01
21	0.000464	385.6	1280	10.0	12.80
23	0.000733	545.5	1440	11.1	15.98

The tungsten properties are set using field functions to account for changing temperature. Polynomial curves were generated for the specific heat and thermal conductivity of tungsten and are shown in Figures 4.3 and 4.4 [43]. A temperature polynomial was also generated for the emissivity of tungsten based upon data extracted from the original paper. The density was held constant since tungsten has a small coefficient of thermal expansion. A curve fit was similarly created for the electrical resistivity of tungsten.

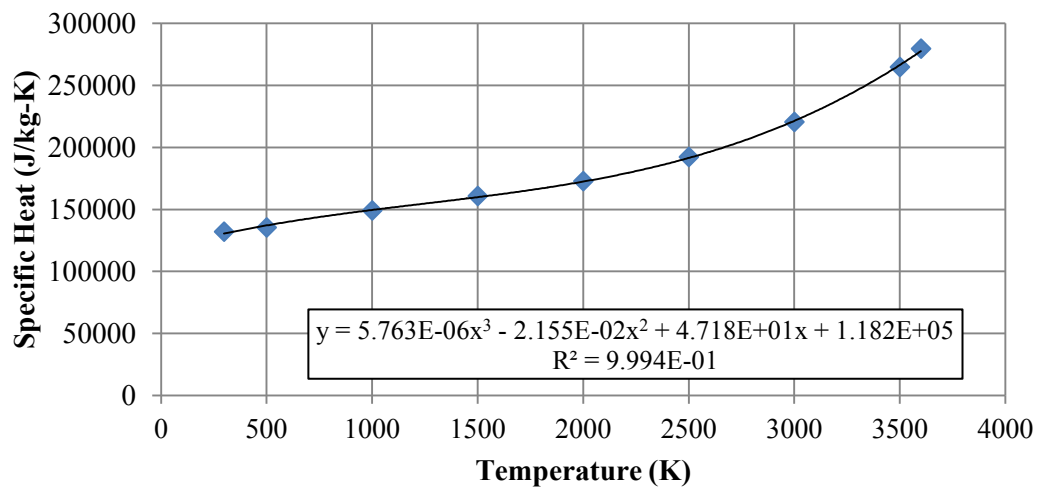


Fig. 4.3 Temperature polynomial for c_p of tungsten using data from Ref. [43]

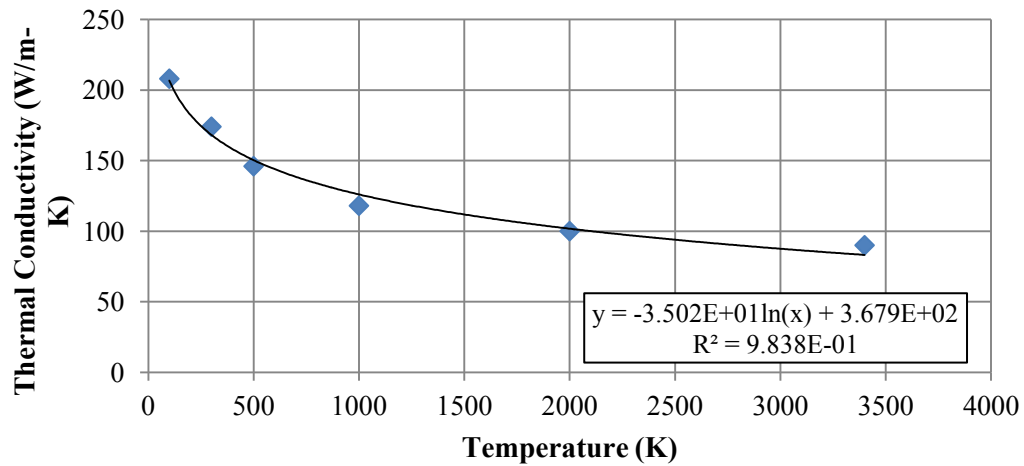


Fig. 4.4 Temperature regression for thermal conductivity of tungsten [43]

A baseline set of simulation parameters was first established based on experience and the “best practices” for general CFD setups. This case is referenced as case A21-0, where 21 stands for experimental run number 21. Case A21-0 uses a conformal polyhedral mesh for the hydrogen and tungsten channel regions, and a one-cell-thick tetrahedral “thin mesh” for the radiation shields. A pressure outlet is specified at the fluid exit, and a mass flow inlet is specified at the entrance. Star-CCM+ does not always match exactly the specified mass flow, but generally comes to within 1% of the desired value.

One significant simplification of the model relative to the experiment is the specification of the tungsten rod temperature at the inlet and outlet. In the experiment each end was attached to a water-cooled copper flange; however not enough detail is provided to accurately model these components. Therefore, the inlet and outlet faces of

the tungsten channel have simple specified temperature boundary conditions. This is not expected to have significant impact on the solution parameters of interest, but does result in a noticeable difference in the shape of the axial temperature profile.

Heat transport to the radiation shields is modeled using Star-CCM+'s Surface-to-Surface (S2S) radiation model with an assumed gray thermal spectrum. The radiation patch resolution is decreased to 0.5% of the default value in order to reduce the number of required view factors and increase computation speed, since the temperature distribution in the radiation shields is not of interest.

Using case A21-0 as a starting point, the following sections investigate the effect of changing one simulation parameter at a time. Figure 4.5 shows a snapshot of a typical temperature distribution in the model.

In general the ohmic heating of the tungsten rod will not be uniform. In order to account for the non-uniform energy distribution in the rod, a comparison was run for three different modeling options. The first case, A21-0, uses a relationship that was developed to account for the fact that power deposition is proportional to the resistance (Joule's law: $Q=I^2R$) on a cell-by-cell level. This formula is shown in Eq. 4.15.

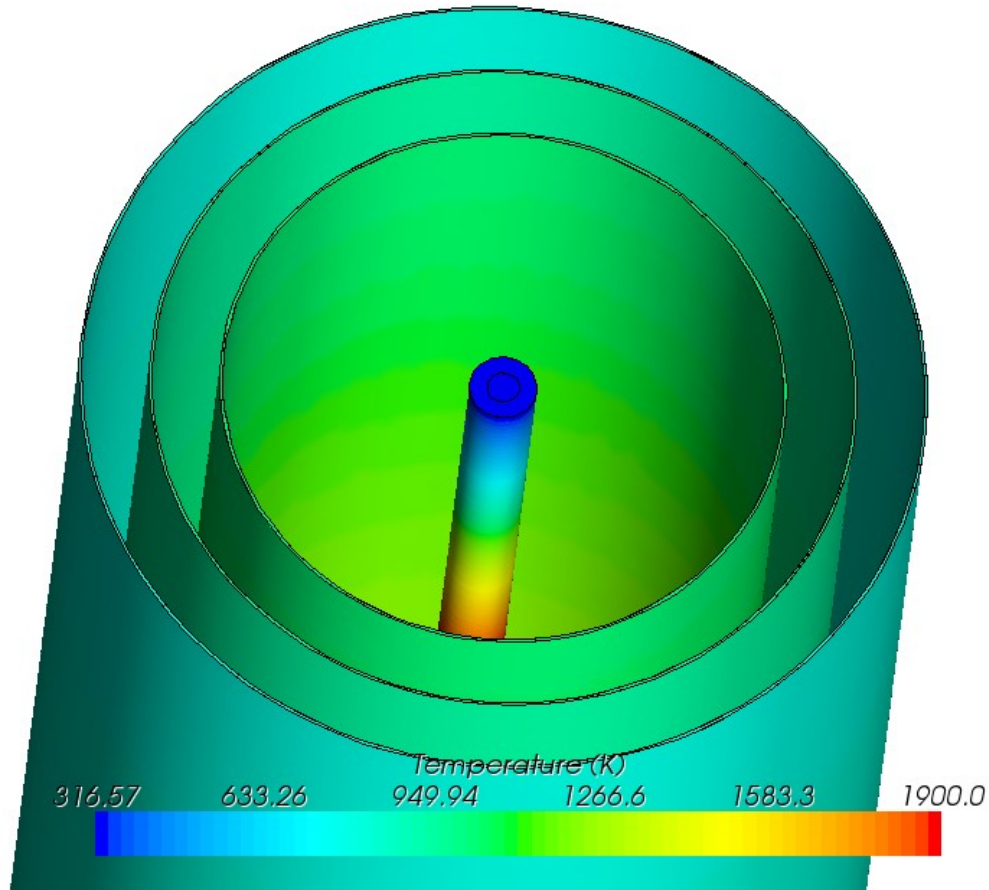


Fig. 4.5 Snapshot of temperature distribution in method down-select model

$$q'''_i = C \left(I^2 \frac{\rho(T)L}{A} \right) / V = C \frac{I^2 \rho(T)}{A^2} \quad (4.15)$$

where q''' is the volumetric heat generation in cell i in W/m^3 , I is the current in amps, ρ is the resistivity in ohm-meters as a function of the temperature in cell i , L is the length of the rod, A is the cross sectional area of the rod, V is the voltage potential drop across

the test section, and C is a correction factor. This formula introduces an added level of complexity to the simulation since the heat generation and temperature become implicitly coupled. In order to reach a converged solution, the factor C must be actively adjusted until the total power deposited matches the experimental value, and all other simulation parameters have converged as well.

The second method for applying the ohmic heat deposition uses a simple uniform distribution, in which the total power deposited is divided by the tungsten channel volume. The final and most complex method utilizes Star-CCM+'s Ohmic Heating model as part of its Electromagnetism module [27]. In this model Star-CCM+ models the electric field inside the tungsten rod, and adds an electrical source term to the conservation of energy equation.

The results of each modeling method are shown in Table 4.2.

Table 4.2 Simulation results for different power shape methods

Case	Description	Bulk Exit Temperature (K)	Peak W Temperature (K)	Pressure Drop (kPa)
Experiment 21	measured	1506	3080	274.8
A21-0	variable power generation	1516	2879	317.3
A21-1	uniform power generation	1420	2549	313.0
A21-2	ohmic heating model	1517	2720	324.4

Out of the three electrical heating models tried, the variable power generation according to Eq. 4.15 is the most accurate for matching experimental run 21. The Electromagnetic model, A21-2, also comes reasonably close, particularly with the bulk exit temperature. However, it underpredicts the peak temperature by a significant margin compared to the Joule's law model, and solves at a slower pace. The uniform energy deposition model, as expected, produces the least accurate results.

4.2.1 Mesh Type

Star-CCM+ offers three different mesh cell types that are relevant to this simulation: polyhedral cells, tetrahedral cells, and a trimmer mesh. Each is an unstructured grid. In order to compare which mesh type is most suitable to the hydrogen conjugate heat transfer problem, three test cases were run based on experiment run 21. Figure 4.6 shows a snapshot of each of the three mesh types applied to the tungsten channel (the tan center is the fluid region).

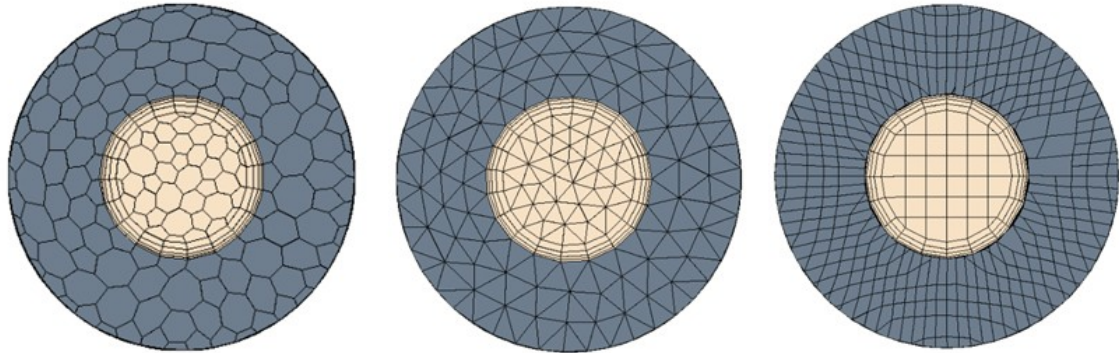


Fig. 4.6 Polyhedral mesh (left), tetrahedral mesh (center), and trimmer mesh (right) for the tungsten channel.

The results from using each mesh type are shown in Table 4.3.

Table 4.3 Simulation results for different mesh types

Case	Description	Bulk Exit Temperature (K)	Peak W Temperature (K)	Pressure Drop (kPa)	# cells	Average time per iteration (s)
Experiment 21	measured	1506	3080	274.8	--	--
C21-0	polyhedral cells	1516	2879	317.3	246077	0.79
C21-1	tetrahedral cells	1521	2953	315.6	561919	1.82
C21-2	trimmer mesh	1479	2966	331.2	246886	0.91

Despite the tetrahedral cells and trimmer mesh producing better-matching results for peak temperature, other computational constraints necessitate the use of the polyhedral mesher. First, the polyhedral mesher results in the fewest number of cells, and as a result requires the shortest amount of elapsed time to solution – less than half the time of that required by the tetrahedral mesh. In addition, the latest addition of Star-CCM+ (7.02.011 at this time) offers parallel meshing for polyhedral cells, but none of the others. While the meshing time is not an important factor for small cases, it is very significant for larger cases such as a full core model, where meshing time can take up to several days.

Once Star-CCM+ gains the ability to execute the tetrahedral and trimmer mesh generators in parallel, this discrepancy should be investigated further, and future studies should perhaps switch to the trimmer mesh. However, it is important to re-state that because the experimental uncertainty of the temperature data is unknown, the results in Table 4.3 do not definitively mean that one mesh type is more accurate than another.

4.2.2 Conformal versus Non-Conformal Mesh

The energy transport across the fluid-solid boundary is very sensitive to the quality and resolution of the mesh. It is important that adjacent cells on the interface make 100% contact with each other in order to ensure realistic transport of energy across the boundary. Star-CCM+ offers the ability to mesh the fluid-solid parts in one seamless mesh region (conformal interface), or in two separate, different-sized mesh regions (non-conformal interface). The results after using each type are shown in Table 4.4.

Table 4.4 Simulation results for a conformal and non-conformal mesh interface

Case	Description	Bulk Exit Temperature (K)	Peak W Temperature (K)	Pressure Drop (kPa)	# cells
Measured	experiment	1506	3080	274.8	--
D21-0	conformal interface	1516	2879	317.3	246077
D21-1	non-conformal interface	1536	2900	326.6	177897

It can be seen that there is not a large difference in the results between the conformal and non-conformal meshes. This result is important, since for large-scale simulations, it is highly desirable to have less resolution in the solid region than the fluid region in order to save computational resources; therefore the non-conformal interface needs to be used.

For all small-scale (sub-channel or fuel element) simulations in this report, the conformal interface is used since it is known to be a better practice. However, for larger simulations, computer and time constraints require that the non-conformal interface be used.

4.2.3 Turbulence Model

Due to the large-scale of the intended problems for NTR simulation, the choice was made to use Reynolds-Averaged Navier-Stokes (RANS) methods for calculating the effect of turbulence. Other methods such as Large Eddy Simulation or Direct Numerical

Simulation require vast amounts of computational power and to date have only been applied to small-scale problems.

RANS models are themselves an empirical method for resolving turbulence, and as such there have been many RANS models developed. Two of the most common eddy-viscosity models which Star-CCM+ supports are the k-epsilon and the k-omega models. In order to survey a range of the available models, four turbulence models have been selected: the k- ϵ 2-layer realizable model, the k- ϵ V2F low-Reynolds model, the k- Ω SST Menter model, and the k- ϵ AKN model. Each of these models were used for simulating experiment runs 20, 21, and 23, and these results are shown in Table 4.5.

The average errors that each turbulence model produced with respect to the measured data are summarized in Table 4.6. From the results in Table 4.6, it is apparent that both the k- ϵ 2-layer realizable model and the k- ϵ V2F model have advantages and disadvantages. The 2-layer realizable model performs excellently with respect to the bulk exit temperature, but significantly under-predicts the measured peak temperature. On the other hand, the V2F model has the smallest error for peak temperature, but does poorly for predicting the bulk exit temperature. The other two models do not provide any advantage over the first two, except for pressure drop, although pressure drop accuracy is given lower priority.

Table 4.5 Simulation results for different turbulence models

Case	Description	Bulk Exit Temperature (K)	Peak W Temperature (K)	Pressure Drop (kPa)	Wall y^+
Experiment 20	measured	1326	2948	259.6	--
E20-0	k- ϵ 2-layer realizable turbulence	1335	2672	300.0	1.002
E20-1	k- ϵ V2F turbulence	1226	3028	292.3	0.658
E20-2	k- Ω SST Menter turbulence	1233	3067	291.0	0.714
E20-3	k- ϵ AKN turbulence	1228	3017	291.6	0.658
Experiment 21	measured	1506	3080	274.8	--
E21-0	k- ϵ 2-layer realizable turbulence	1511	2900	320.6	0.945
E21-1	k- ϵ V2F turbulence	1396	3186	309.6	0.641
E21-2	k- Ω SST Menter turbulence	1401	3210	308.9	0.683
E21-3	k- ϵ AKN turbulence	1394	3174	310.3	0.642
Experiment 23	measured	1384	3124	375	--
E23-0	k- ϵ 2-layer realizable turbulence	1305	2726	430.2	1.282
E23-1	k- ϵ V2F turbulence	1187	3280	417.8	0.811
E23-2	k- Ω SST Menter turbulence	1195	3338	416.4	0.934
E23-3	k- ϵ AKN turbulence	1196	3472	415.1	1.205

Table 4.6 Percent errors from measurements for each turbulence model

Turbulence Model	Average Bulk Exit Temperature Error	Average Peak W Temperature Error	Average Pressure Drop Error
k- ϵ 2-layer realizable turbulence	-1.6%	-9.3%	+15.7%
k- ϵ V2F turbulence	-9.7%	+3.7%	+12.2%
k- Ω SST Menter turbulence	-9.2%	+5.0%	+11.9%
k- ϵ AKN turbulence	-9.5%	+5.5%	+12.0%

The best performing models, k- ϵ 2-layer realizable and k- ϵ V2F, were compared for their stability with respect to mesh refinement. For each model, the boundary layer refinement was adjusted and the peak tungsten temperature was recorded. These results are shown graphically in Fig. 4.7.

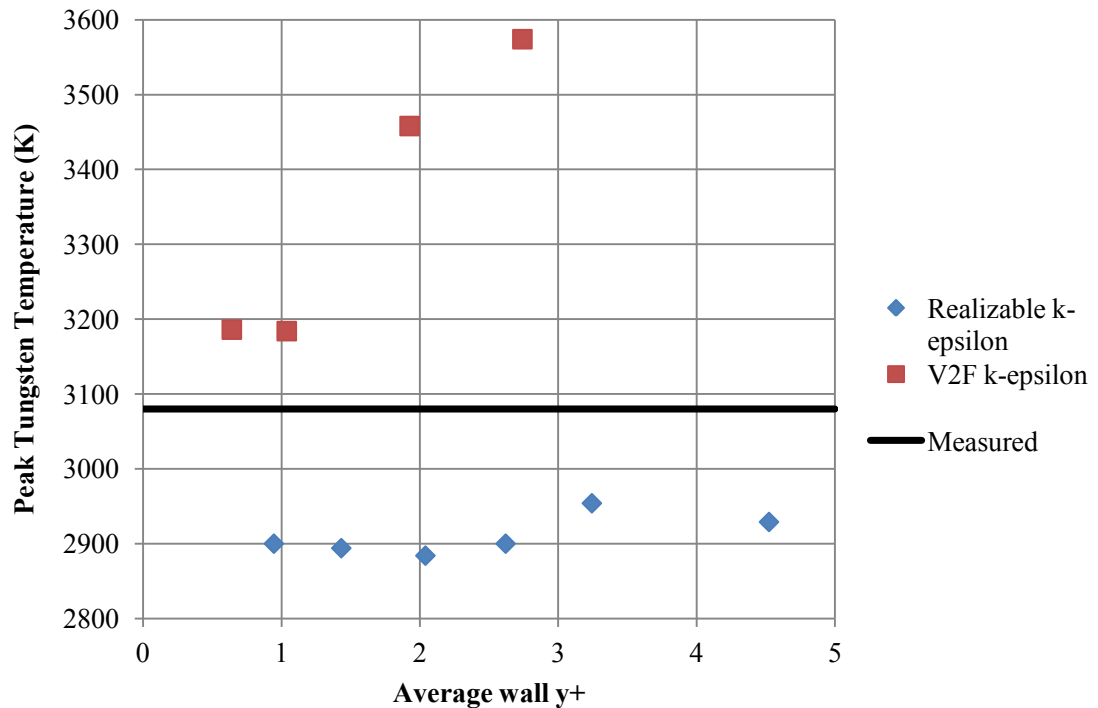


Fig. 4.7 Peak temperature as a function of average y^+ of cells at the wall

There is a very drastic divergence in the solution of the V2F model between a wall y^+ of 1.04 and 1.93. Below 1.04 however, the solution is very consistent. For the Realizable two-layer model, the divergence is much more gradual, and the trend is somewhat clouded by other numerical effects taking place. For realizable two-layer cases with a wall y^+ of 2.62 and below, there is a standard deviation of approximately 6.5 degrees from the average solution.

Despite the fact that the V2F model produces a closer and more conservative prediction of the peak temperature, the instability of the mesh for wall y^+ 's greater than

one is a cause for concern for two reasons. First, the reported wall y^+ is only an average of all cell values – there are certainly many cells or entire sections of the channel which have a wall y^+ significantly higher than the reported value. The divergence seen in Fig. 4.7 suggests that the V2F solution in these regions may be very inaccurate. Second, a requirement to resolve all fluid regions down to a wall y^+ of 1.0 or less would require a very fine mesh and drive up the computational resources required for a full-core simulation. Therefore, because of its grid stability and reasonable prediction accuracy, the Realizable two-layer k-epsilon turbulence model is selected for all subsequent simulations.

Another recent study compared the available turbulence models in Star-CD (an earlier version of Star-CCM+) for resolving conjugate heat transfer in a heated channel [44]. For each turbulence model, the wall y^+ was varied from 0.21 to 2.1 for a Reynolds number of 6000. The researchers also found that the V2F model could accurately match experimental data, but is highly sensitive to grid resolution; while the k-epsilon model converged fairly easily [44]. Chen et al. also investigated the effect of specifying inlet turbulence on the simulation output, and found that for large Reynolds numbers of at least 9000, the inlet turbulence intensity has a negligible effect. Since all the flow of interest in an NTR fuel element have $Re > 10,000$, the effect of turbulent intensity was not independently investigated.

4.3 Grid Convergence Assessment

While the experiment benchmark is sufficient for evaluating most of the heat transfer physics involved, it does not provide enough geometric detail in the solid region to account for the complexity of heat conduction that is seen in a typical NTR fuel element.

In order to determine what grid size is required to assure spatial convergence, a model of a unit cell of a sample fuel element was built and meshed for range of mesh size settings. This model, which is known as the “nominal problem,” is of significantly smaller size than full fuel element or core simulations, however it contains the same fundamental repeating detail of those larger models. The general technique used for assessing convergence is the Grid Convergence Index (GCI), as discussed in Section 4.1.2.

4.3.1 Axial Coarsening

Various meshing software packages were investigated before settling on Star-CCM+'s native mesher, including Gambit, GridGen, Salome, and BlockMesh. Star-CCM+ was ultimately selected for its versatility in generating meshes for the large full-core problems. However, one disadvantage of the Star-CCM+ mesher is its lack of a treatment for long, slender geometries where length-wise grid resolution is less important than transverse resolution. The “generalized cylinder” feature is a step towards addressing the issue, but is not yet capable of handling complex, non-circular geometry. Currently, the mesh generators in Star-CCM+ produce grids with much more resolution in the axial direction than is necessary, which drives up computational costs severely.

To work around this, a simple technique was developed to axially stretch the mesh. The process involves scaling the model geometry down in the z-direction by some factor $1/x$ before meshing, then re-scaling it by x to full size after meshing. Since it is unknown how this practice will affect the stability of the mesh, a basic convergence check is performed on the nominal model. Results for axial stretching factors ranging from 1 (no coarsening) to 5 are shown in Table 4.7.

Table 4.7 Simulation results for different axial stretching factors

Stretching Factor	Peak Fuel Temperature (K)	Bulk Exit Temperature (K)	Pressure Drop (kPa)	Wall y^+	Max skewness angle (deg)
1	2990	2844	761.6	2.584	57.2
2	2998	2844	753.4	2.546	71.1
3	3002	2842	743.0	2.526	81.5
4	3004	2843	737.3	2.484	83.3
5	3007	2844	748.1	2.480	83.8

Three main parameters were tracked – peak fuel temperature, bulk exit temperature, and pressure drop. The peak fuel temperature showed a steady, but small, rise as the stretching factor increased. The total percent difference from the factor-of-5 stretched grid to the original grid is 0.57%. The bulk exit temperature showed no appreciable change at all. Finally, the pressure drop was the most variable of the three parameters, dropping by as much as 3.2%. The change in pressure was not monotonic with the stretching factor, however. The percent errors for each parameter are plotted in Fig. 4.8.

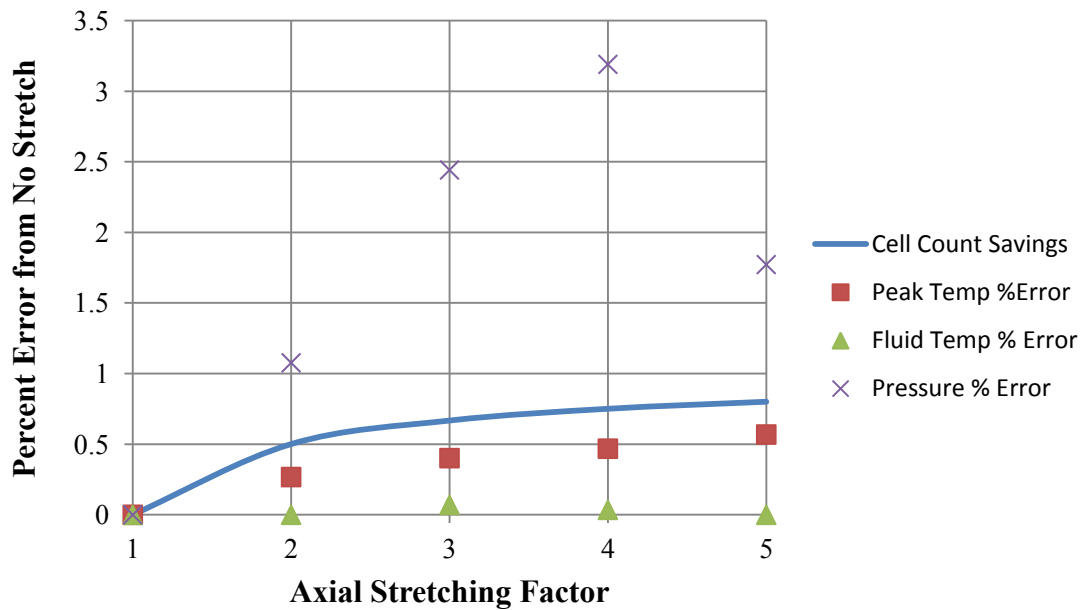


Fig. 4.8 The change in simulation results as a function of stretching factor

The blue curve is included to illustrate the cell count savings as the factor increases (it is arbitrarily normalized). Based on these results, the decision is made to use an axial stretching factor of 4.0.

Precedent for this type of axial coarsening has also been found in other studies which use Star-CCM+. Researchers at the Argonne National Lab have used the method in their analysis of a wire-wrapped sodium-cooled fast reactor fuel bundle [45]. In that study, reasonable convergence was shown for nominal cell aspect ratios of up to 1:16.

4.3.2 Grid Convergence Index

As mentioned in Section 4.1.2, there is no definitive way to measure the grid size for a complex mesh with many different regions, so Eq. 4.2 was tried as an of estimate the average cell dimension. In each case for the nominal problem, the only parameter changed is the “base size” of the mesh, which is conformal for both the fluid and solid regions. The ratio of base sizes between successive cases is held constant at 1.8. Due to the presence of a fine prism layer in the fluid region, a separate average cell size is tracked for the fluid and solid. Table 4.8 shows the cell base sizes used in each case, and the resulting solution parameters.

Table 4.8 Simulations results for different base size refinements

Case	Base Size (cm)	Peak Fuel Temp (K)	Bulk Exit Temp (K)	Pressure Drop (kPa)	Wall y^+
GCI-1	0.0333	3000	2841	724.0	1.427
GCI-2	0.0600	3004	2843	737.3	2.484
GCI-3	0.1080	3016	2851	775.7	4.305

It should be noted that the mesh was noticeably less stable in solving case GCI-3, as the residuals were very oscillatory and the under-relaxation factors needed to be reduced to achieve convergence. In calculating the order of accuracy, it was found that using Eq. 4.2 for the average cell size produced unrealistic results (greater than the ideal order of accuracy). Therefore, the base size was used as the average cell size, which is the same

for both the fluid and solid regions. Even though base size is not necessarily representative of the true average cell size, all mesh parameters are held constant (as some proportion of base size) between the different cases, so the ratios r_{32} and r_{21} in Eqs. 4.3 through 4.8 should be conserved.

The calculated order of accuracy (p) and numerical uncertainty for each solution parameter are shown in Table 4.9. The GCI uncertainty column includes the values calculated using the Grid Convergence Index, and the Coarsening uncertainty column includes the uncertainty resulting from using an axial stretching factor 4.0, which was determined in Section 4.3.1. These values are summed in quadrature to arrive at an estimate of the total numerical uncertainty, u_{num} .

Table 4.9 Order of accuracy, grid convergence index, and numerical uncertainty

Parameter	p	GCI uncert.	Coarsening uncert.	u_{num}
Peak solid temp	1.423	0.346%	0.468%	0.582%
Hydrogen exit temp	1.979	0.104%	0.035%	0.110%
Pressure Drop	1.804	2.539%	3.191%	4.078%

The theoretical order of accuracy for the modeling schemes selected in Star-CCM+ is 2.0, and it is expected that the actual order is somewhat less than that. This is in large part due to the presence of non-ideal, unstructured cell shapes, some of which have large skewness angles. Overall, the numerical uncertainty is reasonably small for the solid and

fluid temperatures, but relatively large for the pressure drop, at 4%. It has already been seen in cases with the Method Down-select model that the pressure drop is the least accurately-predicted parameter.

4.4 Sensitivity Coefficient Calculation

Five variables are examined for their impact on the solution: Solid thermal conductivity, fluid thermal conductivity, fluid specific heat, fluid viscosity, and volumetric energy generation. The nominal model used for the study is taken from Case 3 of the parametric study (see Section 5.3.2). In each case, one of the variables is perturbed and the effects on solution parameters are recorded. Although many of the variables are functions of temperature, for simplicity the entire function is scaled by a constant perturbation. These results are shown in Table 4.10.

Table 4.10 Simulation results for different variable perturbations

Case	Variable	Perturbation	Peak Fuel Temp (K)	Bulk Exit Temp (K)	Pressure Drop (kPa)
Sens-0	Nominal	--	3004	2843	737.3
Sens-1	k_fuel	+20%	2989	2843	737.2
Sens-2	k_H2	+10%	2997	2844	743.5
Sens-3	cp_H2	+10%	2863	2685	684.1
Sens-4	mu_H2	+10%	3000	2843	760.3
Sens-5	q'''	+10%	3168	3009	795.7

The errors are propagated through using Eqs. 4.10 and 4.11 from Section 4.1.3. The mean value used for each variable is evaluated at the average temperature from case Sens-0, which is 1752 K for the hydrogen and 2342 K for the fuel. These results are shown in Table 4.11.

Table 4.11 Input uncertainties for each solution parameter for a set of assumed variable relative uncertainties.

Parameter	Absolute u_{input}	Relative u_{input}	Variable	Relative uncertainty
Peak Fuel Temp	67.0 K	2.230%	k_fuel	20.0%
Hydrogen Exit Temp	68.8 K	2.419%	k_H2	10.0%
Pressure Drop	27.1 kPa	3.670%	cp_H2	3.0%
			mu_H2	5.0%
			q'''	3.0%

The results of u_{input} shown in Table 4.11 are specific to the assumed relative uncertainties of each variable. Depending on the case, the material property uncertainties should remain the same, however the volumetric energy generation uncertainty is subject to change. It has an assumed uncertainty of 3% here, but will be refined when discussing each case. As discussed in Section 4.1.3, the relative importance of each input variable in influencing the solution can be quantified via importance factors. These importance factors are visualized for each parameter in Figures 4.9, 4.10, and 4.11.

Input Importance for Fuel Temperature

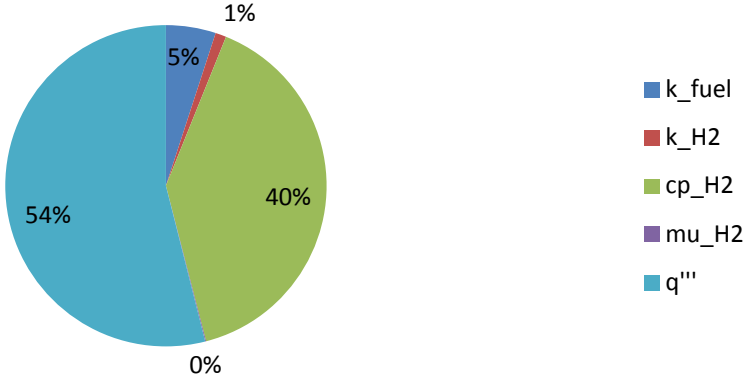


Fig. 4.9 Relative importance of input variables for calculating fuel temperature uncertainty

Input Importance for Hydrogen Temperature

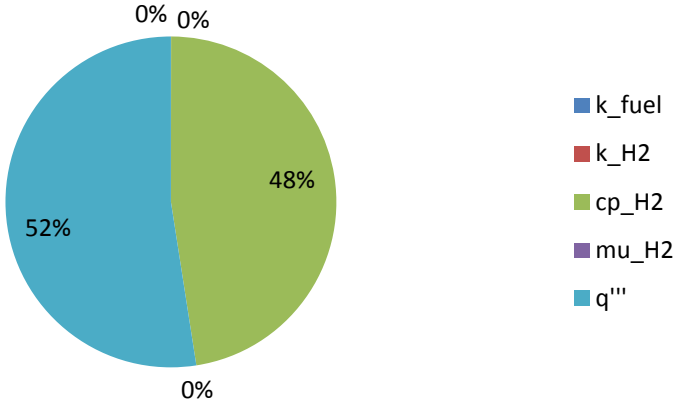


Fig. 4.10 Relative importance of input variables for calculating hydrogen temperature uncertainty

Input Importance for Pressure Drop

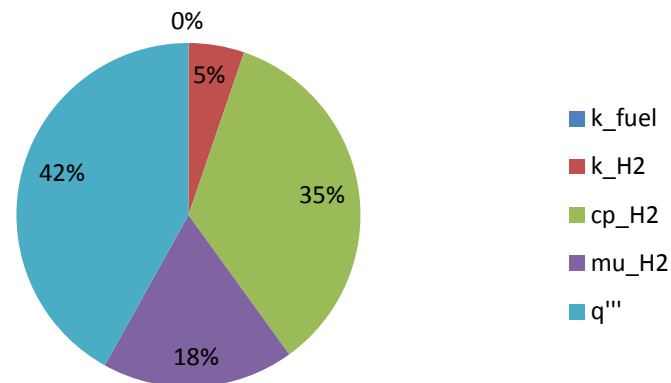


Fig. 4.11 Relative importance of input variables for calculating pressure drop uncertainty

It is readily apparent that the volumetric energy generation accounts for about half of the input uncertainty for all solution parameters. Equally as important is the specific heat of hydrogen. The hydrogen thermal conductivity and specific heat both play a significant role in the determination of pressure drop, but are negligible in their influence on temperature.

For the fuel temperature, the fuel thermal conductivity plays a minor, but still significant role. It is convenient that the thermal conductivity has a relatively small influence, since it is the most uncertain of all parameters. This result is somewhat surprising, and it was investigated whether or not the temperature drop between the wall temperature and centerline temperature is large enough for the 20% perturbation to be significant. For the particular geometry chosen for the sensitivity study, there is a 74 K

temperature rise at the peak location; the thermal conductivity perturbation reduces this to 59 K. Relative to the overall temperature, however, this change is small.

To address the universality of the sensitivity study nominal case, the study was repeated for a different sample element (Case 6 from Section 5.3.2), which has a wall-to-centerline ΔT of 377 K. It was found that the overall relative uncertainties did not change by more than 15%. Therefore, the sensitivity coefficients are considered valid for most geometries, with the understanding that it can fluctuate to an extent. However, as expected, the relative influence of each variable did change for the new case, and this time the fuel thermal conductivity *did* play a large role in determining the peak temperature. The importance factors are charted in Fig. 4.11.

Input Importance for Fuel Temperature with Large ΔT

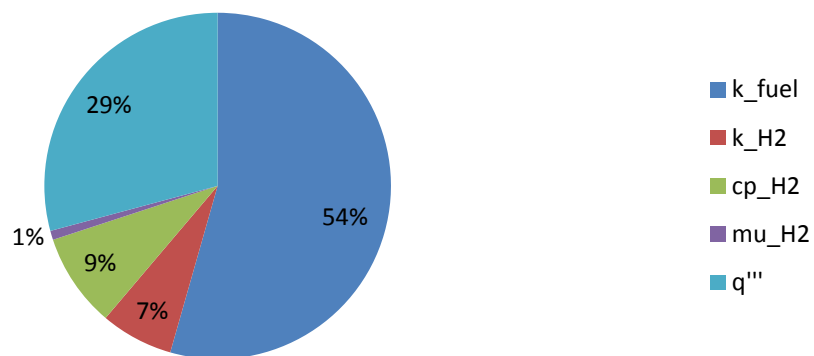


Fig. 4.12 Relative importance of input variables for calculating fuel temperature uncertainty, large ΔT case

The distribution of importance factors did not change appreciably for the hydrogen temperature or pressure drop.

Because of the varying role of thermal conductivity depending on the ΔT , it has been decided to use one of two set of sensitivity coefficients for subsequent simulations. For small wall-to-peal ΔT cases, the set exemplified by Fig. 4.9 is most appropriate; for large ΔT cases, the latter set shown in Fig. 4.12 should be used. The ΔT cutoff can be considered in the neighborhood of 100 K.

4.5 Validation Model

An attempt is made to validate the CFD simulation methods by comparison with actual NERVA data. The NRX series of engines followed the KIWI reactor tests in 1968, and were tasked with six main objectives, the first three of which were (1) Run at full power and temperature for 60 minutes, (2) Demonstrate stable operation of the bleed cycle, and (3) “Provide necessary information for the design of future reactor and engine systems” [46]. All objectives were ultimately met, but it is that third objective which will be capitalized on in this analysis.

4.5.1 Model Setup

During test number EP-III A of the series, several fuel elements were instrumented with thermocouples and thermal capsules (which record the highest temperature seen over a period of time). The high-temperature tungsten / tungsten-rhenium thermocouples were placed into narrow holes (approximately 0.16 cm diameter) drilled into the web of a fuel element down to various depths, or axial stations. This measurement is therefore

representative of a temperature somewhere between the average and peak temperature of the fuel at that location. The typical placement of these thermocouples is shown in Fig. 4.13, where the drawing on the right is indicating a thermocouple placed at Station 1.

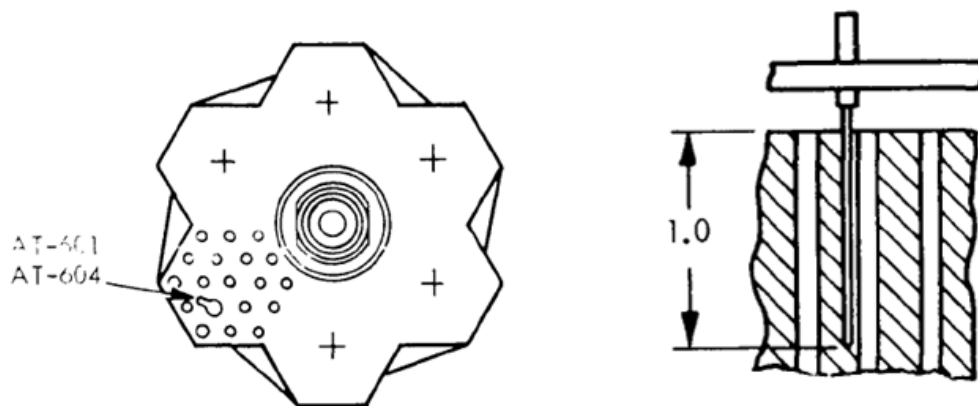


Fig. 4.13 Typical placement of a fuel element thermocouple in the NRX-A6 test; cross-sectional view (left), and profile view (right) [35]

The NRX-A6 final report contains the axial temperature data for a central-region fuel element taken at control room time (CRT) 17800 [46]. The data were extracted from the report using the open source MATLAB utility grabit.m, and are shown in Fig. 4.14. A few extra data points were collected from the published curve which do not necessarily correspond thermocouple measurements.

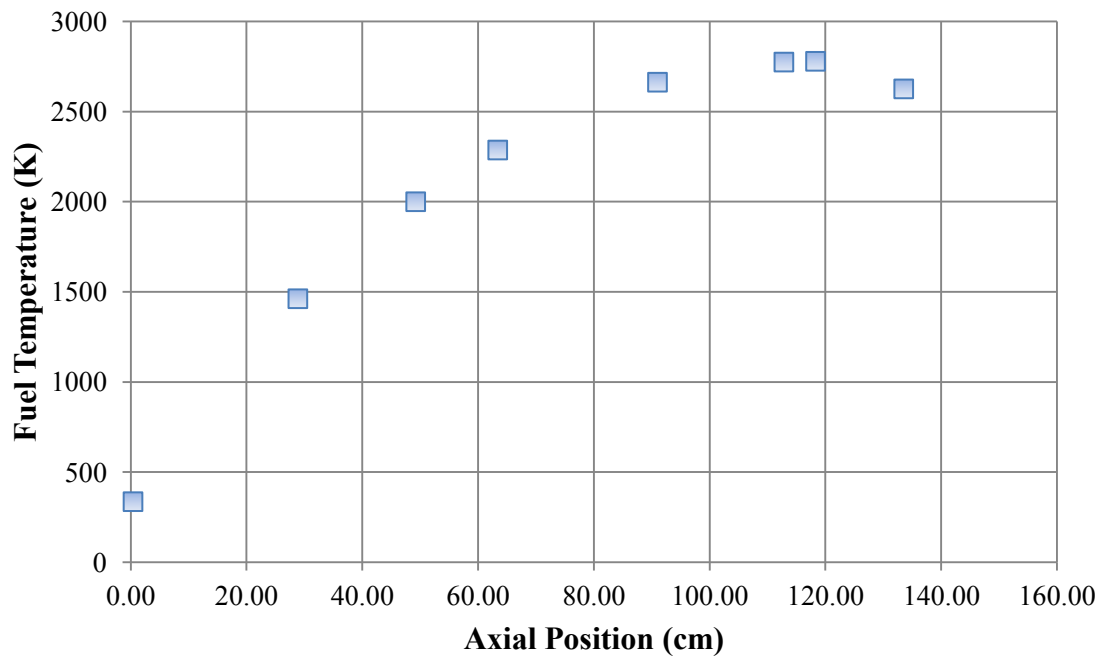


Fig. 4.14 Extracted temperature measurements from the NRX-A6 final report

It is noted that the NRX-A6 is certainly not an ideal validation case, because of several unknowns regarding how the data were collected and the precise conditions in the fuel element. Some consideration went into using the tungsten rod experiment used for the Down-select model as a validation case [27]. However, the utility of that experiment is limited due to three reasons: (1) Although Taylor did meticulously record all the parameters of his experiment, he neglected to include any mention of measurement uncertainty, (2) The axial power shape due to ohmic heating could not be accurately reconstructed, and (3) The maximum hydrogen temperature experienced was about 1500 K, which means the divergence of hydrogen properties at very high temperatures would

never come into play. On the other hand, although less controlled (after all, the main objective of the NRX-A6 test was not code validation), the NRX-A6 data does have traceable uncertainties, the axial power profile is well known, and of course, the hydrogen temperatures are more indicative of a real NTR environment.

In a separate report, the uncertainty in thermocouple measurements during the NRX-A6 tests was estimated by accounting for both instrumentation and data system uncertainties [47]. The $3\text{-}\sigma$ uncertainties are plotted for five different thermocouples as a function of temperature. The correlation between thermocouple part number and its placement in the core was not tracked down, but the errors were similar between each one, so an average was taken. This average maximum uncertainty was approximately ± 73 K at a temperature of 2606 K [48]. To this value, an additional uncertainty is added to account for the ambiguity that the thermocouple measurement truly represents the peak fuel temperature. This uncertainty, u_{Tmax} , is estimated as the difference between the peak fuel temperature and the average fuel temperature at the peak axial location:

$$u_{Tmax} = T_{peak} - \left(\frac{T_{peak} + T_{wall}}{2} \right) \quad (4.16)$$

where T_{peak} and T_{wall} are the peak and wall fuel temperatures observed in the simulation. Hence there is an assumption that the ΔT in the simulation and experiment are comparable enough for an uncertainty estimate. Using this approach u_{Tmax} comes out to 19 K. This is added in quadrature to the reported thermocouple uncertainty, to give an overall u_D of 75 K.

In order to simulate the NRX-A6, the inputs are borrowed from J. Walton, who also used NRX-A6 data to validate his code, “Program ELM,” in 1992. The inputs provided in Table 4.12 are used for the simulation, which are taken directly from Walton’s validation for Program ELM [4]:

Table 4.12 Simulation inputs for validation model

Input	Value
Power Deposited in Fuel Element	710 kW
Exit Pressure	593 psia
Inlet Temperature	123 K
Element flow rate	0.01878 kg/s

Walton also published a polynomial curve estimate for the axial power profile in the NRX-A6, which is used here as well [4]. The thermal conductivity for the NERVA fuel comes from a materials data compilation from Aerojet [38]. The uncertainty in the conductivity data is about 15% at high temperature.

The model geometry was taken as a 1/12th symmetry section of a fuel element. Of all the simulation parameters, the total power deposited is the most uncertain, since the exact radial power distribution in the core is not known; nor is the effort taken to isolate the element’s location in the core. This issue is circumvented by taking advantage of the exit gas temperature, which is well known (2642 K). A correction factor is applied to the total input power until the bulk exit temperature converges to the measured value. This correction factor turned out to be 1.05, producing an exit temperature of 2644 K.

4.5.2 Model Results

All of the same meshing and physics models that were discussed in Section 4.3 were used for the validation model. The wall y^+ was resolved down to an average of 0.47. A snapshot of the temperature solution at the hot end of the element is shown in Fig. 4.15.

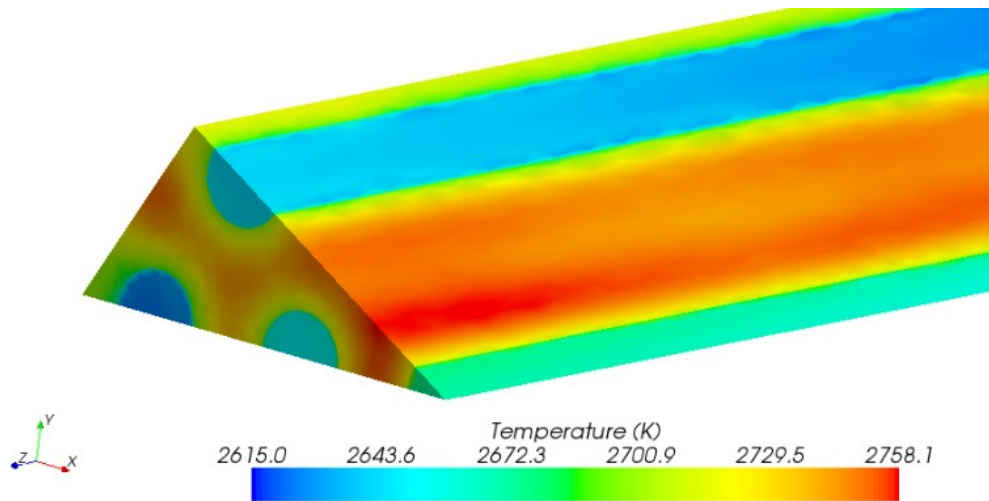


Fig. 4.15 Snapshot of validation model temperature distribution

The axial profile of the maximum fuel temperature calculated in Star-CCM+ is compared with the measured data in Fig. 4.16. The blue dashed lines indicate the estimated upper and lower uncertainty bounds for the measured values.

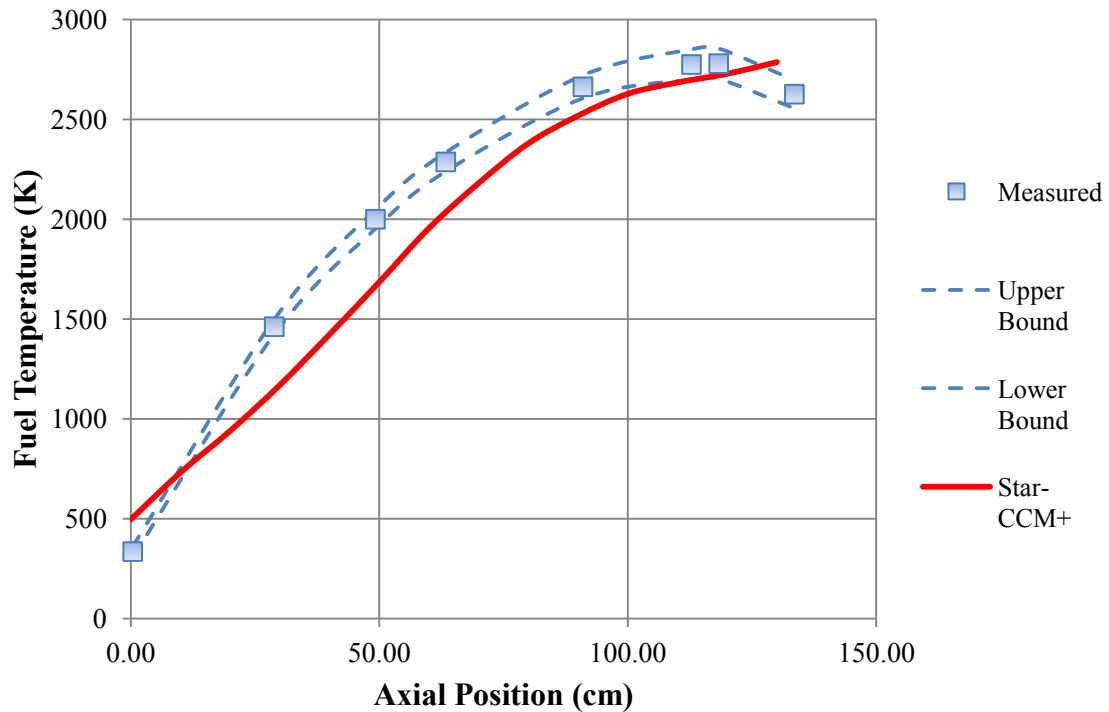


Fig. 4.16 Comparison of measured and simulated axial temperature profiles for the NRX-A6

The Star-CCM+ prediction for peak fuel temperature matches the measured test data reasonably well. The maximum measured temperature was 2779 K, which occurred at an axial location of 118 cm. The Star-CCM+ predicted peak fuel temperature at that location is 2718 K, a percent difference of 2.2%. Pressure drop was not expected to match particularly well between the simulation and experiment, since there were entrance and exit loss effects which are not accounted for in the model. Star-CCM+ predicts a pressure drop of 722.2 kPa versus a measured 827.4 kPa, a percent difference of 12.7%.

4.5.3 Estimate of Model-Form Error

At this point, the relationships discussed in Section 4.1.4 are used to estimate the model-form error, δ_{model} . The experimental-data uncertainty, u_D has already been estimated to be 75 K, but the numerical and input uncertainties need to be updated for the validation model. The relative numerical uncertainty, u_{num} , is taken to be 0.582%, exactly the same as that calculated in Section 4.3.2, since the same meshing techniques were used. The input uncertainty is based upon the low- ΔT model in Section 4.4, since the wall-to-peak ΔT is only 42 K. A 15% uncertainty is applied for the NRX fuel thermal conductivity input. The hydrogen uncertainties are kept the same because the same properties are used. Finally, the power relative uncertainty should be small because of the iterative manner in which it was determined, but due to the uncertainty in the axial profile it is kept, somewhat arbitrarily, at 3%. These assumptions result in a relative input uncertainty of 2.205%.

The resulting absolute uncertainties are summarized in Table 4.13.

Table 4.13 Uncertainties and errors in the validation model

u_{num} (K)	u_{input} (K)	u_D (K)	u_{val} (K)	S (K)	D (K)	E (K)
16	60	75	97	2718	2779	-61

It follows that the estimate of δ_{model} is -61 K (or in relative terms 2.2%), although the range of possible values is quite large. If a Gaussian distribution is assumed for the

combination of the numerical, input, and experimental uncertainties, then the 95% confidence range for δ_{model} extends from -255 to 133 K.

An important outcome of the validation exercise is insight into which factors need to be investigated in order to improve the modeling techniques. In this case, the magnitude of the validation comparison error ($|E|$) is less than or close to the magnitude of the validation uncertainty. This means that the modeling error is “within the noise level” of the combination of numerical, input, and experimental uncertainties [41]. It can be seen in Table 4.13 that the experimental uncertainty is the largest contributor to u_{val} . And, the largest contributor to u_{input} is the input power, which stems from knowledge of the experiment as well. Therefore, the conclusion can be made that the most important next step, by far, in improving confidence in NTR modeling techniques is a well-designed validation experiment.

Nonetheless, it has been shown that CFD modeling methods discussed throughout this chapter are reasonably accurate in predicting fuel temperatures, and that there is likely a modest, negative bias in the solution on the order of 2%.

4.6 Neutronics Uncertainty Quantification

The two main quantities which are calculated using MCNP are critical dimensions and volumetric energy deposition. In determining k_{eff} , it is recognized that all simulated designs are pre-conceptual at best, and that the final detail will alter the criticality of the model. Therefore, for k_{eff} , the statistical standard deviation reported by MCNP is deemed adequate, and no further investigation into k_{eff} uncertainty is performed.

Along with the mesh tallies, MCNP also outputs a table of relative uncertainties for each mesh cell. These uncertainties, like the standard deviation for k_{eff} , are mostly a function of the number of particle histories that are run. They therefore tend to be larger in lower-flux regions of the core, where the energy deposition accuracy is less critical. In order to produce an overall uncertainty that is suitable for producing error bars, the uncertainties from all cells are averaged. According to the MCNP manual, the tally results are considered reliable for uncertainties below 5% [15]. For each simulation, enough particles are run to ensure that the average uncertainty is considerably below that level.

4.7 Overall Uncertainty Assessment

The standard uncertainty in calculating fuel temperature, hydrogen temperature, and pressure drop for subsequent simulations will be estimated by assuming:

1. A u_{num} determined in Section 4.3.2.
2. A u_{input} defined by either the small- ΔT or large- ΔT sensitivity coefficient set determined in Section 4.4. The power relative uncertainty that goes into this calculation will come from the steps outlined in Section 4.6.
3. For the fuel temperature only, the relative δ_{model} estimate of 2.2% will be included.

These items will be summed in quadrature to produce approximate error bars for each simulation result. For illustrative purposes, typical relative standard error bars for a large wall-to-peak ΔT case are shown in Table 4.14.

Table 4.14 Typical total uncertainties for a large ΔT case

Parameter	u_{num}	u_{input}	δ_{model}	Total
Fuel Temperature	0.00582	0.02268	0.02195034	3.21%
Hydrogen Temperature	0.0011	0.02394	--	2.40%
Pressure Drop	0.04078	0.03485	--	5.36%

5. PARAMETRIC STUDY

The main objective of the parametric study is to provide guidance on the selection of the required coolant channel configuration for safe peak fuel temperatures. As discussed earlier, the design of the nuclear core of an NTR is a complicated process because of the many coupled relationships between different parameters. For example, the number and size of the coolant channels affects the overall core porosity, which affects the overall core critical size, which affects the power peaking factor, which affects the requirement for coolant channel flow rate, which affects the core pressure drop, which in turn depends on the channel size. When considering the many different physics relationships taking place in a core, the only realistic method for design must rely on some degree of iteration.

The overall process for the study is illustrated in Fig. 5.1.

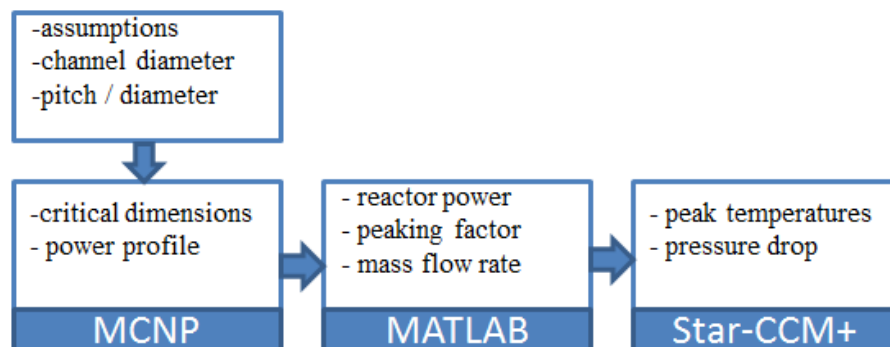


Fig. 5.1 Analysis process for parametric study

Several approximations are made during each step of the analysis process which will be discussed. The goal is to inform a decision about a fuel element design, which can then be scrutinized with a higher-fidelity set of analyses.

5.1 Definitions

The two independent variables which are varied to define the study are the coolant channel hydraulic diameter, d_{ch} , and the pitch-to-diameter ratio (p/d). These definitions are formulated based upon the triangular unit cell shown in Fig. 5.2:

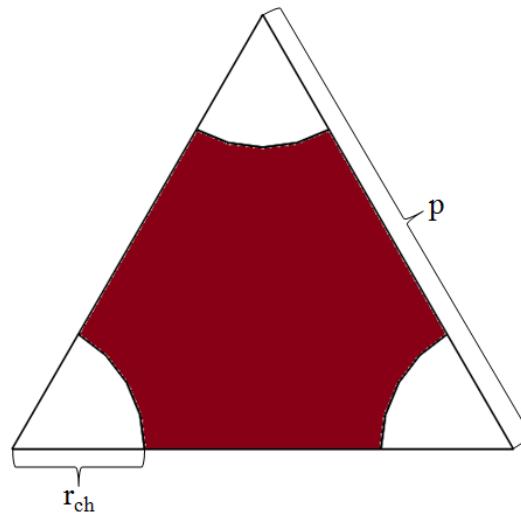


Fig. 5.2 Geometry of the triangular lattice unit cell

The p/d ratio can be used to calculate the core coolant void fraction, VF , using Eq. 5.1:

$$VF = \frac{\pi}{2\sqrt{3}(p/d)^2} \quad (5.1)$$

Alternatively, the same geometry information could be represented by specification of the coolant channel diameter and the coolant channel Surface Area-to-fuel Volume (SA/V) ratio. For the hexagonal fuel elements which have a constant shape in the axial direction, the SA/V is equivalent to the perimeter-to-area ratio. The VF and SA/V defined in terms of hexagonal geometry are shown in Eqs. 5.2 and 5.3.

$$VF = \frac{n_{ch/e} \left(\frac{\pi d_{ch}^2}{4} \right) L}{\frac{\sqrt{3}}{2} d_{F2F}^2 L} \quad (5.2)$$

$$SA/V = \frac{n_{ch/e} \pi d_{ch} L}{\left(\frac{\sqrt{3}}{2} d_{F2F}^2 - n_{ch/e} \left(\frac{\pi d_{ch}^2}{4} \right) \right) L} \quad (5.3)$$

where $n_{ch/e}$ is the number of coolant channels per element, d_{ch} is the hydraulic diameter of each channel, d_{F2F} is the hexagonal fuel element flat-to-flat dimension, and L is the fuel element length (which drops out).

Two competing effects take place as the channel diameter is increased. The SA/V increases, which reduces the peak fuel temperature. However, the VF also increases, which increases the critical volume and mass of the core. Therefore, the optimum channel size and p/d will be configured just tightly enough to ensure a safe maximum fuel temperature, but not too tight so as to drive up the mass of the core.

As a simple illustration on the effect of void fraction, Fig. 5.3 shows the critical mass for a typical cermet NTR core. The critical masses were determined iteratively with MCNP5, using homogenized geometry for the core and assuming a fixed combined core-and-reflector L/D of 1.0 (the core L/D was allowed to vary). For this particular configuration, there is a mass penalty of 31% when the VF increases from 0.20 to 0.31.

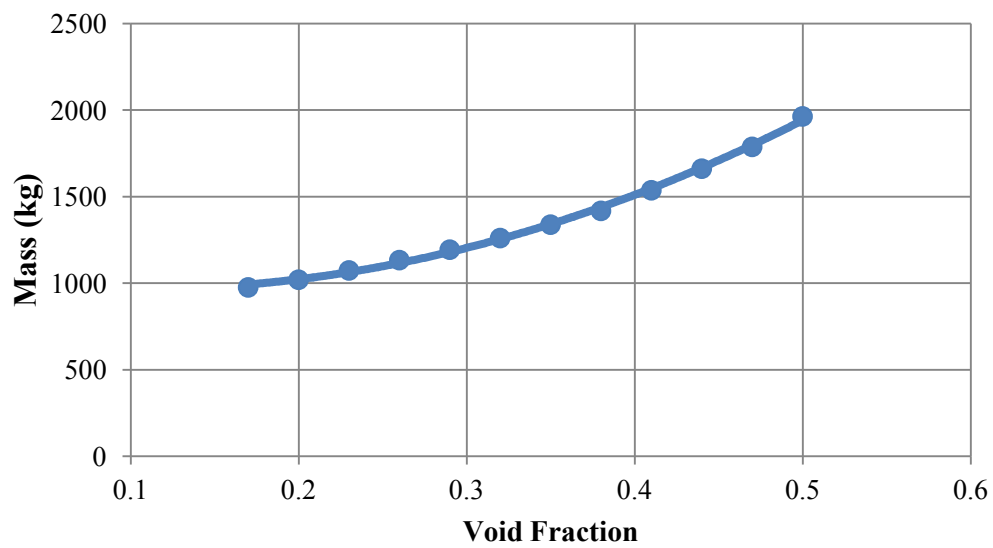


Fig. 5.3 Variation of core critical mass with void fraction

5.2 Review of Previous Parametric Studies

Three other parametric studies of a cermet NTRs have been found in literature, although each study incorporated slightly different assumptions. The main conclusions of each are summarized here.

The first study comes from the GE 710 program (volume I of the summary report), in which they looked at many of the basic design choices for the fuel [13]. They concluded that tubular fuel (more commonly referred to as prismatic fuel) is advantageous over pin or plate-type fuel for two reasons: (1) It results in a substantially lower temperature gradient for the same power density and hydraulic diameter; and (2) It has superior dimensional stability (i.e. does not propagate temperature gradients resulting from manufacturing imperfections or dynamic forces) as compared to the other types. The 710 program also studied the effects of different radial reflector thicknesses and materials, and their impact on core weight and peaking factor. They found that Be and BeO are both competitive reflector materials, but that Be results in the lightest engine. Their conclusions on peaking factor management will be discussed further in Section 5.4.5.

The second study, which comes from the ANL program, evaluated the effect of core L/D, porosity, and reflector thickness for both ^{233}U and ^{235}U based cores [12]. They assumed that the core would be flow orificed so as to produce a uniform outlet temperature and a maximum permissible fuel temperature of 2900 K. Several conclusions resulted from that study:

1. A ^{233}U core saves a very significant amount of weight compared to ^{235}U – the savings is greater than 30% for a 25 klb-thrust engine.
2. Increasing the radial reflector thickness from four to eight inches produces only a marginal impact on overall engine weight, although it does produce a significant radial power spike at the edge.
3. Core L/D does not have a strong influence on weight for low-thrust engines, although lower-L/D cores are generally lighter.
4. Chamber temperature can be safely increased while conserving weight by a combination of decreasing channel diameter and increasing chamber pressure.
5. The radial peaking factor has a surprisingly small influence on the weight, chamber pressure, and channel diameter.
6. The coolant channel surface roughness has a very significant effect on core performance. Although heat transfer is enhanced with roughness, engine weight was found to asymptotically decrease with decreasing roughness.

Much more recently, Webb, Taitano, and Gross evaluated the performance of an XNR-2000-derived design for carrying coolant channel size and distribution. They produced curves comparing the peak fuel temperature for a given coolant surface area-to fuel volume (SA/V) ratio. From their simulations, they estimated that 91 coolant channels of diameter 0.1778 cm would be required in a 3.51 cm flat-to-flat fuel element to keep the peak fuel temperature below 3000 K [3].

The general channel configuration used by Webb et al. is based on the configuration used by the XNR2000, which is based on the assumptions used by the ANL designs. Although the ANL report does include some results from its parametric study that led to their channel size selection, the precise methods they used or uncertainty in their calculations has not been documented. This is part of the justification for re-visiting some of the basic analysis for deciding channel configuration.

5.3 Design Space and Assumptions

This section will first describe the assumptions taken in conducting the study, and then discuss the justification for the range of channel configurations analyzed. In addition, the core sizes, power, and flow rates resulting from those assumptions are calculated.

5.3.1 Assumptions

Several assumptions are needed to make the parametric study tractable. First, there is an inherent assumption that for small-sized engines on the order of 10 klbf-thrust, the core dimensions will be criticality-limited, not power density-limited. For larger engine designs, an allowable power density may be specified, which then can be used to specify a target core volume. For the small engine, the smallest-possible core volume is first calculated, then the required total power is applied to it, making the power density a completely dependent variable.

Each of the remaining assumptions for the study are listed below.

1. The axial reflector thickness will be held constant at 20.0 cm (of beryllium) with the same void fraction as the core. The ANL-10k had a thickness of 10.16 cm,

and the XNR-2000 had a thickness of 20.32 cm. The GE-710 designs did not use an axial reflector. A thickness of 20 cm is chosen to maximize the effect of the axial reflector.

2. The radial reflector thickness will be held constant at 18.0 cm of beryllium-oxide, which is an intermediate value between historical designs. The ANL-10k engine had a 10.16 thick radial reflector; though they suggested the optimum thickness for low-power engines was in between 10 and 20 cm. The GE-710 program assumed a 19.05-cm radial reflector thickness for all power levels, and the XNR-2000 uses an 18.03-c m reflector thickness.
3. The core L/D will be fixed at 1.00. The ANL-10k and XNR2000 both have an L/D's of 1.00, while the GE 710 varied from 0.77 for the 200 klb-thrust engine to 1.04 for the 30 klb-engine. The ANL 100 klb-thrust engine has the highest historical L/D of 1.32. Since core mass is a weak function of L/D, setting L/D at 1.00 will keep the study comparable to historical designs.
4. The volumetric composition of the fuel will be 60 % UO_2 (93.15% enriched in ^{235}U), 33.91 % W, and 6.09 % Gd_2O_3 . This is identical to the ANL composition. The GE-710 designs used 45% UO_2 / 55% W.
5. The exit chamber pressure will be held constant at 600 psia, an intermediate value between historical designs. The ANL-10k design (bleed cycle) has a 540-psia chamber pressure, the GE-710 designs (expander cycle) all have a 500 psia-chamber pressure, and the XNR-2000 (expander cycle) has a 766-psia chamber pressure. No particular cycle is assumed.

6. The nozzle area ratio will be 200. The ANL-10k has a ratio of 50, the GE 710 has an area ratio of 100, and the XNR 2000 uses an area ratio of 200. The RL10, a (real) workhorse hydrogen upper stage engine built by Pratt and Whitney, has an expansion ratio of 250. A thrust coefficient efficiency of 98% is assumed.
7. The coolant channel cladding thickness will be 0.01778 cm of tungsten, which is identical to the ANL-10k. The GE 710 designs used 0.02032 cm of a tantalum-tungsten alloy. The study by Webb used a 0.009 cm channel cladding thickness. The choice of 0.01778 cm is an intermediate value between these designs, closer to the higher-end.
8. No other core heterogeneities will be accounted for, including fuel element cladding or a pressure vessel. This assumption will tend to cause an under-prediction of critical dimensions, but it is understood that critical dimensions for a detailed reactor design will differ no matter what assumptions are made.
9. The target excess reactivity is β_{eff} assuming an approximate delayed neutron fraction of 0.0066. The corresponding target k_{eff} is approximately 1.015.

The method for dealing with the peaking factor also needs to be determined. Many methods may be used, including fuel enrichment zoning, mass flow rate zoning, channel-by-channel orificing, or nothing at all. Three sets of cases are run to account for these effects:

1. No compensation for power peaking. The mass flow rate is equal in each channel.

2. Element-by-element mass flow rate zoning. This is approximated by dividing the core into 10 radial flow zones.
3. Channel-by-channel mass flow rate orificing. This is approximated by calculating the average number channels along the radius for each design, and dividing the core into a corresponding number of radial flow zones.

5.3.2 Channel Configuration

A range of channel diameters and p/d's have been chosen which generally encompass the values seen in historical designs. These values are shown in Table 5.1. For reference, the ANL designs have a diameter of 0.17 cm, the GE-70 designs range from 0.12 to 0.16 cm, and the XNR2000 has 0.36 cm.

Table 5.1 Channel size and p/d for parametric study

Case #	channel diameter (cm)	p/d	VF	SA/V (cm ⁻¹)
1	0.12	1.5	0.403	13.44
2	0.12	1.8	0.280	9.33
3	0.12	2.1	0.206	6.85
4	0.18	1.5	0.403	8.96
5	0.18	1.8	0.280	6.22
6	0.18	2.1	0.206	4.57
7	0.24	1.5	0.403	6.72
8	0.24	1.8	0.280	4.67
9	0.24	2.1	0.206	3.43

The corresponding void fractions and SA/V's are also shown. Historical cermet designs range in void fraction from 0.181 to 0.344, and in SA/V from 5.91 to 14.7 cm⁻¹.

For illustrative purposes, Fig. 5.4 shows the design space when it is applied to the 1.082" flat-to-flat fuel element used for the ANL-10k engine. For a triangular lattice imprinted in a hexagon, there is a discrete set of numbers which fit the channels symmetrically: 7, 19, 37, 61, 91, 127, and so on. It can be seen that due to the excess fuel at the perimeter of the fuel element, particularly in cases 6 and 9, the 1.082" flat-to-flat is only appropriate for certain combinations of channel diameter and pitch.

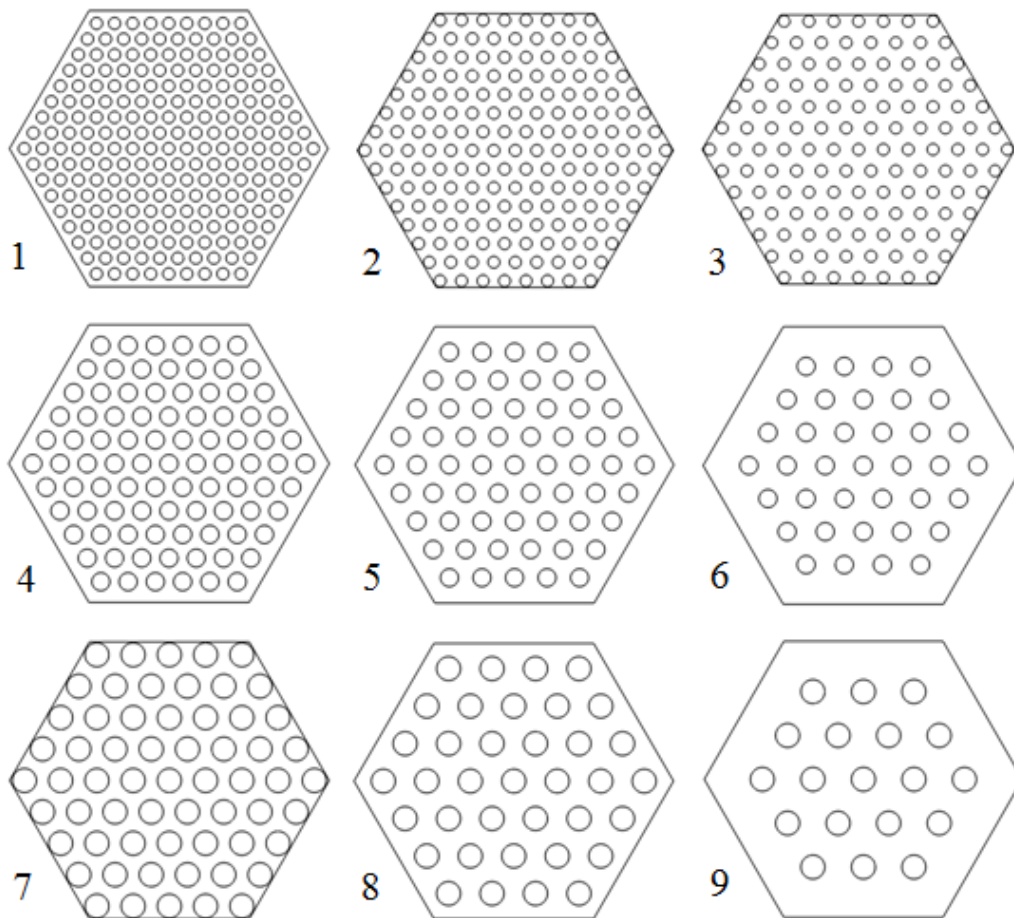


Fig. 5.4 Each of the nine cases applied to a 1.082" flat-to-flat fuel element

5.3.3 MCNP Model

Critical dimensions are determined iteratively in MCNP using a simplified model for the core, and a homogenized model for the radial reflector. The specific fuel elements are not modeled; instead the core is modeled as one continuous chunk of fuel with coolant channels. The cladding in each coolant channel is included, since that will have a significant effect on the net core composition. Fig. 5.5 shows various snapshots from the model.

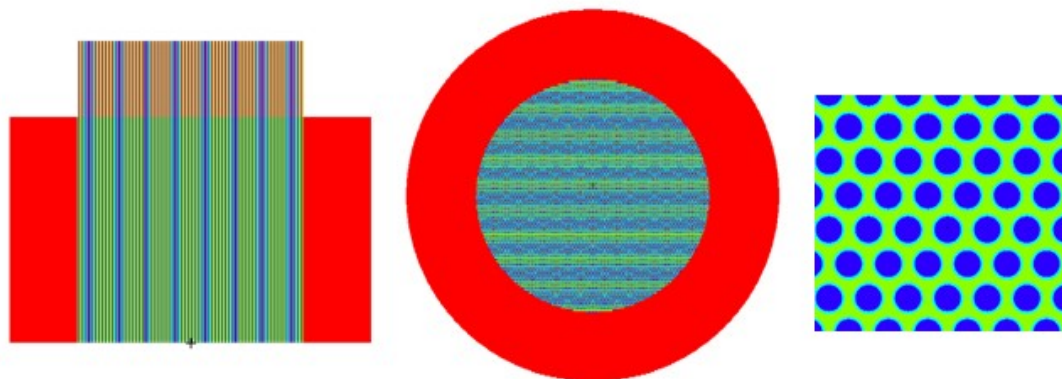


Fig. 5.5 Snapshots of a typical MCNP case in the study. Profile view (left); Cross-section view (center); Channel zoom-in (right)

In Fig. 5.5 the radial reflector is red and the axial reflector is orange. Table 5.2 shows the critical dimensions and corresponding total mass of the fuel in the core determined by MCNP iterations with each model.

Table 5.2 Critical dimensions for each channel configuration

Case #	Core diameter (cm)	Fuel mass (kg)	Clad volume fraction
1	78.41	3063	0.274
2	47.52	822	0.190
3	39.51	521	0.140
4	58.23	1254	0.175
5	42.73	598	0.122
6	37.2	435	0.089
7	53.21	957	0.128
8	41.12	533	0.089
9	36.45	409	0.065

As expected, the lower void fractions generally produce smaller cores, which require less fuel mass. However, one additional effect became apparent from the critical size results. Because the coolant channel cladding thickness was held constant in each case, the overall volume fraction of the cladding in the core varied significantly, as shown in Table 5.2. As a result, designs with large numbers of channels, most notably case 1, are penalized in size because of a higher net composition of tungsten in the core. This is an unintentional effect of holding the cladding thickness constant. However, the details of calculating the required cladding thickness as a function of channel diameter are beyond the scope of this study.

To facilitate the calculation of peaking factor for a large number of cases, the core power profile was obtained by first using an FMESH4 tally with cylindrical geometry, and then fitting a polynomial to the results. The radial direction was divided into ten mesh cells for each core. An example of the radial zones is shown in Fig. 5.6. Note in

Fig. 5.6 that the horizontal stripes are a consequence of rendering in MCNP, and do not represent any physical construction.

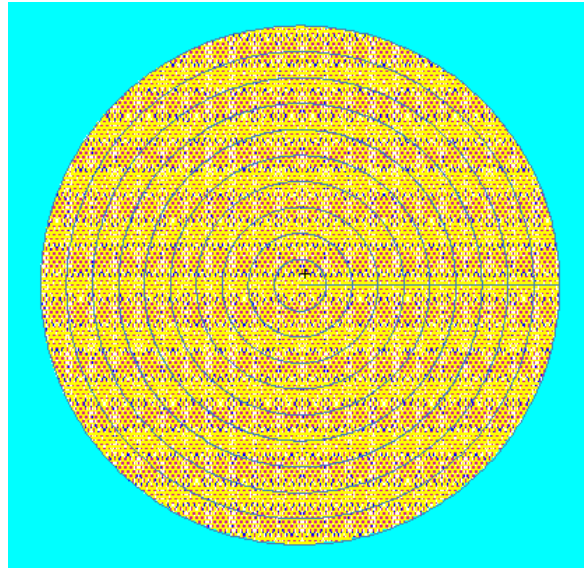


Fig. 5.6 Radial zones used for MCNP5 mesh tally

A similar technique was used to obtain the axial profile in each case. In order to normalize the radial results to estimate peaking factor, each polynomial was divided by an area-weighted average.

5.3.4 Rocket Performance Estimates

The requirements of thrust, I_{sp} , chamber pressure, and area ratio established in Section 5.3.1 are used to calculate the necessary chamber (core outlet) temperature, reactor power, and mass flow rate. A basic MATLAB code has been written to estimate these

parameters. This section describes the general method used in that code, which can be found in the Appendix.

First, the exit Mach number, M_e , is found by iteratively solving Eq. 5.4:

$$\varepsilon = \frac{1}{M_e} \left[\left(\frac{2}{\gamma + 1} \right) \left(1 + \frac{\gamma - 1}{2} M_e^2 \right) \right]^{\frac{\gamma + 1}{2(\gamma - 1)}} \quad (5.4)$$

where γ is the ratio of specific heats and ε is the area ratio. Next, the exit pressure, p_e , is calculated using the isentropic relation for compressible stagnation pressure:

$$\frac{p_e}{p_c} = \frac{1}{\left(1 + \frac{\gamma - 1}{2} M_e^2 \right)^{\gamma / \gamma - 1}} \quad (5.5)$$

The next step is to calculate the chamber temperature, T_c , using Eq. 5.6:

$$T_c = \frac{(\gamma - 1)v_e^2}{2\gamma R \left(1 - \left(\frac{p_e}{p_c} \right)^{\gamma - 1 / \gamma} \right)} \quad (5.6)$$

where v_e is the exhaust velocity and R is the specific gas constant. The exhaust velocity in a vacuum comes from the I_{sp} requirement:

$$v_e = I_{sp} g_0 - \frac{A_e p_t}{\dot{m}} \quad (5.7)$$

where the product $I_{sp} g_0$ is also known as the effective exhaust velocity, c . Next the chamber characteristic velocity c^* and nozzle thrust coefficient c_f are calculated:

$$c^* = \frac{\sqrt{\gamma RT_c}}{\gamma \sqrt{\left(\frac{2}{\gamma+1}\right)^{\frac{\gamma+1}{\gamma-1}}}} \quad (5.8)$$

$$c_f = \eta_{cf} \sqrt{\left(\frac{2\gamma^2}{\gamma-1}\right) \left(\frac{2}{\gamma+1}\right)^{\frac{\gamma+1}{\gamma-1}} \left(1 - \left(\frac{p_e}{p_c}\right)^{\frac{\gamma-1}{\gamma}}\right) + \varepsilon \frac{p_e}{p_c}} \quad (5.9)$$

where η_{cf} is the thrust coefficient efficiency. Equations 5.4 through 5.9 are solved iteratively until the chamber temperature and exhaust velocity converge to meet the requirements. Once the required chamber temperature is determined, the total power output required from the core is calculated using Eq. 5.3.10:

$$\dot{Q} = \dot{m} \left(\int_{T_1}^{T_c} c_p(T) dT + \Delta h_{vap} \right) \quad (5.10)$$

where \dot{Q} is the thermal power and Δh_{vap} is the enthalpy of vaporization. T_1 is the initial temperature of the hydrogen. It is assumed here that energy from the reactor is being used to vaporize the liquid-stored hydrogen, although this would occur outside of the core.

As a sanity check for the performance code, it was run for the ANL-10k and XNR2000 designs. These results are shown in Table 5.3.

Table 5.3 Comparison of calculated rocket performance with published calculations

	Input Parameters				Calculated Values		
	Thrust (lbf)	Isp (s)	Epsilon	Pc (psia)	Tc (K)	Power (MWth)	Flow rate (kg/s)
ANL-10k reported	10,530	821	50	540	2500	212	5.556
ANL-10k calculated	--	--	--	--	2457	219	5.936
XNR2000 reported	25000	900	200	766	2669	510	12.610
XNR2000 calculated	--	--	--	--	2626	512	12.856

It can be seen that the chamber temperature calculations match to within 2%; power matches to within 3%; and flow rate matches to within 7%. The most sensitive parameter in these calculations is the specific heat ratio γ , since it is a very strong function of temperature for hydrogen. The results are highly variable depending on which temperature at which γ is evaluated. An in-depth analysis of the nozzle flow is beyond the scope for this study, however, so γ will be evaluated at an average temperature between the chamber and nozzle exit; this is seen to match the published results reasonably well.

There is also some uncertainty associated with the power calculation. The code matches the published total reactor power very closely when the specific heat is integrated from the hydrogen core inlet temperature to the chamber temperature (as in Eq. 5.10). However, the total thermal power the reactor generates is also being used to heat the propellant from its cryogenic state, not just the inlet state; although the first 200 degrees K or so of this heating occurs outside of the core. For this reason, the integral in

Eq. 5.10 is begun at the storage temperature of the hydrogen, which will add 5 to 10 % to the total power.

Given these assumptions, the estimated chamber temperature, reactor power, and propellant flow rate for a 10 klb-thrust core is listed in Table 5.4.

Table 5.4 Performance requirements for the 10 klb-thrust core

Thrust (klbf)	Tc (K)	Power (MWth)	Flow rate (kg/s)
10	2630	222	5.14

5.4 Results

5.4.1 Peaking Factor and Flow Rate Zones

Fig. 5.7 shows the radial power profiles for each of the nine case. Each curve has been determined after fitting a 5th-order polynomial to the FMESH results, and normalizing with respect to the average radial power density. A total of four million particles were run in each case, which produced an average tally relative uncertainty of 0.33%.

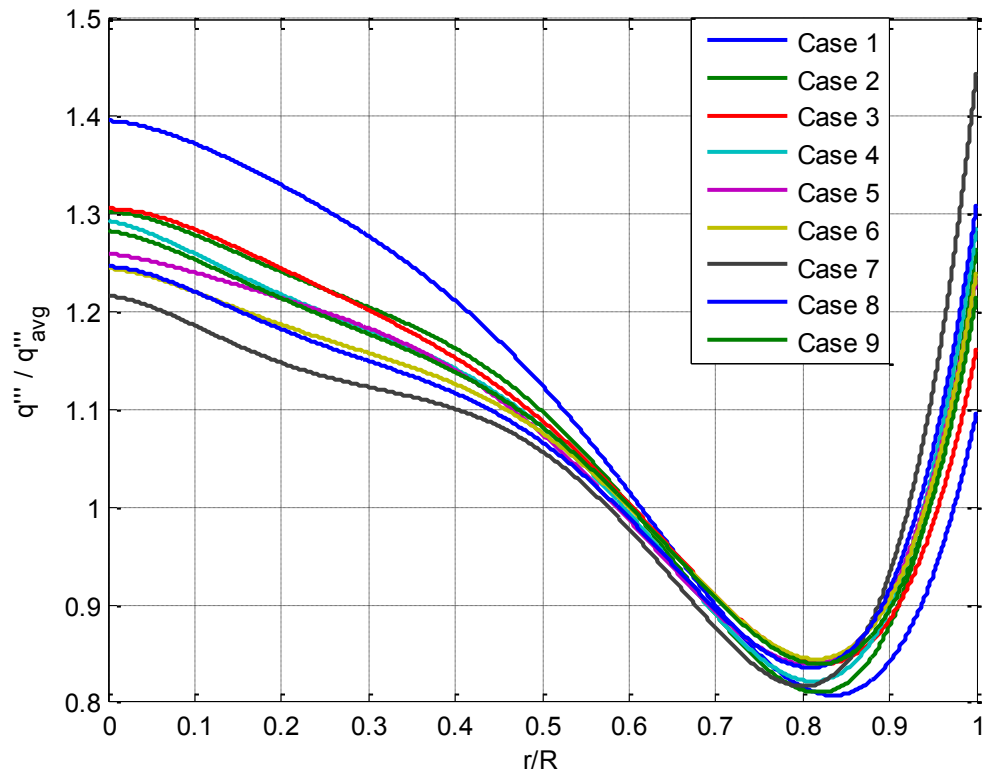


Fig. 5.7 Radial power profile normalized to average power

All of the cases have a center peaking factor between 1.20 and 1.30, except for case 1. The main cause for the variance in radial profile is the varying radial reflector worth as the size of the core changes. For case 1, which is substantially larger than the others, the edge peak due to the reflector is relatively smaller, which drives up the center peaking factor. It is suspected that the edge peak due to the radial reflector is slightly amplified due to the polynomial fit. However, the radial reflector on balance reduces the peaking factor a great deal. From 1D diffusion theory, the radial peaking factor of a bare

cylindrical core is about 2.32, which is much greater than the peaking factor for all cases. For two of the cases, 7 and 8, the radial edge peaking factor is actually larger than the center peak. However, due to the uncertainty in the edge peak, the center element is kept at the basis for analysis in all cases.

Fig. 5.8 shows the axial power profile for each case, again normalized to the average power. The shape for all cases is very similar, which indicates that the axial reflector thickness of 20.0 cm is relatively large and near the maximum possible axial reflector worth.

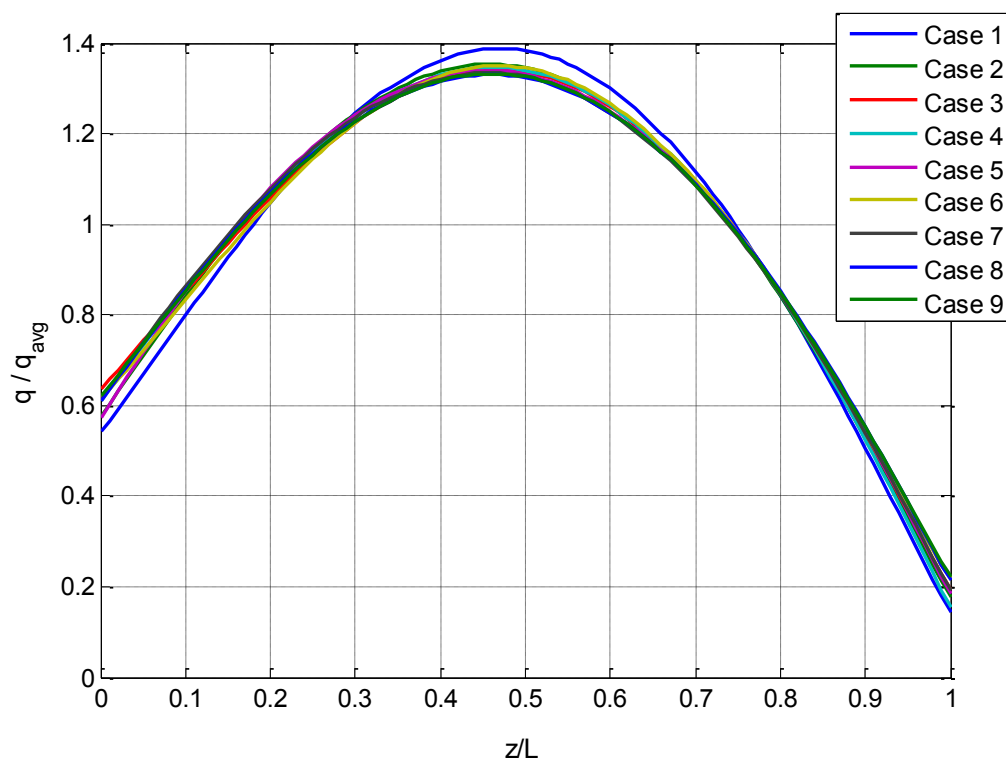


Fig. 5.8 Axial power profile normalized to average power

The flow rate distribution was determined by dividing the core into the specified number of radial zones, and applying a flow rate such that the same ratio of mass flow rate to total power is conserved in each zone. These calculations are performed in the MATLAB script `power.m`, which is included in the Appendix. Fig. 5.9 shows the mass flow rate per channel for each case when using the ten-zone (element-by-element) flow zoning method.

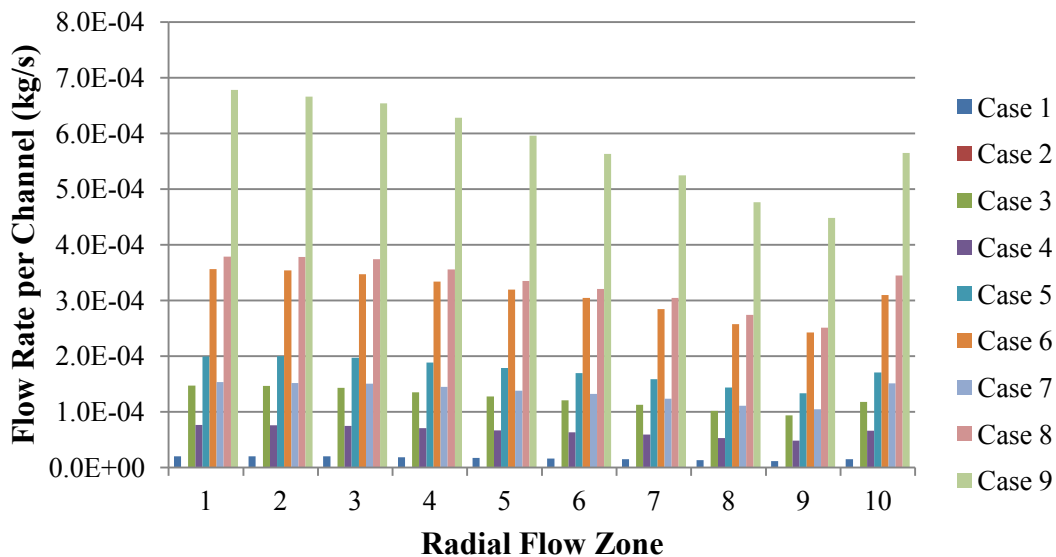


Fig. 5.9 Radial zone flow rate distribution for the ten-zone set of cases

5.4.2 Peak Fuel Temperatures

A total of 27 cases were run (nine configurations with three flow zoning schemes each), and the data can be interpreted in different ways. Fig. 5.10 shows a typical mesh and Fig. 5.11 shows a typical temperature distribution from the study.

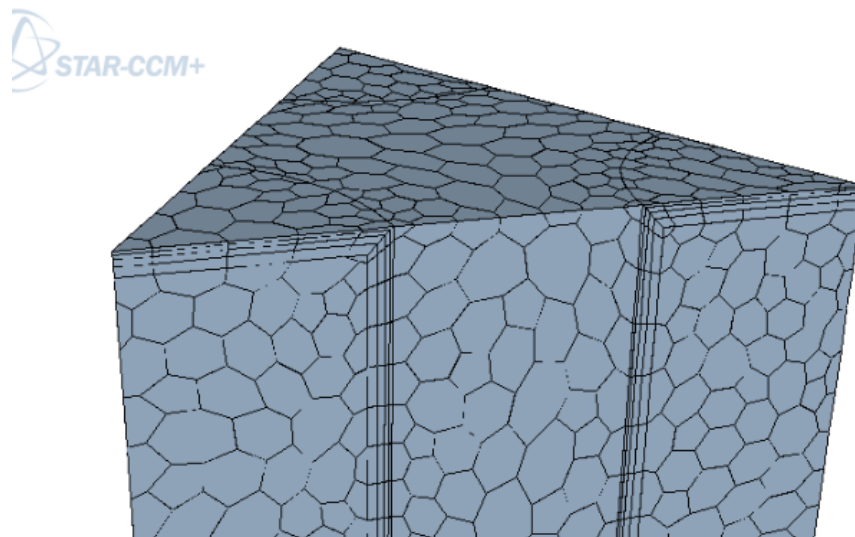


Fig. 5.10 Typical mesh snapshot from the parametric study

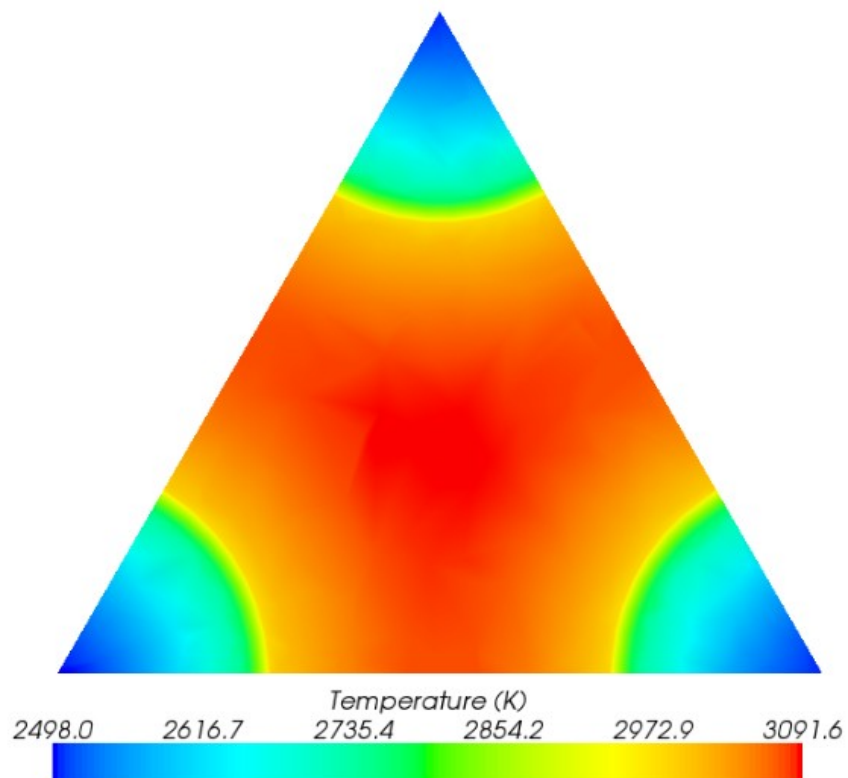


Fig. 5.11 Typical temperature distribution in a subchannel cross section

The peak fuel temperature is first observed as a function of p/d for different channel diameters. Figs 5.12 through 5.14 show the peak temperatures for the one-zone, element-by-element, and channel-by-channel zone data sets, respectively.

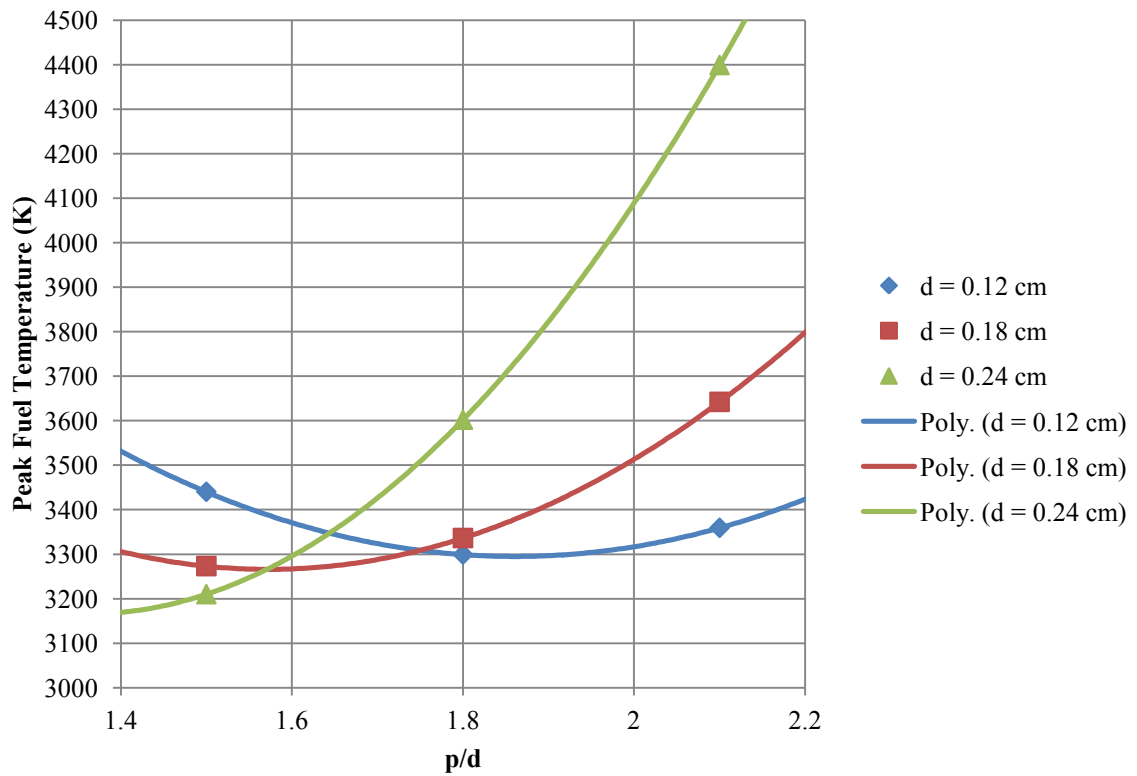


Fig. 5.12 Peak fuel temperatures for one mass flow rate zone

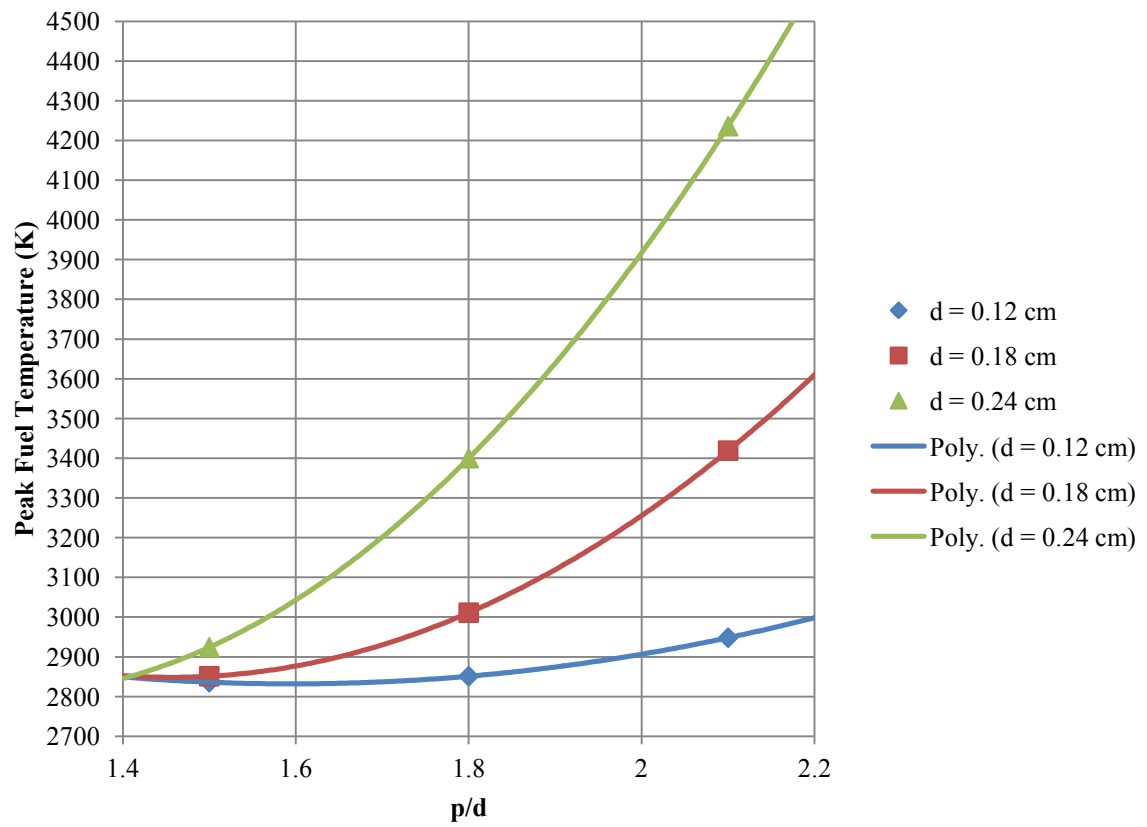


Fig. 5.13 Peak fuel temperatures for element-by-element flow zoning

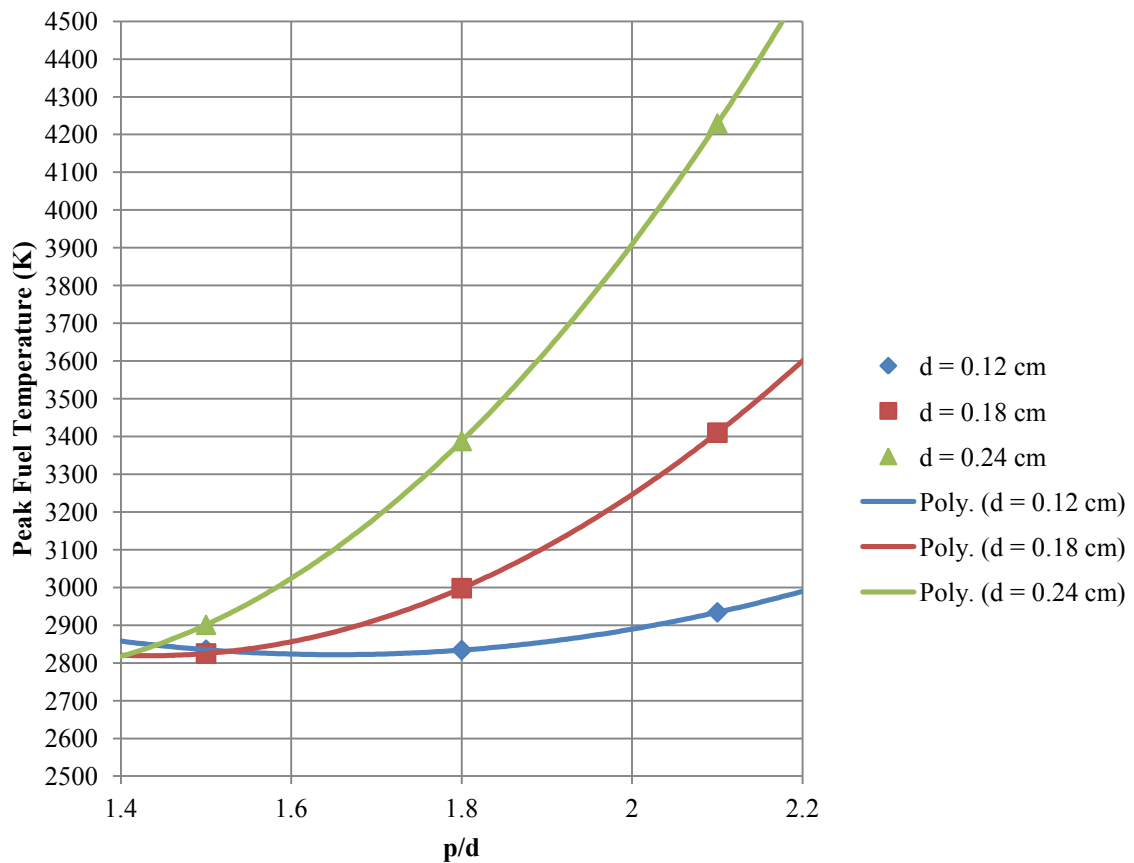


Fig. 5.14 Peak fuel temperatures for channel-by-channel flow zoning

Because of the great variety of peaking factors and flow rates, there are no clear trends in the results for the one-flow zone case (Fig. 5.12), except for one: Not a single channel configuration results in an acceptable peak temperature. This confirms the already-suspected notion that doing nothing to address power peaking in an NTR is not a plausible option.

The next immediate observation is that there is a very small difference between the results for the element-by-element data set and the channel-by-channel data set. The number of channel-by-channel zones ranges from 36 for case 8 to 218 for case 1. However, the radial power shape is slowly-changing enough such that the power gradient across any one fuel element is relatively small. These results indicate that subdividing a fuel element into flow zones only saves an average of 10 K off of the peak temperature. Given the extra effort and cost of implementing a channel-by-channel orificing scheme, with only a marginal improvement, these results would tend to make the element-by-element zoning option more attractive.

With 3000 K as a rough guideline for a permissible peak temperature, from Fig. 5.13 it appears that six of the nine channel configurations are competitive. Interestingly, as the curves for each channel diameter are extrapolated backwards, the peak temperature for all channel sizes converges to about 2850 K for a p/d of 1.4. The peak temperature for the 0.12-cm diameter case rises only slightly with p/d, while the change is more severe for 0.18 and 0.24 cm.

The curves in Figs. 5.13 and 5.14 can be used as a preliminary prediction of how a cermet NTR core with a particular channel size and p/d will perform. Interpolation between the case results can be used to target a specific temperature. However, with six possible configurations, other factors must be considered in choosing the best size.

As an alternative to using channel size and p/d as a criteria, the SA/V is plotted against peak fuel temperature in Fig. 5.15.

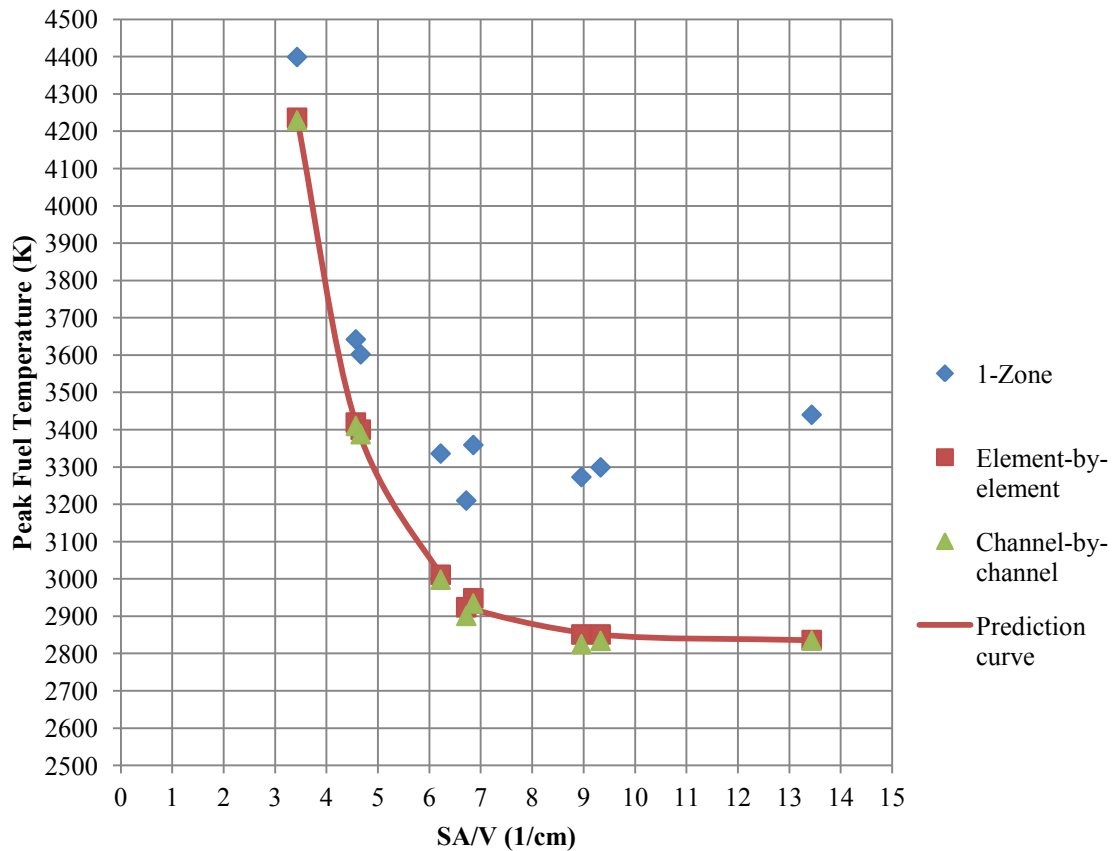


Fig. 5.15 Peak fuel temperature as a function of SA/V

Several observations come from this plot. First, the trend of decreasing peak fuel temperature with increasing SA/V is clearly shown as expected. However, the results are scattered for the 1-zone set. This scattering is due to other factors besides SA/V playing a role – most importantly a varying power density and peaking factor in each case. But for the element-by-element and channel-by-channel cases, the SA/V proves to be a useful discriminator for predicting peak fuel temperature. According to this plot, an

SA/V of approximately 6.2 cm^{-1} is required to keep the peak fuel temperature below 3000 K.

5.4.3 Pressure Drop

Pressure drop is another important consideration in fuel element design. Fig. 5.16 shows the pressure drop for each configuration when element-by-element flow zoning is used.

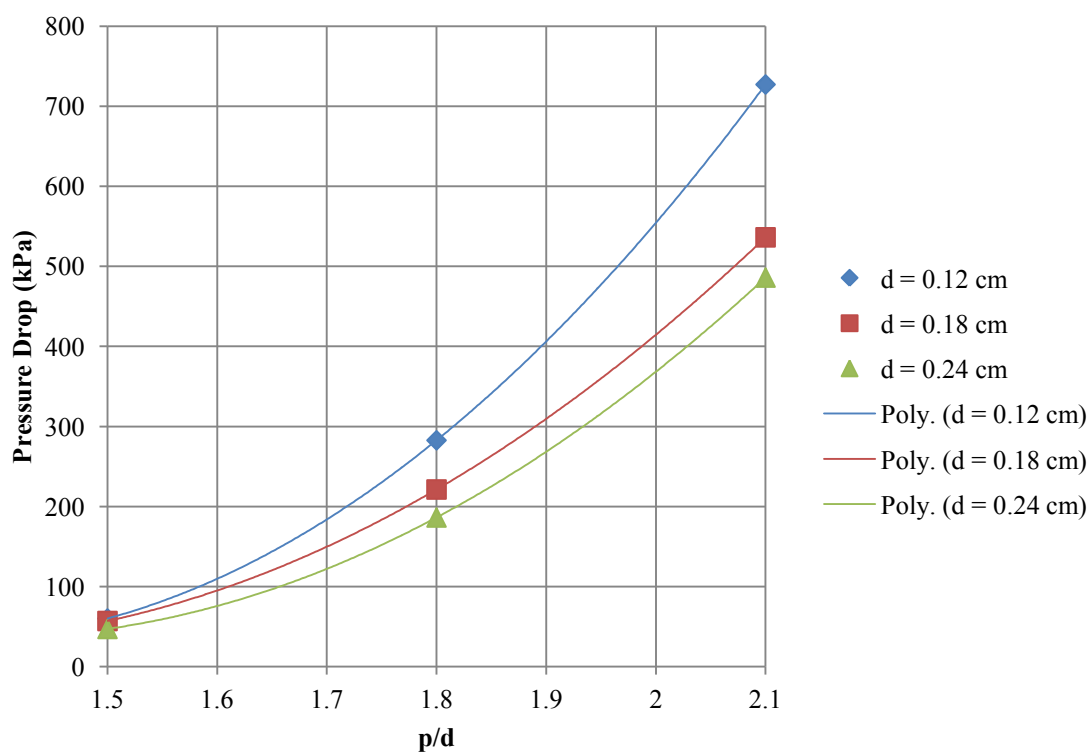


Fig. 5.16 Pressure drop for the element-by-element data set

The pressure drop does not increase with the inverse square of the channel diameter as one might expect, because the flow rate per channel is varied in each configuration (since smaller channels have a larger total number of channels per core). However, the p/d has a very severe effect on pressure drop, regardless of channel diameter. There is no clear restriction on pressure drop, since it is a part of a broader engine cycle analysis. For reference, the ANL-10k had a 414 kPa pressure drop, while the GE 710 designs all had a 2760 kPa pressure drop. Because there is a large tolerable range of pressure drop, it will not be used as a design discriminator at this conceptual-level parametric study.

5.4.4 Core Mass

Reducing core mass is one of the primary objectives of any NTR design effort. Fig. 5.17 shows the mass of the fuel in each case as a function of p/d and channel diameter. As discussed earlier, the constant coolant channel cladding thickness causes the $d = 0.12$ cm, $p/d = 1.5$ case to require a very large critical mass. This effect could potentially be reduced by allowing a thinner cladding for smaller channels, but is a real effect nonetheless.

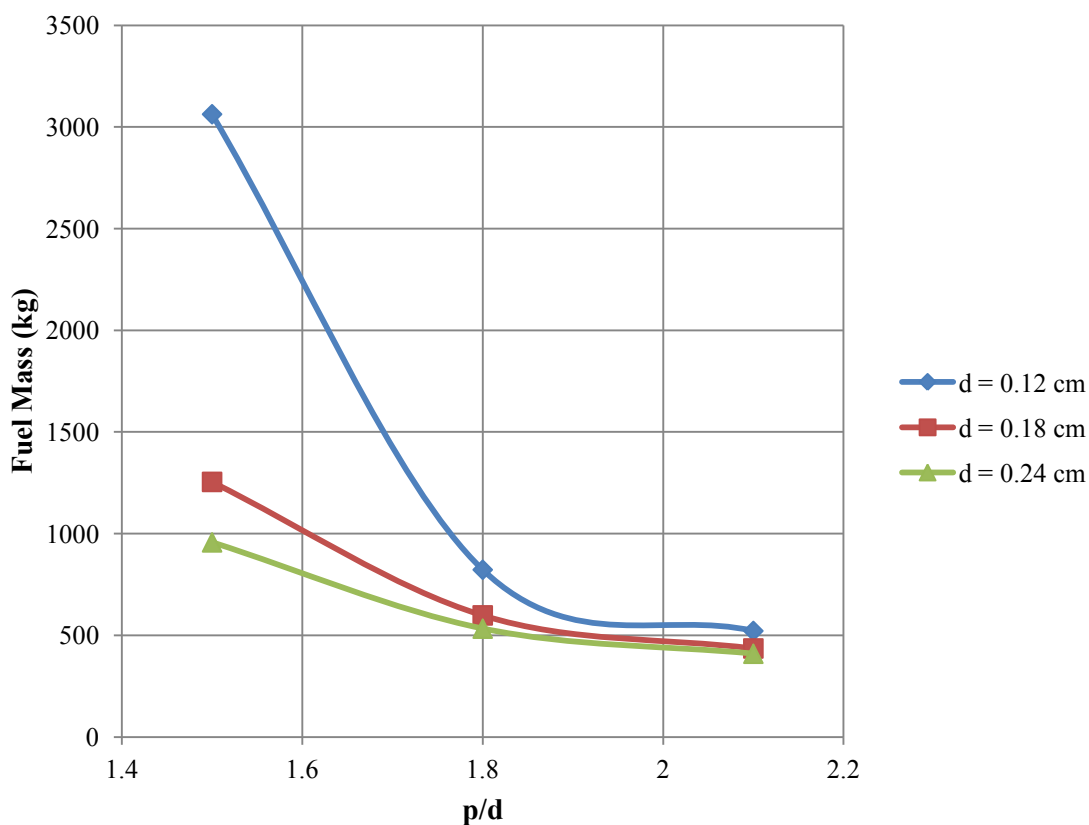


Fig. 5.17 Mass of fuel as a function of p/d

It can be seen that the required fuel mass converges as the p/d increases. There is also not a very large difference between the 0.18 cm and 0.24 cm cases for a p/d of 1.8 or larger. Therefore from a mass perspective, both the 0.18 cm and 0.24 cm channel diameters are competitive options.

5.4.5 Effect of Enrichment Zoning

Rearranging the fissile content of the core, either by changing the enrichment or fuel loading, is the other major technique that can be used for managing radial power

peaking. This technique was used heavily by the NERVA program, which included 17 different enrichment zones for the Small Nuclear Rocket Engine [18].

The technique was investigated for cermet engines as part of the GE 710 program. For their 30 klbf-thrust design, it was found that introducing eight radial fuel loading zones could reduce the radial peaking factor from 1.167 to 1.116. This comes at a cost of increasing the overall reactor mass by 21% [24]. More recently, Schnitzler applied the technique to the NERVA Small Nuclear Rocket Engine design by ^{235}U enrichment rather than the fuel loading. He found that two enrichment zones does not offer a substantial improvement; three or four zones are beneficial perhaps with a combination of flow rate zoning; and by going up to an arbitrary number of groups (37 in the SNRE case), the peaking factor could be reduced drastically to 1.012 [49].

In order to assess the potential impact of enrichment zoning, one of the more competitive designs, case 5 ($p = 0.18$ cm, $p/d = 1.8$) was divided into ten radial enrichment zones. This division is illustrated in Fig. 5.18.

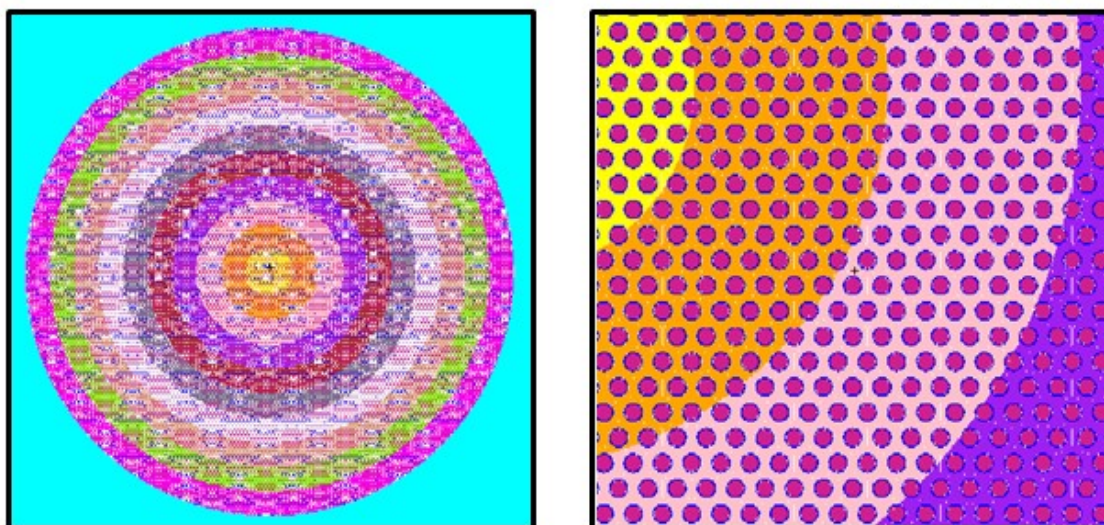


Fig. 5.18 Cross section view of radial enrichment zones (left); and zoom-in of zones (right)

The enrichment zones were first determined by establishing an overall range of enrichment based on past studies. It was decided to vary the ^{235}U enrichment rather than the fuel loading, because changing the overall UO_2 composition would require calculation of a new thermal conductivity for each ring. This could possibly introduce a peak temperature somewhere in the core away from a power peak. Two ranges of enrichment were investigated. For the first one, the enrichment range was based on the fuel loading zones calculated for the GE-710 study (0.495 to 0.600 v/o UO_2), but applied to the enrichment instead. This produces a permissible enrichment range of approximately 77% to 93.15%. This choice is arbitrary, and there are infinitely many enrichment combinations that are possible. However, the goal of this study is to roughly

gauge the impact that the enrichment zoning can have, and scaling down to 77% is in line with the range seen in historical designs.

Once the original radial power curve from case 5 was divided into ten equal-thickness radial zones, the enrichment in each zone was calculated by weighting it with the inverse of its peaking factor. It was found that in order to make up for the loss in fissile material, the first enrichment scheme required increasing the core mass by 21.8% - but there was an almost negligible effect on the radial power profile.

In order to achieve an appreciable amount of radial flattening, a new enrichment pattern was tried by allowing the minimum enrichment to drop to 57%, which is the lowest value used by Schnitzler for zoning the SNRE [49]. The enrichment levels in each of the ten radial zones are shown in Fig. 5.19 for the 77% and 57%-minimum cases.

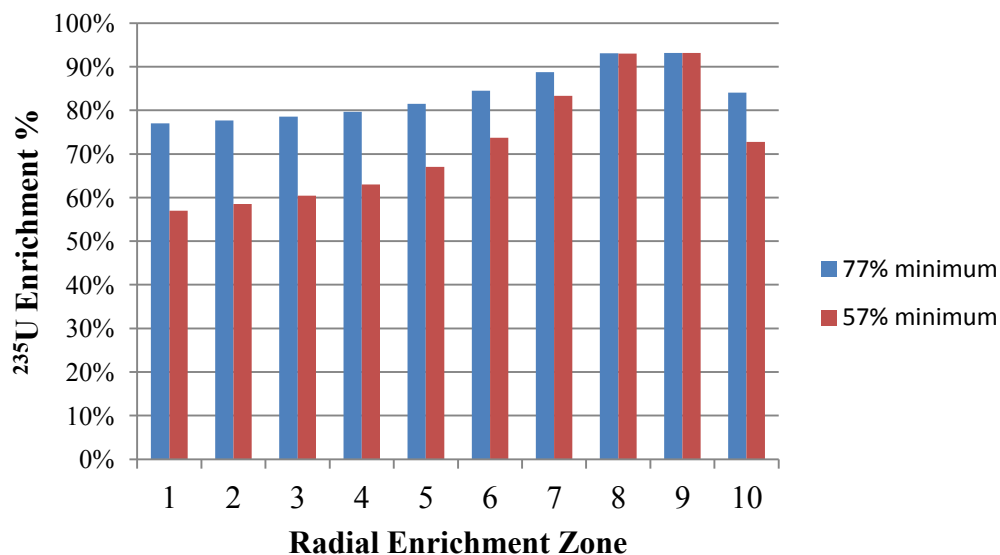


Fig. 5.19 ^{235}U enrichment levels in radial zones

Although dropping the minimum enrichment 57% did alter the radial profile, it did not have a very large impact on the overall peaking factor. Figure 5.20 shows the 57%-minimum enriched radial profile with the nominal (constant 93.15% enriched) case 5 profile.

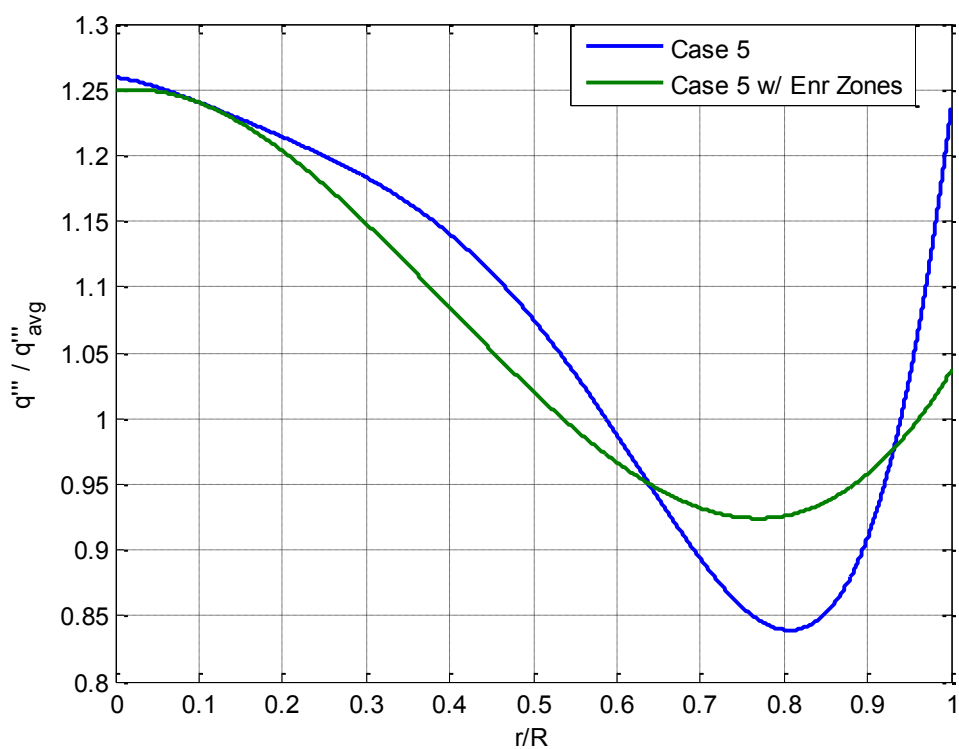


Fig. 5.20 Radial power profiles for flat-enrichment and zoned-enrichment cases

It can be seen that although the radial power shape is significantly flattened near the low-power zones and the reflector-edge peak, there is still only a small change in the

center peaking factor. In order to make up for the loss in reactivity, the 57%-minimum enrichment case required a fuel mass increase of 64%.

Table 5.5 shows the results of the Star-CCM+ simulation of Case 5 with no flow-zoning and with element-by-element flow zoning - each without enrichment-zoning and with enrichment-zoning.

Table 5.5 Effect of combining flow and enrichment zoning for Case 5

Flow Zones	Enrichment Zones	Peak Fuel Temp (K)	Peak Wall Temp (K)	Bulk Exit Temp (K)	Pressure Drop (kPa)
1	1	3336	3267	3186	183.5
1	10	3177	3129	2980	91.6
10	1	3011	2923	2792	221.3
10	10	2893	2845	2661	106.0

When no flow-zoning is done, the move to ten enrichment zones drops the peak fuel temperature by almost 6%, to 3177 K. When element-by-element flow zoning is combined with ten enrichment zones, the peak temperature drops by about 4% to 2893 K, which is a typically-acceptable peak temperature. It therefore appears that when the enrichment zones are combined with flow zones, an optimally-low peak temperature can be achieved. However, the actual cause for the reduction in peak temperature has little to do with the enrichment zoning directly – it is mostly due to the requisite increase in core size and corresponding decrease in average power density.

Increasing the core size (by as much as 64% by mass) in order to reduce the average power density would defeat the purpose producing the lightest-possible core to produce

10 klbf-thrust. Although enrichment zoning is certainly still a plausible option for larger engines, for a 10 klbf-thrust core it offers no advantages.

5.5 Application of Parametric Study to ANL-10k

To evaluate the robustness of the assumptions used in the parametric study, the results are checked against a more detailed analysis of the ANL-10k. This exercise also serves to re-assess the viability of the ANL-10k design using modern methods.

5.5.1 Model Setup

The ANL-10k has a unique fuel element design in that its upper half is made of Mo-UO₂, while the lower half is made of W-UO₂. This feature is included in order to substantially lower the mass of the core. Each fuel element has a flat-to-flat dimension of 2.748 cm, with 61 channels of diameter 0.170 cm, with a p/d of 2.03. An illustration of an ANL-10k fuel element model in SolidWorks is shown in Fig. 5.21. The green section is a beryllium oxide reflector, the yellow is Mo-60v/oUO₂, and the orange is W-60v/oUO₂.



Fig. 5.21 SolidWorks model of an ANL-10k fuel element

A detailed MCNP model of the ANL-10k reactor was built in order to obtain criticality and power generation information. Figure 5.22 shows a cross-sectional view of the reactor taken from the report on the left, and the MCNP model cross-section on the right. Fig. 5.23 shows a zoom-in of core detail, and Fig. 5.24 shows a profile view, where the leakage-control movable reflector is shown fully inserted and partially withdrawn. In all snapshots, blue is Mo-UO₂ fuel, dark green is W-UO₂ fuel, light yellow is tungsten-rhenium, light green is BeO, orange is Be, dark yellow is Inconel, purple is hydrogen, and red is stainless steel 316.

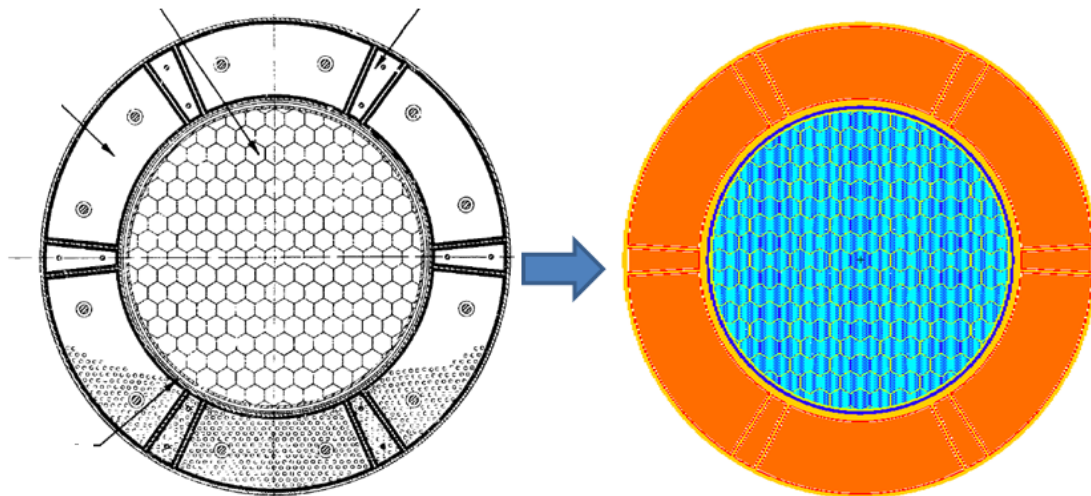


Fig. 5.22 Original reactor drawing (left) [8]; and MCNP model cross section (right)

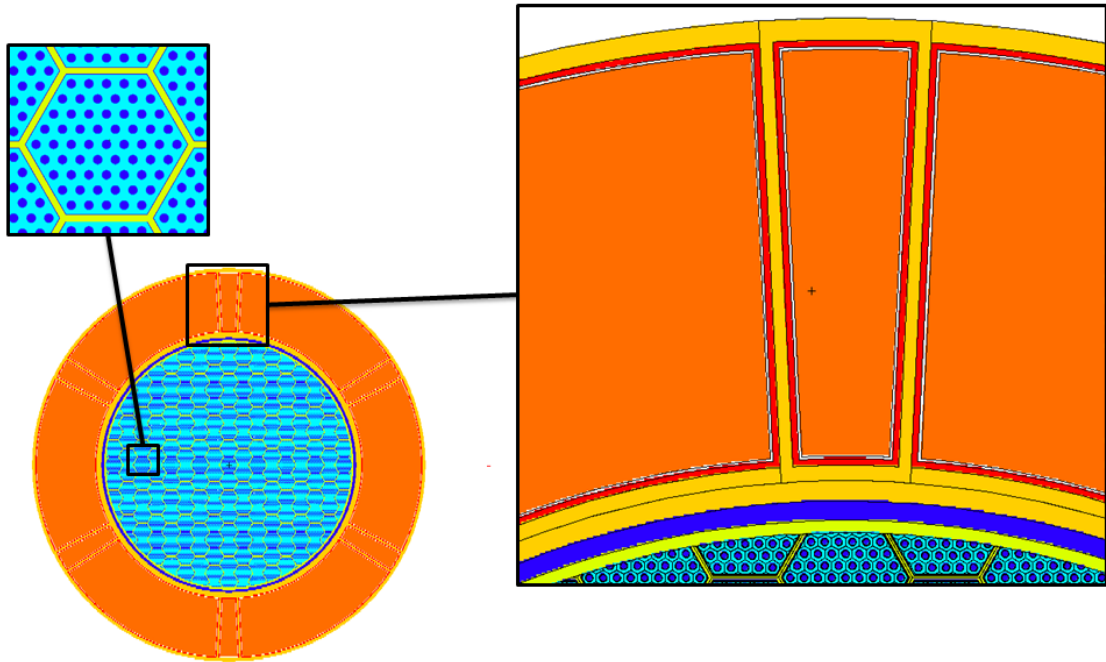


Fig. 5.23 Zoom-in of a fuel element (top left); and the reflector components (right)

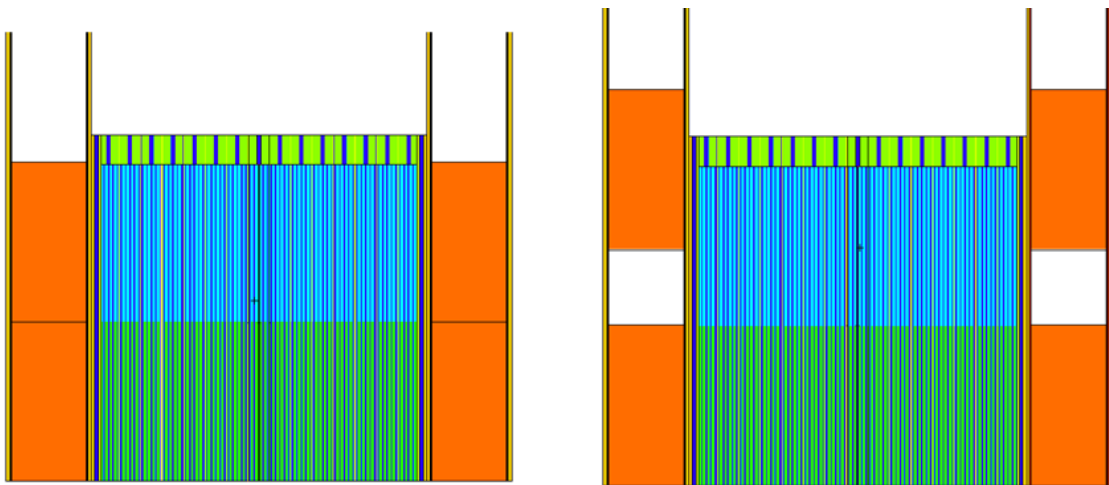


Fig. 5.24 Profile view of the MCNP ANL-10k model showing the movable radial reflector

The CFD model is based on a 1/12th symmetrical section of the center ANL-10k fuel element. This model includes the fuel element cladding and the core support grid, shown in Fig. 5.25. The red represents the fuel (Mo-UO₂ or W-UO₂), the brown is the fuel element cladding and the purple is the core support grid, both of which are W-25%Re.

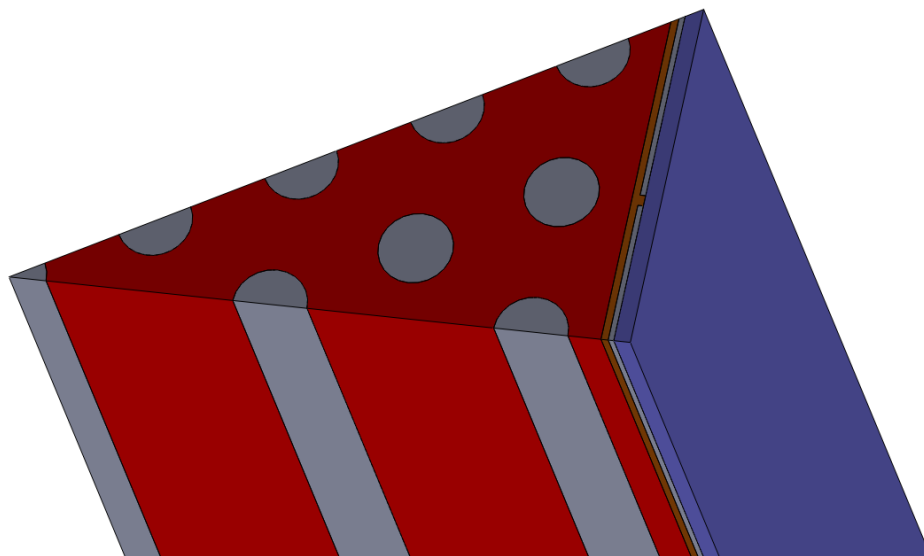


Fig. 5.25 SolidWorks snapshot of ANL-10k CFD model

5.5.2 MCNP Results

Figure 5.26 shows the power deposition shape resulting from the FMESH tally. This is a plot of the power deposition *per volume of fuel*, not overall core volume. This distinction is important for when the deposition is applied in the CFD model. The average fuel energy deposition rate is 5.03 GW/m³, while the overall average core power density (including the total volume of the core) is 3.43 GW/m³.

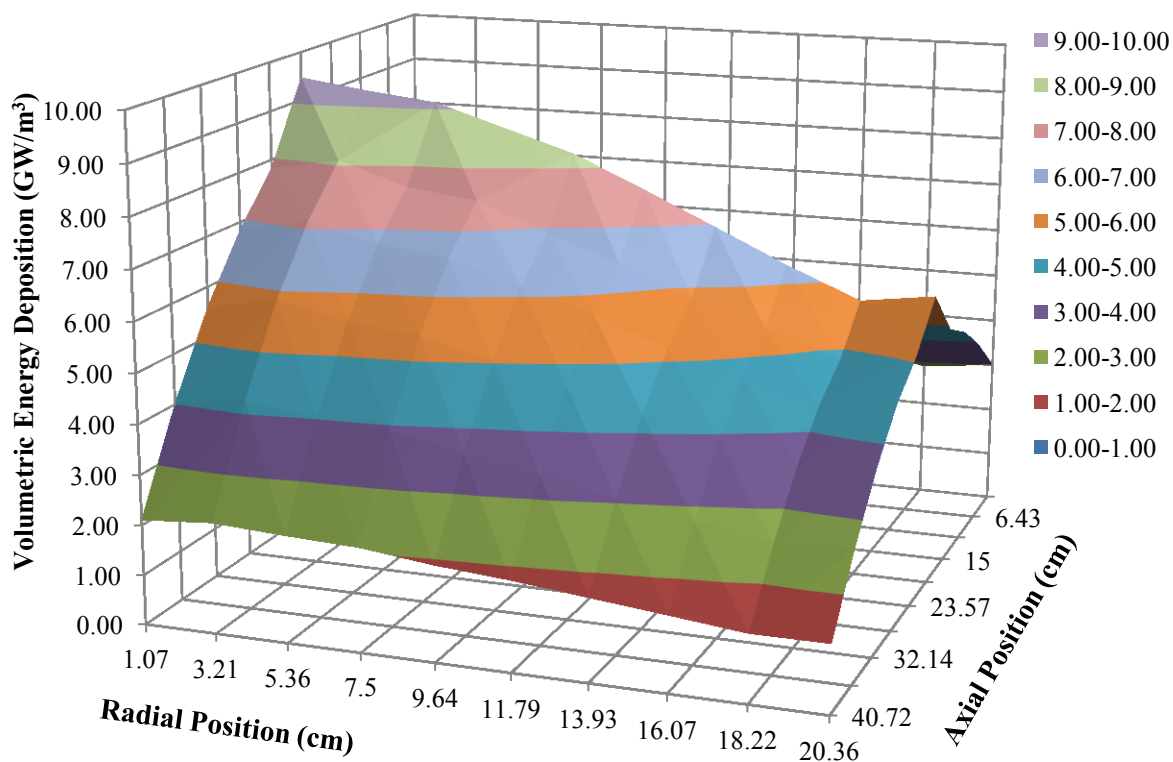


Fig. 5.26 R-Z profile of volumetric power deposition in the fuel

The overall radial peaking factor (with respect to average) is 1.373, and the axial peaking factor is 1.535. The radial peaking factor matches fairly closely to the value reported in original report, 1.35, with a difference of 1.7%. The originally reported axial peaking factor is 1.17, though it appears that this is normalized only to the Mo-UO₂ portion of the core. When the same normalization is applied to the MCNP results, the Mo-UO₂-half peaking factor is 1.213, a reasonable match.

It is visible in Fig. 5.26 that there is a cusp in the axial power shape occurring around the core midplane. This is physical, and is due to the abrupt change from Mo-UO₂ to W-

UO₂ fuel. The effect is caused by the overall larger volume fraction of M-UO₂, since the upper-half fuel elements do not use cladding for coolant channels or the fuel elements – which would otherwise take away fuel volume. Figure 5.27 shows the axial profile, normalized to average.

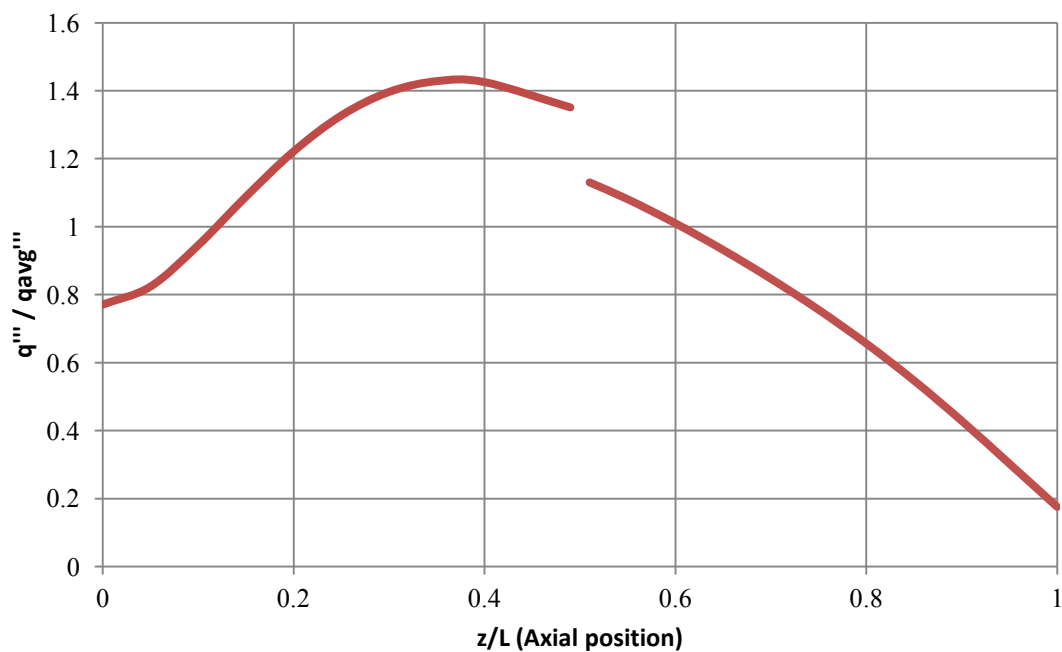


Fig. 5.27 Calculated axial power profile (normalized to average power) for the ANL-10k

Figure 5.27 represents the whole-core normalized power density; the fuel volumetric energy deposition rate is actually a continuous function. It can also be seen that the power profile begins to flare upwards as it gets close to the inlet end, which is a direct

effect of the axial reflector. This unique power shape generally produces an axial temperature profile with two local peaks, one in the Mo-UO₂ fuel and one in the W-UO₂ half.

5.5.3 CFD Results

Before the CFD results are reported, a prediction of the solution is made using the results of the parametric study. For a 0.170 cm-diameter coolant channel with a p/d of 2.03, Fig. 5.13 would predict a peak fuel temperature in the neighborhood of 3200 K, and Fig. 5.16 would predict a pressure drop of about 450 kPa.

The peak fuel and bulk hydrogen temperatures are plotted as a function of axial position in Fig. 5.28. The peak fuel temperature was 3098 K, with a bulk hydrogen exit temperature of 2756 K, and a pressure drop of 505 kPa. The results from the original ANL predictions, the parametric study predictions, and the detailed simulation are summarized in Table 5.6.

Table 5.6 Comparison of results for ANL-10k

Predictor	Peak Fuel Temp (K)	Pressure Drop (kPa)
ANL Report	3000	414
Parametric Study	3200	450
Detailed Simulation	3098	505

These results have two implications. First, they indicate that the parametric study, which was performed on a simplified reactor model, generally hold when compared to a

more detailed simulation. It is expected that the detailed simulation would yield a slightly lower peak temperature (in this case by about 3%), since the added detail in the core MCNP model, including the fuel element cladding and pressure vessel, would tend to increase the critical size and decrease the overall power density. The pressure drop prediction was not as consistent, with a difference of about 12% - however, this could be due to differences in the flow zoning distribution. Because the ANL-10k has only a four-inch radial reflector instead of the six-inch reflectors used in the parametric study, its radial peaking factor was a little bit higher, thereby requiring more mass flow per channel at the center.

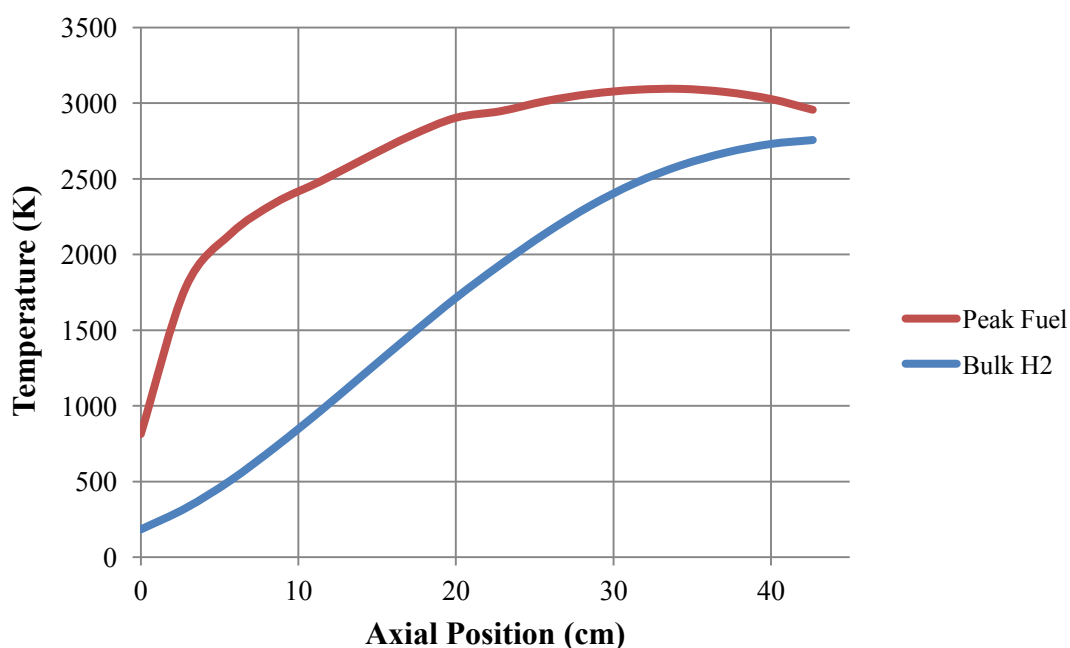


Fig. 5.28 Axial temperature profiles for the ANL-10k

The results have an even more important implication for the overall design of the ANL-10k. The design peak temperature of 3000 K left a small margin to the melting point of UO_2 to begin with. The simulation result of 3098 K, ± 99 K, is close to the original prediction, and within the range of uncertainty. However, because the range on uncertainty extends up to 3197 K (beyond the fuel melting point), the conclusion can be made that the ANL-10k is designed to run slightly too hot. The best remedy for this, according to Fig. 5.13, would be to reduce the p/d from 2.03 to about 1.9, and/or reduce the channel diameter from 0.17 cm to about 0.15 cm. These changes would probably incur a core mass penalty of about 10-15%.

A cross section of the temperature distribution near the peak fuel temperature is shown in Fig. 5.29. One interesting note on the ANL-10k design is that although the parametric study suggested that channel-by-channel flow zoning offers only a slight advantage over element-by-element zoning, Fig. 5.29 clearly suggests that the peak temperature could be further reduced by channel zoning, for at least the center element.

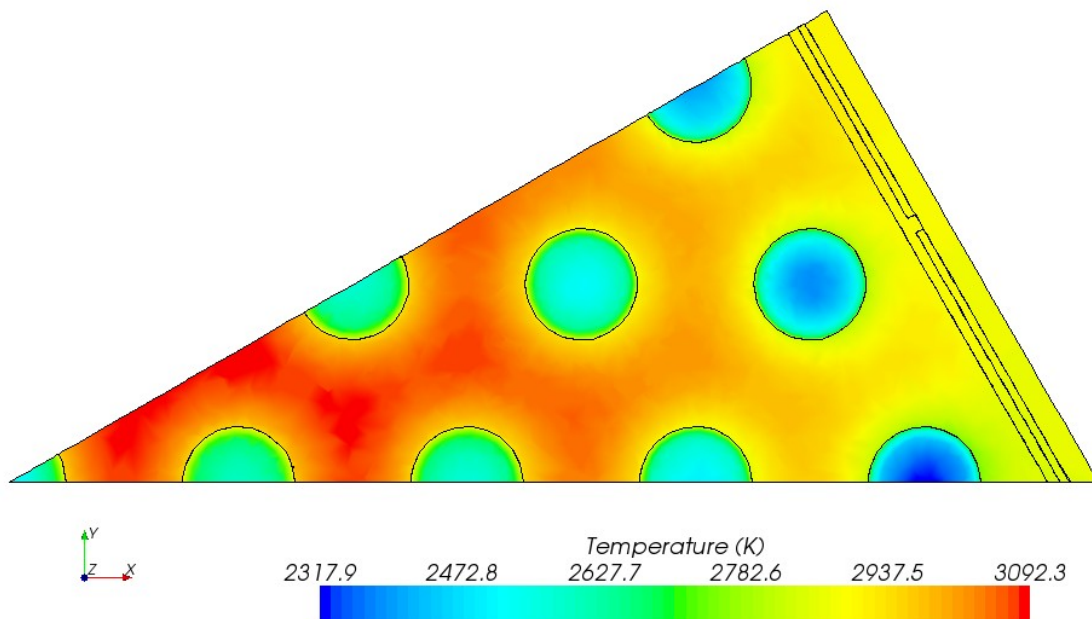


Fig. 5.29 Transverse temperature distribution in the ANL-10k fuel element

In the original ANL report, it was also assumed that the core support grid would be adequately cooled by the gap region, although no particular analysis was done. This region is resolved and outlined in the right side of Fig. 5.29. It can be seen that there are no significant temperature gradients at the fuel element edge, and that the core support grid does stay adequately cooled.

The final assessment resulting from this analysis is that the ANL-10k is *close* to being a feasible design, but runs with a peak fuel temperature with probably too small a margin. In order to make the design safer, slight adjustments to the channel configuration should be made, which can be guided by Fig. 5.13.

5.6 Channel Size Recommendation

The final conclusion from this study is a recommendation of the optimum channel configuration for a 10 klbf-thrust NTR core subject to the following constraints:

1. The core size is criticality-limited, which inherently makes it optimized for mass.
2. An element-by-element flow zoning scheme is used, and no enrichment zoning is done.

The maximum allowable fuel temperature is chosen using Eq. 5.11 as a guide:

$$T_{max} = \frac{T_{melt,UO_2} - \Delta T_{SM}}{F_{trans} F_{uncert}} \quad (5.11)$$

ΔT_{SM} is a safety margin included to account for the uncertainties in the estimates of the other ΔT 's. It is arbitrarily chosen to be 30 K here.

F_{trans} is meant to account for the overshoot that can occur during reactor startup.

During the NRX test series, reactor startup was controlled by a power-feedback controller until the chamber temperature reached about 1100 K, at which point control was transferred to a temperature-feedback loop [46]. During the NRX-A6 full power test EP-III A, there was an 82 K, or 3.8%, overshoot in chamber temperature during startup [46]. This coincided with an approximate power overshoot of 42 MW, or 4.1%. If it is assumed that operation of a W-UO₂ NTR is controlled in a similar manner, then it is reasonable to assume that there will be a 4% overshoot in core temperature (for an F_{trans}

of 1.04). Throughout the rest of the 62 minute run of EP-III A, no other significant, unplanned, power excursions were observed.

The melting temperature of UO_2 is listed as 3120 K, +/- 30 K, and it is conservatively taken as 3090 K [50]. The safety margin ΔT_{SM} immediately reduces T_{max} to 3060 K. When the ΔT for transients is accounted for, T_{max} comes down to 2942 K. Then, an additional ΔT is taken out by assuming the 3.2% uncertainty ($F_{uncert} = 1.032$) that was calculated in Section 4.14. This results in a T_{max} of 2851 K, which is rounded to 2850 K.

According to Fig. 5.13, the only channel configurations which can satisfy a peak fuel temperature of 2850 K are a 0.24 cm-diameter channel with a p/d of up to 1.4, 0.18 cm-diameter channel with a p/d of up to 1.5, and a 0.12 cm-diameter channel with a p/d of up to 1.8. Of these options, according to Fig. 5.17, the case with a channel diameter of 0.12 cm and a p/d of 1.8 produces the lightest core.

The three viable channel configuration options are summarized in Table 5.7.

Table 5.7 Viable channel configurations for not exceeding a peak temperature of 2850 K

Channel Diameter (cm)	p/d	Fuel mass (kg)	Pressure Drop (kPa)	SA/V (cm^{-1})
0.12	1.8	822	282.8	9.33
0.18	1.5	1254	57.0	8.96
0.24	1.4	1410	38.0	7.71

6. MULTI-ELEMENT FAILURE MODE ANALYSIS

6.1 Important Failure Modes

The purpose of this section is to serve as a basic demonstration of one of the next logical steps for cermet NTR modeling – to couple the thermal hydraulic simulations (already discussed in detail) with the ability to evaluate complex fuel failure modes. While Sections 4 and 5 discussed the techniques for predicting peak temperature, a major potential failure mode, the integrity of a fuel element can also be threatened by various induced stresses. The main stresses of concern in a cermet NTR can be attributed to three general sources [13]:

1. Coefficient of thermal expansion (CTE) mismatches. This can occur on multiple levels. At the microscopic level, the different CTEs of the matrix metal and the fuel can cause a warping of the fuel over time. On a larger scale, there can be a CTE mismatch between the fuel matrix and the coolant channel cladding; and the fuel matrix and the fuel element cladding. In either case, there is a risk for cladding failure and fission product release.
2. Large temperature gradients. Between the coolant channel wall and the fuel centerline, the fuel temperature can change by hundreds of degrees K within a fraction of a centimeter, producing thermal stresses due to the varying expansion. Large temperature gradients can also result from quick changes in the axial and radial power profiles. Typically the axial power changes slowly enough to avoid a problem, but the radial power shape, particularly near the

reflector peak, can cause large temperature changes across a single element. If extreme enough, either of these effects can cause cracking of the fuel, and a resulting structural failure or fission product release.

3. Large pressure differentials. Depending on the sealing mechanism between the inlet-end and outlet-end of the core, there may be a substantial pressure difference between the inside of a coolant channel and the exterior of the fuel element. This can induce a hoop stress in the channels which could threaten the bond of the cladding. However, from testing and basic analysis, for the most part pressure-induced stresses are less of a concern than temperature-induced stresses [13].

The other main failure mode not listed above is cracking due to the build-up of fission product gases inside the fuel matrix. In fact, this is often considered the most threatening failure mode. However, analysis of this phenomenon is not well suited for the macroscopic problems modeled in Star-CCM+.

6.2 Multi-Element Model

To demonstrate the ability to assess common failure modes in Star-CCM+, the 0.24 cm, $p/d=1.4$ coolant channel configuration was selected from the recommended designs in Table 5.6. The tighter pitch results in a critical diameter of 62.7 cm and average volumetric energy generation of 2.13 GW/m^3 . The thickness of the external fuel element cladding was chosen as 0.01778 cm, which is identical to the ANL-10k design. The flat-to-flat dimension was trimmed from 2.748 cm to 2.639 cm in order to more evenly

distribute cooling channels along adjacent fuel element edges. Figure 6.1 shows a snapshot of the model in SolidWorks, which covers 1/12th of the central fuel element along with 1/4th of an adjacent element in the next row.

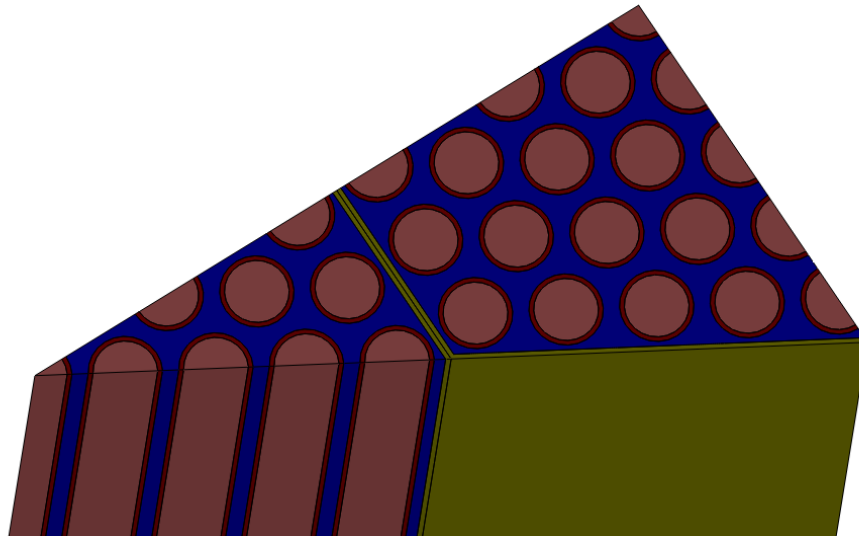


Fig. 6.1 Multi-element model for stress analysis

The blue represents the W-UO₂ fuel, the pink represents the cooling channels, the red represents the tungsten coolant channel cladding, and the gold represents the W-Re fuel element cladding. Element-by-element flow zoning is applied to the model such that the central element receives 2.022×10^{-4} kg/s per channel, and the second element receives 1.963×10^{-4} kg/s per channel.

This model is capable of simulating the stresses from each of the causes described in Section 6.1. By applying the solid stress model in Star-CCM+ and inputting data for the

coefficient of thermal expansion for each material, the thermally-induced stresses will be resolved. In addition, a net pressure force can be applied to the external cladding surfaces to simulated pressure-induced stresses.

6.3 Results

The channel configuration chosen for this simulation is an extrapolation from the parametric study, and as such a good check on its usefulness. Table 6.1 shows the performance results from the simulation. As discussed in Section 5.6, the target peak fuel temperature was 2850 K, which the actual model comes to within 1%.

Table 6.1 Results for failure mode test case

Peak Fuel Temp (K)	Peak Wall Temp (K)	Bulk Exit Temp (K)	Pressure Drop (kPa)
2827	2816	2715	25515

Figure 6.2 shows the equivalent solid stress distribution across a cross-section of the model near the maximum temperature. The equivalent solid stress, sometimes called the von Mises stress, is the summation of the principle stress components and represents the maximum stress that the material is experiencing. Figure 6.3 shows the equivalent solid stress across a cross-section near the peak temperature.

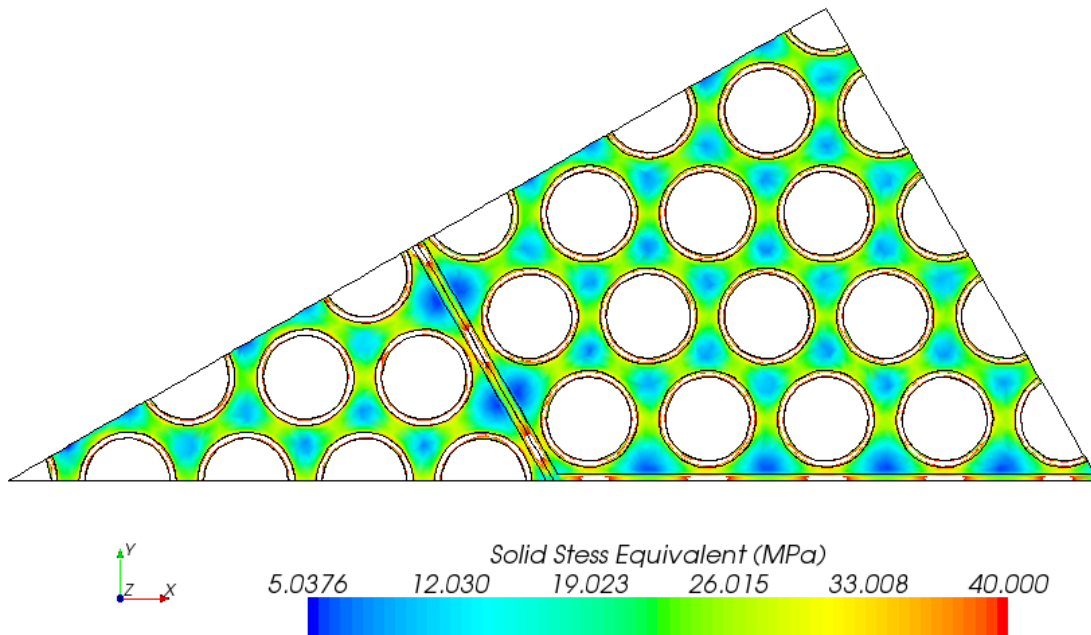


Fig. 6.2 Equivalent solid stress in the failure mode model

According to analysis during the GE-710 program, the W-60UO₂ fuel can be exposed to a compressive stress of up to 78,000 psi (538 MPa) safely, however the precise yield stress of the fuel is not known. There are also large uncertainties associated with the input properties for solid stress simulation. Accordingly, the results in Fig 6.2 are included only as a demonstration that Star-CCM+ can be a useful tool for resolving stress in a cermet fuel element; but reliable results would require more scrutiny. It is clear from the figure, however, that the stress levels in the cladding exceed the fuel

matrix stress. It is also interesting to note a pattern of high-stress regions connecting the shortest distances between each coolant channel edge.

Figure 6.3 shows the deformation in each component resulting from the stresses, when exaggerated by a factor 50.

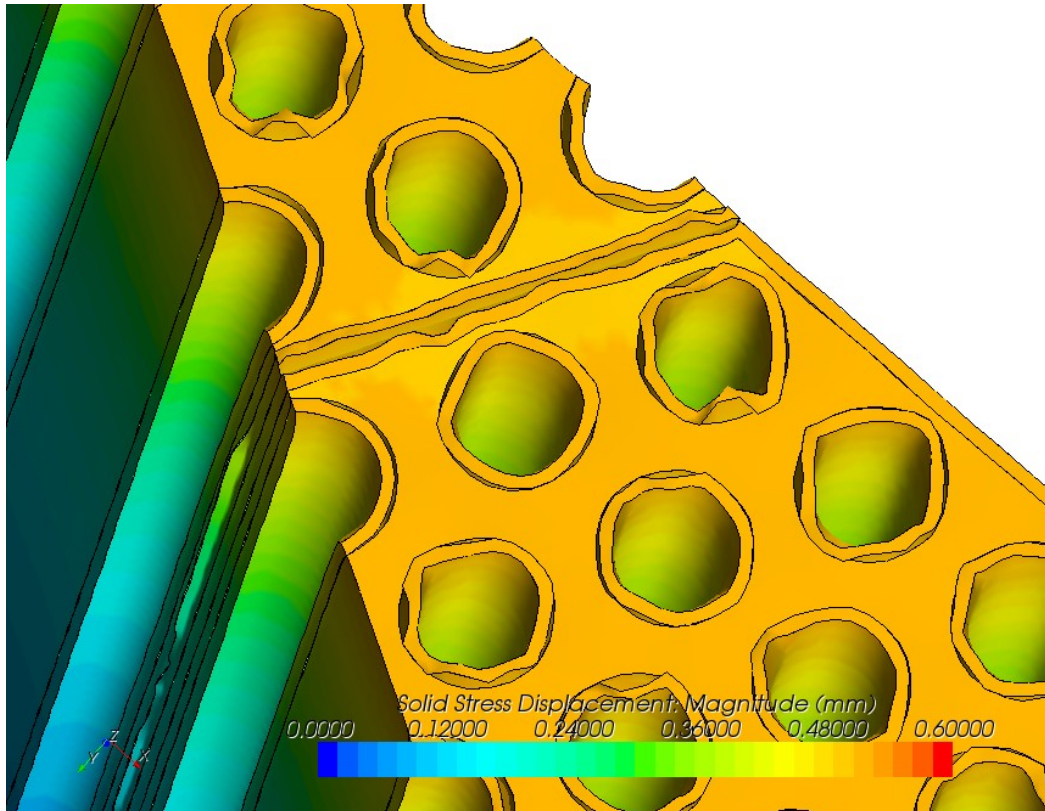


Fig. 6.3 Exaggerated displacement of fuel matrix and cladding

It can be seen that the coolant channel cladding tubes tend to buckle away from the channel wall, although it is unknown whether the strength of the cladding-wall bond is strong enough to resist the strain in the cladding. Nonetheless, it is clear that there is a

significant potential for coupled thermal-hydraulic and solid stress failure analysis of fuel elements in Star-CCM+. Future work should focus on better quantifying the stress properties of the fuel matrix and cladding.

7. CONCLUSIONS

The goals of this thesis were to modernize the analysis methods for a tungsten cermet fuel element design and make recommendations for the coolant channel configuration. In addition, the uncertainty in modern analysis tools has been assessed, as well as the ability of Star-CCM+ to resolve failure modes in a fuel element.

The main conclusions from the uncertainty analysis suggest that:

1. The k-epsilon two-layer realizable turbulence model, with polyhedral mesh cells and an axial stretching factor of four, is a stable and reasonably accurate set of methods to model conjugate heat transfer in a fuel element.
2. Numerical uncertainty can be reduced to a nearly-insignificant level for predicting fuel and coolant temperatures, but accounts for more than half the uncertainty in predicting pressure drop.
3. Uncertainty from the specific heat of hydrogen at high temperature can be a major contributor to the overall uncertainty in calculating peak fuel temperature.
4. The effect of the uncertainty from the thermal conductivity of the cermet fuel depends on the wall-to-peak temperature difference. If the temperature difference is larger than 100 K, the thermal conductivity can cause over half of the total uncertainty in predicting the peak fuel temperature.
5. The uncertainty from energy deposition calculations typically comprises about half of the total uncertainty in predicting the peak fuel temperature.

6. The combined Star-CCM+ and MCNP approach to simulating fuel elements is capable of predicting peak fuel temperature with about 3% uncertainty, bulk hydrogen exit temperature with about 2% uncertainty, and pressure drop with about 5% uncertainty.

These conclusions can be used to help guide priorities for improving NTR modeling.

The top three priorities should be (1) Running a validation experiment with low uncertainty, (2) Reduce the uncertainty for thermal conductivity of the cermet fuel, and (3) Reduce the uncertainty for the specific heat of hydrogen at high temperature.

The main conclusions from the parametric study suggest that:

1. The coolant channel cladding thickness is a hidden driver of the core critical mass, which reduces the competitiveness of small-diameter coolant channel designs.
2. Channel-by-channel flow zoning offers only a small reduction in peak fuel temperature as compared to element-by-element flow zoning.
3. Enrichment zoning is not a competitive method for managing power peaking for a small 10 klbf-thrust class core.
4. The ANL-10k design should be modified slightly with a smaller p/d to increase its peak fuel temperature safety margin.
5. By taking into account power startup-transients and the analysis uncertainty, a safe target peak fuel temperature is 2850 K.

6. Specific channel configurations which can achieve the target peak temperature are channel diameter of 0.12 cm with a p/d up to 1.8; a diameter of 0.18 cm with a p/d up to 1.5; and a diameter of 0.24 cm with a p/d of up to 1.4. The 0.12 cm-diameter case results in the lightest core.

In the multi-element failure mode analysis, it was shown that Star-CCM+ has the capability to couple a solid stress and strain model in with the conjugate heat transfer problem, which is very powerful tool for fuel element design.

This thesis has provided a set of simulation data which can be used to guide materials research and sample fuel element testing programs. In addition, several recommendations have been made for the best practices for NTR fuel modeling with modern methods, and the areas of highest priority for improving model accuracy.

REFERENCES

- [1] Drake, B., 2009, *Human Exploration of Mars Design Reference Architecture 5.0*, SP-2009-566, National Aeronautics and Space Administration, Johnson Space Center, Houston, TX.
- [2] Borowski, S., McCurdy, D., and Packard, T., 2009, "'7-Launch" NTR Space Transportation System for NASA's Mars Design Reference Architecture (DRA) 5.0, AIAA-2009-5308," American Institute of Aeronautics and Astronautics, Denver, CO.
- [3] Webb, J., Gross, B., and Taitano, W., 2011, "Conceptual Design of a CERMET NTR Fission Core Using Multiphysics Modeling Techniques," 47th AIAA Joint Propulsion Conference, San Diego, CA, 2011.
- [4] Walton, J., 1992, *Program ELM: A Tool for Rapid Thermal-Hydraulic Analysis of Solid-Core Nuclear Rocket Fuel Elements*, NASA Technical Memorandum 105867, Lewis Research Center, Cleveland, OH.
- [5] Stewart, M., and Schnitzler, B., 2007, "Thermal Hydraulics and Structural Analysis of the Small Nuclear Rocket Engine (SNRE) Core, AIAA 2007-5619," American Institute of Aeronautics and Astronautics Joint Propulsion Conference, Cincinnati, OH, 2007.
- [6] Seker, V., Thomas, J., and Downar, T., 2007, "Reactor Physics Simulations with Coupled Monte Carlo Calculation and Computational Fluid Dynamics," International Congerence on Emerging Nuclear Energy Systems, Istanbul, Turkey, 2007.
- [7] Ying, A., Abdou, M., Smolentsev, S., Munipalli, R., Youchison, D., Wilson, P., and Sawan, M., 2009, *Integrated Multi-Physics Simulation of Nuclear Components as an Essential Element in Developing Predictive Capabilities for DEMO*, University of California at Los Angeles, Los Angeles, CA.
- [8] Oak Ridge National Laboratory, 2011 *Consortium for Advanced Simulation of LWRs: A Project Summary*, Oak Ride National Laboratory, Oak Ridge, TN.

- [9] Todreas, N., and Kazimi, M., 1992, *Nuclear Systems I: Thermal Hydraulic Fundamentals*, Taylor & Francis Group, New York.
- [10] Dewar, J. A., 2004, *To the End of the Solar System*, The University Press of Kentucky, Lexington, KY.
- [11] Peery, S., Parsley, R., Anghaie, S., and Feller, G., 1993 "XNR2000 - A Near Term Nuclear Thermal Rocket Concept, CONF 930103," American Institute of Physics, pp. 1743-1752, 1993.
- [12] Argonne National Laboratory, 1966, *Nuclear Rocket Program Terminal Report, ANL-7236*, Atomic Energy Commission, Argonne, IL.
- [13] General Electric Nuclear Materials and Propulsion Operation, 1968, *710 High-Temperature Gas Reactor Program Summary Report, GEMP-600*, United States Atomic Energy Commission, Cincinnati, OH.
- [14] Waltar, A., and Reynolds, A., 1981, *Fast Breeder Reactors*, Pergamon Press: New York.
- [15] Pelowitz, D., 2008, *MCNPX User's Manual Version 2.6.0, LA-CP-07-1473*, Los Alamos National Laboratory, Los Alamos, NM.
- [16] Schnitzler, B., 2007, "Neutronics Models and Analysis of the Small Nuclear Rocket Engine (SNRE)," 43rd AIAA Joint Propulsion Conference, Cincinnati, OH, 2007.
- [17] Weng, T., Canabal, F., Chen, Y., and Cheng, G., 2010, "Multiphysics Computational Analysis of a Solid-Core Nuclear Thermal Engine Thrust Chamber," *AIAA Journal of Propulsion and Power*, **26**(3), pp. 407-414.
- [18] Durham, F., 1972, *Nuclear Engine Definition Study Preliminary Report Volume II - Supporting Studies (U), LA-5044-MS*, Los Alamos Scientific Laboratory, Los Alamos, NM.
- [19] Clough, J., Starkey, R., and Lewis, M. J., 2007, "Integrated Propulsion and Power Modeling for Bimodal Nuclear Thermal Rockets, AIAA 2007-5623," American Institute of Aeronautics and Astronautics Joint Propulsion Conference, Cincinnati, OH, 2007.

- [20] Fittje, J., 2007, "Upgrades to the NESS (Nuclear Engine System Simulation) Code," American Institute of Aeronautics and Astronautics Joint Propulsion Conference, Cincinnati, OH, 2007.
- [21] Hersman, E., Pleban, E., Clark, J., and Townsend, D., 1966, *Analytical Study of Some Thermal Stresses in a Nuclear Thermal Rocket Fuel Element (U)*, NASA TM X-52188, Lewis Research Center, Cleveland, OH.
- [22] Cheng, G., Ito, Y., Ross, D., Chen, Y., and Wang, T., 2007, "Numerical Simulations of Single Flow Element in a Nuclear Thermal Thrust Chamber," 39th AIAA Thermophysics Conference, Miami, FL, 2007.
- [23] Kalvinskas, J., 1962, *Heat Transfer and Fluid Dynamic Aspects of Nuclear Rocket Engines, Notes for the 1962 National Science Foundation Advanced Subject Matter on Nuclear Rocket Propulsion*, Florida Engineering and Industrial Experiment Station, Gainesville, FL,.
- [24] Hussey, C., Woike, O., and Zwick, J., 1965, *Conceptual Mechanical Design for a Fast Energy Spectrum Nuclear Rocket Engine*, General Electric Nuclear Materials & Propulsion Operation, Cincinnati, OH.
- [25] Stewart, M., and Schnitzler, B., 2008, "Thermal Hydraulic and Structural Analysis of Nuclear Thermal Propulsion Reactor Core Components," 44th AIAA Joint Propulsion Conference, Hartford, CT, 2008.
- [26] Cardoni, J., and Rizwan-uddin, 2011, "Nuclear Reactor Multi-Physics Simulations with Coupled MCNP5 and Star-CCM+," International Conference on Mathematics and Computational Methods Applied to Nuclear Science and Engineering, Rio de Janeiro, Brazil, 2011.
- [27] CD-Adapco, 2011, *User Guide: Star-CCM+ Version 6.04.014*, CD-Adapco.
- [28] Greitzer, E., Tan, C., and Graf, M., 2004, *Internal Flow: Concepts and Applications*, Cambridge University Press, Cambridge, UK.
- [29] Bird, R., Stewart, W., and Lightfoot, E., 2007, *Transport Phenomena*, John Wiley & Sons, Inc., New York.
- [30] Bust, J., and Stewart, R., 1965, *A Compilation of the Property Differences of Ortho*

and Para Hydrogen, NBS-8812, National Bureau of Standards, 1965.

- [31] Patch, R., 1971, *Thermodynamic Properties and Theoretical Rocket Performance of Hydrogen to 100000 K and $1.01325 \times 10^8 \text{ N/m}^2$* , SP-3069, National Aeronautics and Space Agency.
- [32] Conant, J., Eduskuty, F., Huston, J., and Thome, F., 1973, *The Conversion of Para to Orthohydrogen in a Gamma-Ray and Neutron Radiation Field*, LA-5436-MS, Los Alamos National Lab, Los Alamos, NM.
- [33] McCarty, R., 1975, *Hydrogen Technological Survey: Thermophysical Properties*, SP-3089, National Aeronautics and Space Administration.
- [34] Taylor, M., 1964, *Experimental Local Heat-Transfer and Average Friction Data for Hydrogen and Helium Flowing in a Tube at Surface Temperatures Up to 5600 R*, NASA TN D-2280, National Aeronautics and Space Administration, Lewis Research Center, Cleveland, OH.
- [35] Stubbs, R., Kim, S., and Benson, T., 1991, "Computational Fluid Dynamics Studies of Nuclear Rocket Performance, AIAA-91-3577," AIAA Conference on Advanced SEI Technologies, Cleveland, OH, 1991.
- [36] Indrajit, C., and Webb, J. A., 2011, "Analytical Determination of the Thermophysical Properties of W-UO₂ and W-UN CERMET Nuclear Fuels," Nuclear Materials.
- [37] Hawkes, B., 2012, *Determining the Effective Thermal Conductivity for 60% (Vol) Uranium Oxide and 40% (Vol) Tungsten*, Idaho National Laboratory, Idaho Falls, ID.
- [38] Aerojet Nuclear Systems Company, 1970, *Materials Properties Data Book Volume 3: Nonmetallics and Appendices*, Aerojet-General, Sacramento, CA.
- [39] Brown, F. B., 2009, *A Review of Monte Carlo Criticality Calculations - Convergence, Bias, Statistics*, LA-UR-08, Los Alamos National Laboratory, Los Alamos, NM.
- [40] Allen, R., Manning, B., Chlapek, T., Guan, J., Rao, S., Ferulli, R., and Howe, S., 2011, "Preliminary Mission Architecture for Mars Sample Return Utilizing Nuclear Thermal Rockets," Nuclear and Emerging Technologies for Space, Albuquerque,

NM, 2011.

- [41] American Society of Mechanical Engineers, 2009, *Standard for Verification and Validation in Computational Fluid Dynamics and Heat Transfer*, ASME V&V 20-2009, ASME.
- [42] Blazek, J., 2001, *Computational Fluid Dynamics: Principles and Applications*, Elsevier, Amsterdam.
- [43] Lassner, E., and Schubert, W., 1999, *Tungsten: Properties, Chemistry, Technology Element, Alloys, and Chemical Compounds*, Kluwer Academic / Plenum Publishers, New York.
- [44] Chen, Y., Arbeiter, F., and Schlindwein, G., 2012, "A Comparative Study of Turbulence Models for Conjugate Heat Transfer to Gas Flow in a Heated Mini-Channel," *Numerical Heat Transfer*, **61**, pp. 38-60.
- [45] Pointer, D., Smith, J., Tentner, A., and Fischer, P., 2009, *Advanced Thermal Hydraulics Simulation - Part II*, U.S. Department of Energy, Chicago.
- [46] Westinghouse Astronuclear Laboratory, 1968, *NRX-A6 Final Report*, WANL-TNR-224.
- [47] Westinghouse Astronuclear Laboratory, 1968, *NRX-A6 Transducer Evaluation Report*, WANL-TME-1863, Aerojet-General Corporation.
- [48] Aerojet General Corporation, 1967, *Predicted Measurement Uncertainties*, NRX-A6, AEC-NASA Space Nuclear Propulsion Office, Sacramento, CA.
- [49] Schnitzler, B., and Borowski, S., 2010, "Enrichment Zoning Options for the Small Nuclear Rocket Engine (SNRE), AIAA 2010-6816," American Institute of Aeronautics and Astronautics 46th Joint Propulsion Conference, Nashville, TN, 2010.
- [50] International Atomic Energy Agency, 2008, *Thermophysical Properties of Materials for Nuclear Engineering: A Tutorial and Collection of Data*, IAEA, Vienna.

APPENDIX

MATLAB Scripts

NTR_sizing.m

```

% NTR_sizing.m
% Brad Appel May 2012
% This code takes in requirements for thrust, Isp, nozzle area ratio,
and
% chamber pressure - and calculates the required mass flow rate,
chamber
% temperature, and total reactor power. It calls the subroutine
rocket.m.

clear all
close all
clear global
MatFile = 'XNR2000.mat';           % File name

%%% INPUTS


---


% Performance
Thrust = 25.0*4.448e3;   % [N] - thrust - 1 pound = 4.448 N
Isp = 900;               % [s]
Eps = 200;               % [] - Nozzle area ratio
Pc = 600*6894.76;       % [Pa]

%%% SIMPLE CALCULATIONS


---


% Rocket parameters
[Tc mdot gamma Pow At ve Pe Te cf c_star] = rocket(Thrust,Isp,Eps,Pc);

% Basic calculations
Dt = 2*sqrt(At/pi);
De = 2*sqrt(Eps*At/pi);

%%% REPORT RESULTS


---


fprintf('\n***** SUMMARY REPORT for %s*****\n',MatFile)
fprintf('---From Rocket and Neutronics Calculations---\n')
fprintf('\tChamber temp = %4.0f K\n',Tc)
fprintf('\tTotal flow rate = %3.3f kg/s\n',mdot)
fprintf('\tTotal power = %1.3f MW\n',Pow*1e-6)
fprintf('\tThroat diameter = %2.2f cm\n',Dt*100)
fprintf('\tExit diameter = %3.1f cm\n',De*100)

```

```
fprintf('\tExit pressure = %3.3f kPa\n',Pe/1000)
fprintf('\tAverage nozzle temperature = %3.1f K\n', (0.5*Te+0.5*Tc))
```

Rocket.m

```
function [Tc mdot gamma Pow At ve Pe Te cf c_star] =
rocket(Thrust,Isp,Eps,Pc)
% rocket.m
% Brad Appel May 2012
% This function takes in the rocket performance requirements and
% iteratively calculates the required chamber temperature, mass flow
rate,
% reactor power, and other flow parameters.

% Constants
g = 9.80665;           % [m/s^2]
Ru = 8314.46;         % [J/kmol-K] - universal gas constant
MolW = 2.016;         % [g/mol] - exhaust molecular weight
hv = 451.9e3;         % [J/kg] - H2 heat of vaporization
c = Isp*g;            % [m/s] - effective exhaust velocity
cf_eff = 0.98;        % nozzle efficiency

%%% While-loop to converge on exhaust velocity %%%
% Initial guesses
Ae = pi*1^2/4;        % [m^2]
Pe = 1*6894.76;       % [Pa]
mdot = 12;            % [kg/s]
ve = c - Ae*Pe/mdot;  % [m/s] - exhaust velocity
ve_guess = 9000;      % [m/s]

while abs(ve_guess-ve) > 1
    ve_guess = ve;
    fprintf('\nworking\n')
    % Determine gamma (ratio of specific heats)
    % Initial guesses
    T_guess = 2900;    % [K]
    Tc = 2800;         % [K]

    %%% Inner While-loop to converge on chamber temperature %%%
    while abs(T_guess-Tc) > 1

        T_guess = Tc;    % [K]

        T_gam = 1443;
        cp = -5.4373e-13*T_gam^5 + 5.8506e-9*T_gam^4 - 2.1053e-
5*T_gam^3 + 3.3433e-2*T_gam^2 - 2.1912e1*T_gam + 1.9304e4;    % [J/kg-K]
- McCarty 1975
%         cp = 4.33e-9*T_guess^4 - 1.8e-5*T_guess^3 + 2.58e-2*T_guess^2
- 13.6*T_guess + 1.68e4;    % 1964, J/kg-K
        R = Ru / MolW;
```

```

cv = cp - R;
gamma = cp / cv;
%      gamma = 1.40;

% Determine nozzle exit mach number
Me = Mach_exit(Eps, gamma);

% Calculate exit pressure ratio
Pe_Pc = 1 / (1 + ((gamma-1)/2)*Me^2)^(gamma/(gamma-1));
Pe = Pe_Pc*Pc;      % [Pa] - exit pressure

% Chamber temperature
Tc = (gamma-1)*ve_guess^2 / (2*gamma*R*(1-Pe_Pc^((gamma-1)/gamma)));

% Characteristic velocity c*
a = sqrt(gamma*R*Tc);      % [m/s] - speed of sound in chamber
c_star = a / (gamma*sqrt((2/(gamma+1))^(gamma+1)/(gamma-1)));

% Thrust coefficient
cf = sqrt((2*gamma^2/(gamma-1))* (2/(gamma+1))^(gamma+1)/(gamma-1) * (1-Pe_Pc^((gamma-1)/gamma))) + Eps*Pe_Pc;
cf = cf*cf_eff;
PcAt = Thrust / cf;
At = PcAt / Pc;      % [m^2]
Ae = Eps*At;      % [m^2]

% Mass flow rate
mdot = PcAt / c_star;      % [kg/s]

end

% New guess for exhaust velocity
ve = c - Ae*Pe/mdot;

end

% Nozzle exit temperature
Te = Tc / (1 + ((gamma-1)/2)*Me^2);

% Integrate over temperature range to calculate power required
T_range = 21:Tc;      % [K]
for i = 1:length(T_range)
    cp_H2(i) = -5.4377e-13*T_range(i)^5 + 5.8506e-9*T_range(i)^4 - 2.1053e-5*T_range(i)^3 + 3.3433e-2*T_range(i)^2 - 2.1912e1*T_range(i) + 1.9304e4;      % [J/kg-K] - McCarty 1975
    %      cp_H2(i) = 4.33e-9*T_range(i)^4 - 1.8e-5*T_range(i)^3 + 2.58e-2*T_range(i)^2 - 13.6*T_range(i) + 1.68e4;      % 1964 paper
end

```

```
% Total required power
Pow = mdot*(hv + trapz(T_range,cp_H2));
```

Mach_exit.m

```
function Me = Mach_exit(Eps,gamma)
% Mach_exit.m
% Brad Appel May 2012
% Assumes supersonic conditions, range is M = 1 to 10

M = [1.001:0.001:10];

Eps_guess = (1./M).*((2/(gamma+1)).*(1+((gamma-1)/2)*M.^2)).^((gamma+1)/(gamma-1)).^(1/2);
% Eps_guess = (1./M).*((1+((gamma-1)/2)*M.^2)/((gamma+1)/2)).^((gamma+1)/(2*(gamma-1)));

[value index] = min(abs(Eps - Eps_guess));

Me = M(index);
```

Power_Zoning.m

```
% Power_Zoning.m
% Brad Appel May 2012
% This code takes inputs for the total core power, flow rate, size,
% channel configuration, and power profile - and calculates both the
% required mass flow rate zones or enrichment zones.

clear all; close all;

% Inputs
Q_10k = 222e6; % [W] - thermal power for 10 klbf core
Q_25k = 554e6; % [W] - thermal power for 25 klbf core
mdot_10k = 5.14; % [kg/s]
mdot_25k = 12.86; % [kg/s]
% Core dimensions
% Entries 1 through 9 correspond to parametric study cases; Entry 10 is
the
% ANL-10k design; Entry 11 is Case 5 with enrichment zoning; Entry 12
is
% the design used for the failure mode stress model.
D = [78.41 47.52 39.51 58.23 42.73 37.2 53.21 41.12 36.45 42.86 50.34
62.7]/100; % [m] - Core diameter & length
p = [0.18 0.216 0.252 0.27 0.324 0.378 0.36 0.432 0.504 0.3451 0.324
0.336]/100; % [m] - channel pitch
```

```

VF = [0.403066525 0.279907309 0.205646186 0.403066525 0.279907309
0.205646186 0.403066525 0.279907309 0.205646186 0.220073 0.279907309
0.462704]; % [] - core void fraction
A_cell = (sqrt(3)/4)*p.^2; % [m^2] - area of trinagular lattice
cell
A_core = pi*D.^2/4; % [m^2] - core cross sectional area
n_ch = 0.5*(A_core./A_cell); % [] - number of channels in core
mdot_ch_10k = mdot_10k./n_ch; % [kg/s] - flow rate per channel
with no zoning
mdot_ch_25k = mdot_25k./n_ch; % [kg/s] - flow rate per channel
with no zoning
V_fuel = D.*A_core.*(1-VF); % [m^3] - volume of fuel in core
q_10k = Q_10k ./ V_fuel; % [W/m^3]
q_10k(10) = 212e6 / V_fuel(10); % ANL-10k had a different power
level
q_25k = Q_25k ./V_fuel; % [W/m^3]
n_ch_rad = round((D/2) ./ p); % Number of channels across core
radius
low_enr = 0.57; % Low-end of U-235 enrichment
high_enr = 0.9315; % High-end of U-235 enrichment
del_enr = high_enr-low_enr;

% Range for r/R
r = 0:0.00005:1;
% Calculate power profiles
for i = 1:length(r)
    % Case 1
    % q1r(i) = 22.641*r(i)^5 - 44.076*r(i)^4 + 29.393*r(i)^3 -
8.2522*r(i)^2 + 0.3527*r(i) + 1.27;
    q1r(i) = 7.2704*r(i)^5 - 12.196*r(i)^4 + 6.8839*r(i)^3 -
2.18*r(i)^2 - 0.0494*r(i) + 1.26; % Radial Profile
    q1a(i) = 4.4307*r(i)^4 - 9.2442*r(i)^3 + 1.9495*r(i)^2 +
2.4646*r(i) + 0.5422; % Axial Profile

    % Case 2
    % q2r(i) = 67.103*r(i)^6 - 171.2*r(i)^5 + 163.53*r(i)^4 -
71.504*r(i)^3 + 13.155*r(i)^2 - 0.9218*r(i) + 1.1951;
    q2r(i) = 12.154*r(i)^5 - 21.499*r(i)^4 + 12.393*r(i)^3 -
3.0718*r(i)^2 - 0.013*r(i) + 1.21;
    q2a(i) = 2.8355*r(i)^4 - 5.7667*r(i)^3 - 0.184*r(i)^2 + 2.7154*r(i)
+ 0.5776;

    % Case 3
    % q3r(i) = 58.171*r(i)^6 - 151.37*r(i)^5 + 147.94*r(i)^4 -
66.386*r(i)^3 + 12.718*r(i)^2 - 1.0429*r(i) + 1.2115;
    q3r(i) = 8.9325*r(i)^5 - 16.107*r(i)^4 + 9.8778*r(i)^3 -
2.845*r(i)^2 + 0.0074*r(i) + 1.21;
    q3a(i) = 3.5477*r(i)^4 - 7.6873*r(i)^3 + 1.638*r(i)^2 + 2.057*r(i)
+ 0.6372;

    % Case 4

```

```

%      q4r(i) = 76.141*r(i)^6 - 199.74*r(i)^5 + 198.41*r(i)^4 -
92.245*r(i)^3 + 19.399*r(i)^2 - 1.7897*r(i) + 1.2217;
      q4r(i) = 11.887*r(i)^5 - 20.845*r(i)^4 + 11.73*r(i)^3 -
2.6311*r(i)^2 - 0.1487*r(i) + 1.21;
      q4a(i) = 2.612*r(i)^4 - 5.7183*r(i)^3 + 0.1771*r(i)^2 + 2.4738*r(i)
+ 0.6106;

% Case 5
%      q5r(i) = 60.812*r(i)^6 - 159.45*r(i)^5 + 158.29*r(i)^4 -
73.243*r(i)^3 + 14.952*r(i)^2 - 1.247*r(i) + 1.1798;
      q5r(i) = 7.6749*r(i)^5 - 12.044*r(i)^4 + 5.7762*r(i)^3 -
1.3396*r(i)^2 - 0.0902*r(i) + 1.17;
      q5a(i) = 1.6859*r(i)^4 - 3.4068*r(i)^3 - 1.6484*r(i)^2 +
2.9779*r(i) + 0.5744;

% Case 6
%      q6r(i) = 44.937*r(i)^6 - 112.18*r(i)^5 + 105.41*r(i)^4 -
46.029*r(i)^3 + 8.7433*r(i)^2 - 0.7587*r(i) + 1.1686;
      q6r(i) = 10.862*r(i)^5 - 19.314*r(i)^4 + 11.099*r(i)^3 -
2.5913*r(i)^2 - 0.0608*r(i) + 1.175;
      q6a(i) = 4.3254*r(i)^4 - 9.0511*r(i)^3 + 2.2942*r(i)^2 +
2.0325*r(i) + 0.6162;

% Case 7
%      q7r(i) = 86.191*r(i)^6 - 228.75*r(i)^5 + 233.15*r(i)^4 -
114.22*r(i)^3 + 26.866*r(i)^2 - 2.8875*r(i) + 1.227;
      q7r(i) = 16.476*r(i)^5 - 29.642*r(i)^4 + 17.164*r(i)^3 -
3.7207*r(i)^2 - 0.0591*r(i) + 1.165;
      q7a(i) = 2.257*r(i)^4 - 4.7036*r(i)^3 - 0.585*r(i)^2 + 2.6108*r(i)
+ 0.6135;

% Case 8
%      q8r(i) = 98.191*r(i)^6 - 264.23*r(i)^5 + 269.88*r(i)^4 -
129.62*r(i)^3 + 28.762*r(i)^2 - 2.7405*r(i) + 1.2235;
      q8r(i) = 12.731*r(i)^5 - 23.061*r(i)^4 + 13.742*r(i)^3 -
3.3318*r(i)^2 - 0.0221*r(i) + 1.18;
      q8a(i) = 2.3726*r(i)^4 - 4.9642*r(i)^3 - 0.3486*r(i)^2 +
2.5435*r(i) + 0.6104;

% Case 9
%      q9r(i) = 53.255*r(i)^6 - 142.23*r(i)^5 + 146.66*r(i)^4 -
72.994*r(i)^3 + 17.33*r(i)^2 - 2.0077*r(i) + 1.2432;
      q9r(i) = 10.343*r(i)^5 - 18.418*r(i)^4 + 10.685*r(i)^3 -
2.5679*r(i)^2 - 0.1062*r(i) + 1.2;
      q9a(i) = 3.0014*r(i)^4 - 6.2189*r(i)^3 + 0.4593*r(i)^2 + 2.362*r(i)
+ 0.6198;

% ANL 10k
      qanlr(i) = 0.4167*r(i)^3 - 1.2514*r(i)^2 + 0.0369*r(i) + 1.295;
%      qanlr(i) = 2.3024*r(i)^5 - 2.9734*r(i)^4 + 1.241*r(i)^3 -
0.9921*r(i)^2 - 0.0035*r(i) + 1.235;

```

```

    % XCase 5 w/ Enrichment zones
    %   qenr(i) = 12.182*r(i)^5 - 22.121*r(i)^4 + 13.205*r(i)^3 -
3.2264*r(i)^2 - 0.0176*r(i) + 1.18;
    %   qenr(i) = 15.194*r(i)^5 - 29.091*r(i)^4 + 18.381*r(i)^3 -
4.5221*r(i)^2 + 0.1025*r(i) + 1.145;
    qenr(i) = 1.4737*r(i)^3 - 1.7539*r(i)^2 + 0.0798*r(i) + 1.175;

    % Failure Mode Case
    qclar(i) = 14.307*r(i)^5 - 25.931*r(i)^4 + 15.46*r(i)^3 -
3.7109*r(i)^2 - 0.0247*r(i) + 1.19

end

% Re-normalize power profiles and calculate power in each ring
q1r_avg = sum(q1r.*r)/sum(r);
q1r = q1r / (sum(q1r.*r)/sum(r));
q2r = q2r / (sum(q2r.*r)/sum(r));
q3r = q3r / (sum(q3r.*r)/sum(r));
q4r = q4r / (sum(q4r.*r)/sum(r));
q5r = q5r / (sum(q5r.*r)/sum(r));
q6r = q6r / (sum(q6r.*r)/sum(r));
q7r = q7r / (sum(q7r.*r)/sum(r));
q8r = q8r / (sum(q8r.*r)/sum(r));
q9r = q9r / (sum(q9r.*r)/sum(r));
qanlr = qanlr / (sum(qanlr.*r)/sum(r));
qenr = qenr / (sum(qenr.*r)/sum(r));
qclar = qclar / (sum(qclar.*r)/sum(r));
q5p = q5r / max(q5r);

% Determine the total power generated in each ring
for i = 1:length(r)
    if i > 1
        r2 = r(i)*D(1)/2;
        r1 = r(i-1)*D(1)/2;
        pow1(i) = pi*(r2^2-r1^2)*q1r(i)*D(1)*q_10k(1)*(1-VF(1)); % [W]
        voll1(i) = pi*(r2^2-r1^2)*D(1)*(1-VF(1));
        pow2(i) = pi*(r(i)^2-r(i-1)^2)*q2r(i)*D(2)^3/4*q_10k(2)*(1-
VF(2));
        pow3(i) = pi*(r(i)^2-r(i-1)^2)*q3r(i)*D(3)^3/4*q_10k(3)*(1-
VF(3));
        pow4(i) = pi*(r(i)^2-r(i-1)^2)*q4r(i)*D(4)^3/4*q_10k(4)*(1-
VF(4));
        pow5(i) = pi*(r(i)^2-r(i-1)^2)*q5r(i)*D(5)^3/4*q_10k(5)*(1-
VF(5));
        pow6(i) = pi*(r(i)^2-r(i-1)^2)*q6r(i)*D(6)^3/4*q_10k(6)*(1-
VF(6));
        pow7(i) = pi*(r(i)^2-r(i-1)^2)*q7r(i)*D(7)^3/4*q_10k(7)*(1-
VF(7));
        pow8(i) = pi*(r(i)^2-r(i-1)^2)*q8r(i)*D(8)^3/4*q_10k(8)*(1-
VF(8));
        pow9(i) = pi*(r(i)^2-r(i-1)^2)*q9r(i)*D(9)^3/4*q_10k(9)*(1-
VF(9));
    end
end

```

```

        powanl(i) = pi*(r(i)^2-r(i-
1)^2)*qanlr(i)*D(10)^3/4*q_10k(10)*(1-VF(10));
        powenr(i) = pi*(r(i)^2-r(i-1)^2)*qenr(i)*D(5)^3/4*q_10k(5)*(1-
VF(5));
        powcla(i) = pi*(r(i)^2-r(i-
1)^2)*qclar(i)*D(12)^3/4*q_10k(12)*(1-VF(12));
    end
end

% Radial Peaking Factors
r_peak = [max(q1r) max(q2r) max(q3r) max(q4r) max(q5r) max(q6r)
max(q7r) max(q8r) max(q9r) max(qanlr) max(qenr) max(qclar)];

% Calculate Mass Flow Rate Zoning
drz = 1/n_ch_rad(1);      % Increment for radial zones
rz = 0:(1/9):1;
set = 10;
for j = 2:length(rz)
    a = find(r >= rz(j-1));
    low_ind = a(1);
    b = find(r >= rz(j));
    high_ind = b(1);
    Dj = D(set);
    % Calculate area in ring
    area(j) = pi*((r(high_ind)*Dj/2)^2 - (r(low_ind)*Dj/2)^2);
    % Calculate number of channels in ring
    n_ch_rz(j) = (area(j)/A_core(set))*n_ch(set);
    % Calculate total power in ring
    pow_tot(j) = sum(powanl(low_ind:high_ind)); % [W]
    % Calculate required mass flow rate per channel in ring
    mdot_rz(j) = pow_tot(j)*(mdot_10k/Q_10k)/n_ch_rz(j);
    % Find maximum peaking factor in ring
    r_peak_max(j) = max(qanlr(low_ind:high_ind));
    % Find average peaking factor wrt max in ring
    r_peak_avg(j) =
sum(qanlr(low_ind:high_ind))/length(q5r(low_ind:high_ind));
    enr(j) = high_enr / r_peak_avg(j);

end

% Compress the range of enrichments
enr = enr - min(enr(2:end));
enr = enr/max(enr);
for j = 2:length(rz)
    % Determine target enrichment in ring
    disad(j) = (r_peak_avg(j) - min(r_peak_avg))/(max(r_peak_avg) -
min(r_peak_avg));
    enrich(j) = low_enr + del_enr*enr(j);
end

% Check that the integral parameters are conserved
mdot_check = sum(mdot_rz.*n_ch_rz);
pow_check = sum(pow_tot);

```



```

% Setup
ci0 = 50;      % cell index for drums
si0 = 500;    % surface index for drums
m = 0.1;      % arbitrary margin added so lattice cell surfaces work
filename = 'newpow4.txt';
fid = fopen(filename, 'wt');
fprintf(fid, 'ANL 10klbf-thrust core model \n')
fprintf(fid, 'C Configuration based on the ANL-7236 Terminal Report \n')

%%%%%%%% %%%%%%%%% %%%%%%%%% %%%%%%%%% %%%%%%%%% %%%%%%%%% %%%%%%%%% %%%%%%%%% %%%%%%%%% %%%%%%%%% %%%%%%%%% %%%%%%%%%
%%%%%%%% %%%%%%%%% %%%%%%%%% %%%%%%%%% CELL CARD %%%%%%%%% %%%%%%%%% %%%%%%%%% %%%%%%%%% %%%%%%%%% %%%%%%%%% %%%%%%%%%
%%%%%%%% %%%%%%%%% %%%%%%%%% %%%%%%%%% %%%%%%%%% %%%%%%%%% %%%%%%%%% %%%%%%%%% %%%%%%%%% %%%%%%%%% %%%%%%%%% %%%%%%%%%
fprintf(fid, 'C Cell Card*****
\n')
fprintf(fid, '1  1  -%2.4s          -200 100 -102    u=1 imp:n=1  $
Coolant channel\n', rho_H2)
fprintf(fid, '2  2   %2.4s          200 -201 100 -101    u=1 imp:n=1  $
Coolant Channel cladding \n', totdens_W_chan)
fprintf(fid, '3  3   %2.4s          200 101    u=1 imp:n=1  $
Top MoUO2 channel section \n', totdens_MoUO2)
fprintf(fid, '4  4   %2.4s          201 -101    u=1 imp:n=1  $
Bottom WUO2 channel section \n', totdens_WUO2)
fprintf(fid, '5  0          -300 lat=2 fill=1 u=2
imp:n=1  $ Channels Lattice Cell \n')
fprintf(fid, '6  0          -301 fill=2 imp:n=1 u=3
$ Channels Window \n')

fprintf(fid, '7  1  -%2.4s          -202 102 -106    u=10 imp:n=1  $
Axial ref coolant channel\n', rho_H2)
fprintf(fid, '8  2  -%2.4s          202 -203 102 -106    u=10 imp:n=1  $
Axial ref coolant Channel cladding \n', totdens_W_chan)
fprintf(fid, '9  5   %2.4s          203    u=10 imp:n=1  $
BeO section \n', totdens_BeO)
fprintf(fid, '10 0          -313 lat=2 fill=10 u=20
imp:n=1  $ Axial ref channels Lattice Cell \n')
fprintf(fid, '11 0          -314 fill=20 imp:n=1
u=30    $ Axial ref channels Window \n')

fprintf(fid, '12 3   %2.4s          -306 #6 u=3 imp:n=1  $
MoUO2 element fill \n', totdens_MoUO2)
fprintf(fid, '13 1  -%2.4s          306 -307 u=3 imp:n=1  $
MoUO2 element gap \n', rho_H2)
fprintf(fid, '14 6   %2.4s          307 -308 u=3 imp:n=1  $
MoUO2 element grid \n', totdens_WRe)
fprintf(fid, '15 5   %2.4s          -309 #11 u=30 imp:n=1  $
Axial ref element fill \n', totdens_BeO)
fprintf(fid, '16 1  -%2.4s          309 -310 u=30 imp:n=1  $
Axial ref element gap \n', rho_H2)
fprintf(fid, '17 6   %2.4s          310 -311 u=30 imp:n=1  $
Axial ref element grid \n', totdens_WRe)
fprintf(fid, '18 4   %2.4s          -302 #6 u=3 imp:n=1  $
WUO2 element fill \n', totdens_WUO2)

```

```

fprintf(fid,'19  2  %2.4s                               302 -303 u=3 imp:n=1  $
WUO2 element clad \n', totdens_W_chan)
fprintf(fid,'20  1  -%2.4s                               303 -304 u=3 imp:n=1  $
WUO2 element gap \n', rho_H2)
fprintf(fid,'21  6  -%2.4s                               304 -305 u=3 imp:n=1  $
WUO2 element grid \n', totdens_WRe)
fprintf(fid,'22  0                                     -312   lat=2 fill=3 u=4
imp:n=1  $ Fill card for each element assembly \n')
fprintf(fid,'23  0                                     -400 100 -102 fill=4 imp:n=1
\n')
fprintf(fid,'24  0                                     -315   lat=2 fill=30
u=40 imp:n=1  $ Fill card for each element assembly \n')
fprintf(fid,'25  0                                     -400 102 -106 fill=40 imp:n=1
\n')
fprintf(fid,'30  6  %2.4s                               400 -401 100 -106 imp:n=1  $
Support Grid Edge \n', totdens_WRe)
fprintf(fid,'31  1  -%2.4s                               401 -402 100 -106 imp:n=1  $
Radial gap 1 \n', rho_H2)
fprintf(fid,'32  7  %2.4s                               402 -403 100 -106 imp:n=1  $
Coolant Tubes \n', totdens_Inco718)

% LOOP TO DEFINE DRUM CELLS
ci = ci0; si = si0;      % cell and surface indicies
s_in1 = 407; s_out1 = 408; % inner and outer radial surfaces of
reflector
s_in2 = 406; s_out2 = 409; % radial range of reflector clearance gaps
s_in3 = 405; s_out3 = 410; % radial range of reflector clearance gap
s_in4 = 403; s_out4 = 412; % radial range of reflector clearance gap
s_bot1 = 100; s_top1 = 103; % bottom and top surfaces of fixed radial
reflector
s_bot2 = 103; s_top2 = 104; % bottom and top surfaces of radial
reflector gap 1
s_bot3 = 104; s_top3 = 105; % bottom and top surfaces of moving radial
reflector
s_bot4 = 105; s_top4 = 107; % bottom and top surfaces of radial
reflector gap 2
s_bot5 = 100; s_top5 = 107; % bottom and top surfaces of radial
reflector structure

for i = 1:n
    fprintf(fid,'C *****REFLECTOR SEGMENT AND SHIM, GAPS, AND CASE %i
***** \n',i)
    fprintf(fid,'%i  8  %2.4s  %i -%i %i -%i %i -%i      imp:n=1  $
Fixed shim reflector segment
\n',ci,totdens_Be,s_bot1,s_top1,s_in1,s_out1,si+6,si)
    fprintf(fid,'%i  0          %i -%i %i -%i %i -%i      imp:n=1  $
Shim reflector segment axial gap 1
\n',ci+1,s_bot2,s_top2,s_in1,s_out1,si+6,si)
    fprintf(fid,'%i  8  %2.4s  %i -%i %i -%i %i -%i      imp:n=1  $
Moving shim reflector segment
\n',ci+2,totdens_Be,s_bot3,s_top3,s_in1,s_out1,si+6,si)

```

```

    fprintf(fid,'%i 0 %i -%i %i -%i %i -%i imp:n=1 $
Shim reflector segment axial gap 2
\n',ci+3,s_bot4,s_top4,s_in1,s_out1,si+6,si)
    fprintf(fid,'%i 0 %i -%i %i -%i %i -%i %i %i %i %i
imp:n=1 $ Shim reflector gap
\n',ci+4,s_bot5,s_top5,s_in2,s_out2,si+7,si+1,ci,ci+1,ci+2,ci+3)
    fprintf(fid,'%i 9 %2.4s %i -%i %i -%i %i -%i %i %i %i %i %i
imp:n=1 $ Shim case
\n',ci+5,totdens_SS316,s_bot5,s_top5,s_in3,s_out3,si+8,si+2,ci,ci+1,ci+
2,ci+3,ci+4)
    fprintf(fid,'%i 7 %2.4s %i -%i %i -%i %i -%i
\n',ci+6,totdens_Inco718,s_bot5,s_top5,s_in4,s_out4,si+9,si+3)
    fprintf(fid,'%i %i %i %i %i %i %i imp:n=1 $
Shim reflector pressure vessel \n',ci,ci+1,ci+2,ci+3,ci+4,ci+5)

    if i == n
        fprintf(fid,'%i 8 %2.4s %i -%i %i -%i %i -%i imp:n=1
$ Fixed large reflector segment
\n',ci+7,totdens_Be,s_bot1,s_top1,s_in1,s_out1,si0+5,si+11)
        fprintf(fid,'%i 0 %i -%i %i -%i %i -%i imp:n=1
$ Large reflector segment axial gap 1
\n',ci+8,s_bot2,s_top2,s_in1,s_out1,si0+5,si+11)
        fprintf(fid,'%i 8 %2.4s %i -%i %i -%i %i -%i imp:n=1
$ Moving large reflector segment
\n',ci+9,totdens_Be,s_bot3,s_top3,s_in1,s_out1,si0+5,si+11)
        fprintf(fid,'%i 0 %i -%i %i -%i %i -%i imp:n=1
$ Large reflector segment axial gap 2
\n',ci+10,s_bot4,s_top4,s_in1,s_out1,si0+5,si+11)
        fprintf(fid,'%i 0 %i -%i %i -%i %i -%i %i %i %i %i
imp:n=1 $ Large reflector gap
\n',ci+11,s_bot5,s_top5,s_in2,s_out2,si0+4,si+10,ci+7,ci+8,ci+9,ci+10)
        fprintf(fid,'%i 9 %1.4s %i -%i %i -%i %i -%i %i %i %i %i
%i imp:n=1 $ Large case
\n',ci+12,totdens_SS316,s_bot5,s_top5,s_in3,s_out3,si0+3,si+9,ci+7,ci+8
,ci+9,ci+10,ci+11)
        fprintf(fid,'%i 7 %2.4s %i -%i %i -%i %i -%i imp:n=1
$ Inner Pressure Vessel
\n',ci+13,totdens_Inco718,s_bot5,s_top5,403,405,si0+3,si+9)
        fprintf(fid,'%i 7 %2.4s %i -%i %i -%i %i -%i imp:n=1
$ Outer Pressure Vessel
\n',ci+14,totdens_Inco718,s_bot5,s_top5,410,412,si0+3,si+9)
    else
        fprintf(fid,'%i 8 %2.4s %i -%i %i -%i %i -%i imp:n=1
$ Fixed large reflector segment
\n',ci+7,totdens_Be,s_bot1,s_top1,s_in1,s_out1,si+17,si+11)
        fprintf(fid,'%i 0 %i -%i %i -%i %i -%i imp:n=1
$ Large reflector segment axial gap 1
\n',ci+8,s_bot2,s_top2,s_in1,s_out1,si+17,si+11)
        fprintf(fid,'%i 8 %2.4s %i -%i %i -%i %i -%i imp:n=1
$ Moving large reflector segment
\n',ci+9,totdens_Be,s_bot3,s_top3,s_in1,s_out1,si+17,si+11)

```

```

        fprintf(fid, '%i  0          %i -%i %i -%i %i -%i          imp:n=1
$ Large reflector segment axial gap 2
\n', ci+10, s_bot4, s_top4, s_in1, s_out1, si+17, si+11)
        fprintf(fid, '%i  0          %i -%i %i -%i %i -%i %i %i %i %i
imp:n=1 $ Large reflector gap
\n', ci+11, s_bot5, s_top5, s_in2, s_out2, si+16, si+10, ci+7, ci+8, ci+9, ci+10)
        fprintf(fid, '%i 9  %1.4s %i -%i %i -%i %i -%i %i %i %i %i
%i imp:n=1 $ Large case
\n', ci+12, totdens_SS316, s_bot5, s_top5, s_in3, s_out3, si+15, si+9, ci+7, ci+8
, ci+9, ci+10, ci+11)
        fprintf(fid, '%i  7  %2.4s %i -%i %i -%i %i -%i          imp:n=1
$ Inner Pressure Vessel
\n', ci+13, totdens_Inco718, s_bot5, s_top5, 403, 405, si+15, si+9)
        fprintf(fid, '%i  7  %2.4s %i -%i %i -%i %i -%i          imp:n=1
$ Outer Pressure Vessel
\n', ci+14, totdens_Inco718, s_bot5, s_top5, 410, 412, si+15, si+9)
    end
    ci = ci + 15;
    si = si + 12;
end
% % LOOP TO DEFINE PRESSURE VESSEL
% m = 1; % loop counter
% fprintf(fid, '150  6 -%2.4f 100 -107 403 -412 \n', rho_Be)
% fprintf(fid, '          %i', ci0)
% for j = ci0+1:ci-1
%     if m > 8
%         fprintf(fid, ' %i\n', j)
%         fprintf(fid, '          ')
%         m = 0;
%     else
%         fprintf(fid, ' %i', j)
%     end
%     m = m+1;
% end
% fprintf(fid, ' imp:n=1 \n')
fprintf(fid, '200  0          -100:412 imp:n=0  $
Particle Killer 1 \n')
% fprintf(fid, '201  0          412 imp:n=0  $
Particle Killer 2 \n')
fprintf(fid, '202  0          403 -412 107  imp:n=0  $
Particle Killer 3 \n')
fprintf(fid, '203  0          -403 106  imp:n=0  $ Particle
Killer 4 \n')

%%%%%%%%%%%%%%%%%%%%%%%%%%%%%%%%%%%%%%%%%%%%%%%%%%%%%%%%%%%%%%%%%%%%%%%%
%%%%%%%%%%%%%%%%%%%%%%%%%%%%%%%%%%%%%%%%%%%%%%%%%%%%%%%%%%%%%%%%%%%%%%%% SURFACE CARD %%%%%%%%%%%%%%%%%%%%%%%%%%%%%%%%%%%%%%%%%%%%%%%%%%%%%%%%%%%%%%%%%%%%%%%%%
%%%%%%%%%%%%%%%%%%%%%%%%%%%%%%%%%%%%%%%%%%%%%%%%%%%%%%%%%%%%%%%%%%%%%%%%
fprintf(fid, '\nC SURFACE
CARD***** \n')
fprintf(fid, '100      pz 00.0000          $ Bottom of core \n')
fprintf(fid, '101      pz 21.4312          $ Interface: W & Mo elements
p116\n')
fprintf(fid, '102      pz 42.8625          $ Top of fueled core p116\n')

```

```

fprintf(fid,'103      pz 21.5900          $ Top of fixed rad ref p120\n')
fprintf(fid,'104      pz %2.4f          $ Bottom of moving rad ref
\n',21.5900+gap_radref)
fprintf(fid,'105      pz %2.4f          $ Top of moving rad ref
p120\n',43.18000+gap_radref)
fprintf(fid,'106      pz 53.0225          $ Top of axial reflector
p116\n')
fprintf(fid,'107      pz 65.2936          $ Top of radial reflector casing
and pressure vessel p116\n')

fprintf(fid,'200      cz %2.4f          $ Coolant channel radius p116
\n',r_ch)
fprintf(fid,'201      cz %2.4f          $ Coolant channel clad outer
radius \n',r_ch+t_ch_clad)
fprintf(fid,'202      cz %2.4f          $ Axial ref coolant channel
radius p116 \n',r_ch_ref)
fprintf(fid,'203      cz %2.4f          $ Axial ref coolant channel clad
outer radius \n',r_ch_ref+t_ch_clad)

fprintf(fid,'300      RHP 0 0 0          0 0 42.8625  %1.4f 0 0  $
Coolant channel pattern hexagonal prism \n',p_ch/2)
fprintf(fid,'301      RHP 0 0 0          0 0 42.8625  0 %1.4f 0  $
Extent of channels hexagonal prism \n',F2F_w/2)
fprintf(fid,'302      RHP 0 0 0          0 0 21.4312  0 %1.4f 0  $ W
element outer hexagonal prism \n',F2F_w/2)
fprintf(fid,'303      RHP 0 0 0          0 0 21.4312  0 %1.4f 0  $ W
element cladding outer hex prism \n',F2F_fuel/2)
fprintf(fid,'304      RHP 0 0 0          0 0 21.4312  0 %1.4f 0  $ W
element outer gap \n',F2F_gap/2)
fprintf(fid,'305      RHP 0 0 0          0 0 21.4312  0 %1.4f 0  $ W
element outer grid \n',F2F_gap/2+t_grid/2+m)
fprintf(fid,'306      RHP 0 0 21.4312  0 0 42.8625  0 %1.4f 0  $
Mo element outer hex prism \n',F2F_fuel/2)
fprintf(fid,'307      RHP 0 0 21.4312  0 0 42.8625  0 %1.4f 0  $
Mo element outer gap \n',F2F_gap/2)
fprintf(fid,'308      RHP 0 0 21.4312  0 0 42.8625  0 %1.4f 0  $
Mo element outer grid \n',F2F_gap/2+t_grid/2+m)
fprintf(fid,'309      RHP 0 0 42.8625    0 0 46.8625  0 %1.4f 0  $
Axial ref element outer hex prism \n',F2F_fuel/2)
fprintf(fid,'310      RHP 0 0 42.8625    0 0 46.8625  0 %1.4f 0  $
Axial ref element outer gap \n',F2F_gap/2)
fprintf(fid,'311      RHP 0 0 42.8625    0 0 46.8625  0 %1.4f 0  $
Axial ref element outer grid \n',F2F_gap/2+t_grid/2+m)
fprintf(fid,'312      RHP 0 0 0          0 0 42.8625  0 %1.4f 0  $
Infinite outer grid \n',F2F_gap/2+t_grid/2)
fprintf(fid,'313      RHP 0 0 42.8625    0 0 46.8625  %1.4f 0 0  $
Axial coolant channel pattern hexagonal prism \n',p_ch_ref/2)
fprintf(fid,'314      RHP 0 0 42.8625    0 0 46.8625  0 %1.4f 0  $
Extent of axial ref channels hexagonal prism \n',F2F_w/2)
fprintf(fid,'315      RHP 0 0 42.8625    0 0 46.8625  0 %1.4f 0  $
Infinite outer grid for axial ref \n',F2F_gap/2+t_grid/2)

```

```

fprintf(fid,'400      cz %2.4f          $ Support grid inner radius \n',
r_core)
fprintf(fid,'401      cz %2.4f          $ Support grid outer radius \n',
r_grid)
fprintf(fid,'402      cz %2.4f          $ Coolant tubes inner radius \n',
r_in_tubes)
fprintf(fid,'403      cz %2.4f          $ Inner pressure vessel inner
radius \n', r_in_ipv)
fprintf(fid,'404      cz %2.4f          $ Inner pressure vessel outer
radius \n', r_in_ipv+t_ipv)
fprintf(fid,'405      cz %2.4f          $ Inner reflector case inner
radius \n', r_in_casel)
fprintf(fid,'406      cz %2.4f          $ Inner reflector case outer
radius \n', r_in_casel+t_case)
fprintf(fid,'407      cz %2.4f          $ Reflector inner radius \n',
r_in_ref)
fprintf(fid,'408      cz %2.4f          $ Reflector outer radius \n',
r_in_ref+t_ref)
fprintf(fid,'409      cz %2.4f          $ Outer reflector case inner
radius \n', r_in_case2)
fprintf(fid,'410      cz %2.4f          $ Outer reflector case outer
radius \n', r_in_case2+t_case)
fprintf(fid,'411      cz %2.4f          $ Outer pressure vessel inner
radius \n', r_in_opv)
fprintf(fid,'412      cz %2.4f          $ Outer pressure vessel outer
radius \n', r_in_opv+t_opv)

% LOOP TO DEFINE REFLECTOR SURFACES
si = si0;
for k = 1:n
    fprintf(fid,'C *****SHIM NUMBER %i ***** \n', k)
    fprintf(fid,'%i      p %1.4f %1.4f %1.4f %1.4f $ Plane 1a \n', si,
A1a(k), B1a(k), C1a(k), D1a(k))
    fprintf(fid,'%i      p %1.4f %1.4f %1.4f %1.4f $ Plane 1b \n', si+1,
A1a(k), B1a(k), C1a(k), D1b(k))
    fprintf(fid,'%i      p %1.4f %1.4f %1.4f %1.4f $ Plane 1c \n', si+2,
A1a(k), B1a(k), C1a(k), D1c(k))
    fprintf(fid,'%i      p %1.4f %1.4f %1.4f %1.4f $ Plane 1d \n', si+3,
A1a(k), B1a(k), C1a(k), D1d(k))
    fprintf(fid,'%i      p %1.4f %1.4f %1.4f %1.4f $ Plane 1e \n', si+4,
A1a(k), B1a(k), C1a(k), D1e(k))
    fprintf(fid,'%i      p %1.4f %1.4f %1.4f %1.4f $ Plane 1f \n', si+5,
A1a(k), B1a(k), C1a(k), D1f(k))
    fprintf(fid,'%i      p %1.4f %1.4f %1.4f %1.4f $ Plane 2a \n', si+6,
A2a(k), B2a(k), C2a(k), D2a(k))
    fprintf(fid,'%i      p %1.4f %1.4f %1.4f %1.4f $ Plane 2b \n', si+7,
A2a(k), B2a(k), C2a(k), D2b(k))
    fprintf(fid,'%i      p %1.4f %1.4f %1.4f %1.4f $ Plane 2c \n', si+8,
A2a(k), B2a(k), C2a(k), D2c(k))
    fprintf(fid,'%i      p %1.4f %1.4f %1.4f %1.4f $ Plane 2d \n', si+9,
A2a(k), B2a(k), C2a(k), D2d(k))
    fprintf(fid,'%i      p %1.4f %1.4f %1.4f %1.4f $ Plane 2e \n', si+10,
A2a(k), B2a(k), C2a(k), D2e(k))

```

```

    fprintf(fid, '%i    p %1.4f %1.4f %1.4f %1.4f $ Plane 2f \n', si+11,
A2a(k), B2a(k), C2a(k), D2f(k))
    si = si + 12;
end

%%%%%%%%%%%%%%%%%%%%%%%%%%%%%%%%%%%%%%%%%%%%%%%%%%%%%%%%%%%%%%%%%%%%%%%%
%%%%%%%%%%%%%%%%%%%%%%%%%%%%%%%%%%%%%%%%%%%%%%%%%%%%%%%%%%%%%%%%%%%%%%%% DATA CARD %%%%%%%%%%%%%%%%%%%%%%%%%%%%%%%%%%%%%%%%%%%%%%%%%%%%%%%%%%%%%%%%%%%%%%%%%
%%%%%%%%%%%%%%%%%%%%%%%%%%%%%%%%%%%%%%%%%%%%%%%%%%%%%%%%%%%%%%%%%%%%%%%%
fprintf(fid, '\nC DATA
CARD***** \n')
fprintf(fid, 'C Source Definition-----
----- \n')
fprintf(fid, 'Mode N \n')
fprintf(fid, 'kcode 1000 1.0 50 1000 \n')
fprintf(fid, 'ksrc 0.11 0.11 20 \n')
fprintf(fid, 'C Materials Card-----
----- \n')
fprintf(fid, 'C All cross sections evaluated at room temperature. \n')
fprintf(fid, 'm1    1001.70c 1.0    $ Hydrogen \n')
fprintf(fid, 'm2    74000.55d 1.0    $ Tungsten cladding \n')
fprintf(fid, 'm3    92235.66c %1.4s 92238.66c %1.4s 8016.66c %1.4s \n',
0.93*atdens_U, 0.07*atdens_U, atdens_O)
fprintf(fid, '    64000.35d %1.4s 42000.66c %1.4s    $ Mo-UO2
fuel    \n', atdens_Gd, atdens_Mo) % Note: check the enrichment
of Gd-157
fprintf(fid, 'm4    92235.66c %1.4s 92238.66c %1.4s 8016.66c %1.4s \n',
0.93*atdens_U, 0.07*atdens_U, atdens_O)
fprintf(fid, '    64000.35d %1.4s 74000.55d %1.4s    $ W-UO2
fuel    \n', atdens_Gd, atdens_W)
fprintf(fid, 'm5    4009.66c %1.4s 8016.66c %1.4s    $ BeO \n',
atdens_Be_ax, atdens_O_ax)
fprintf(fid, 'mt5    be/o.15t
$ Be S(alpha,beta) for BeO \n')
fprintf(fid, 'm6    74000.55d %1.4s 75185.70c %1.4s 75187.70c %1.4s    $
W-Re \n', atdens_W_clad, 0.374*atdens_Re_clad, 0.626*atdens_Re_clad)
fprintf(fid, 'm7    6000.70c %1.4s 28000.50d %1.4s 24000.50d %1.4s \n',
atdens_C_inc, atdens_Ni_inc, atdens_Cr_inc)
fprintf(fid, '    13027.70c %1.4s 26000.55d %1.4s 41093.70c %1.4s
\n', atdens_Al_inc, atdens_Fe_inc, atdens_Nb_inc)
fprintf(fid, '    22000.66c %1.4s 14000.60c %1.4s    $ Inconel-718
\n', atdens_Ti_inc, atdens_Si_inc)
fprintf(fid, 'm8    4009.66c 1.0
$ Be \n')
fprintf(fid, 'mt8    be.64t
$ S(alpha,beta) \n')
fprintf(fid, 'm9    6000.70c %1.4s 24000.50d %1.4s 28000.50d %1.4s \n',
atdens_C_ss, atdens_Cr_ss, atdens_Ni_ss)
fprintf(fid, '    42000.66c %1.4s 14000.60c %1.4s 15031.70c %1.4s
\n', atdens_Mo_ss, atdens_Si_ss, atdens_P_ss)
fprintf(fid, '    26000.55d %1.4s 25055.70c %1.4s 16000.66c %1.4s    $
SS-316 Cladding \n', atdens_Fe_ss, atdens_Mn_ss, atdens_S_ss)

% Turn off delayed neutrons

```

```

fprintf(fid,'c totnu no \n')

% Mesh Tallies
fprintf(fid,'C Tally Mesh \n')
fprintf(fid,'c tmesh \n')
fprintf(fid,'c cmesh13 \n')
fprintf(fid,'c cora13 0 20i 35 \n')      % r
fprintf(fid,'c corb13 0 15i 46.8625 \n') % z
fprintf(fid,'c corc13 360 \n')          % theta
fprintf(fid,'c endmd \n')
fprintf(fid,'tmesh \n')
fprintf(fid,'rmesh3 mfact -1 %8f \n', multiplier)
fprintf(fid,'cora3 0 3i -10.715 \n')    % x
fprintf(fid,'corb3 0 6i 21.43 \n')     % y
fprintf(fid,'corc3 0 15i 42.8625 \n')  % z
fprintf(fid,'endmd \n')

% fprintf(fid,'FMESH4:N GEOM=CYL      ORIGIN= 0 0 %1.4f \n',9)
% fprintf(fid,'          IMESH= %1.4f          IINTS=30 \n',r_pv)
% fprintf(fid,'          JMESH= %1.4f          JINTS=20 \n',30)
% fprintf(fid,'          KMESH= 1              KINTS=1 \n')
% fprintf(fid,'FM4 -%1.4s 0 -6 \n',Q*2.523e6)

fclose('all');

```

Inputs.m

```

function complete = Inputs()
% Brad Appel
% Inputs for MCNP Input Deck Generator
% Based on the ANL 10 klf-thrust NTR
% Texas A&M University
%%%%%%%%%%%%%%%%%%%%%%%%%%%%%%%%%%%%%%%%%%%%%%%%%%%%%%%%%%%%%%%%%%%%%%%%
%% Inputs.m %%
% This code specifies all geometry and material inputs for generating
the
% MCNP script for the ANL-10K NTR reactor.

matname = 'Inputs.mat';

%%%%%%%%%%%%%%%%%%%%%%%%%%%%%%%%%%%%%%%%%%%%%%%%%%%%%%%%%%%%%%%%%%%%%%%%
%% TALLY MULTIPLIER %%
%%%%%%%%%%%%%%%%%%%%%%%%%%%%%%%%%%%%%%%%%%%%%%%%%%%%%%%%%%%%%%%%%%%%%%%%
power = 212;          % [MW] - Reactor power
nubar = 2.523;       % [] - avg fast neutrons produced per
fission
E_fis = 192.9;      % [MeV] - energy deposited in material per
fission
multiplier = 100^3*power*nubar/E_fis; % conversion multiplier from
MeV/cc to MW/m^3

```

```

%%%%%%%%%%%%%%%%%%%%%%%%%%%%%%%%%%%%%%%%%%%%%%%%%%%%%%%%%%%%%%%%%%%%%%%%
%%% GEOMETRY  %%%
%%%%%%%%%%%%%%%%%%%%%%%%%%%%%%%%%%%%%%%%%%%%%%%%%%%%%%%%%%%%%%%%%%%%%%%%
cm = 2.54;                                     % convert inches to cm

%%%%%%%%%%%%%%%%%%%%%%%%%%%%%%%%%%%%%%%%%%%%%%%%%%%%%%%%%%%%%%%%%%%%%%%%
%%% MAIN REACTIVITY VARIABLE
%%%%%%%%%%%%%%%%%%%%%%%%%%%%%%%%%%%%%%%%%%%%%%%%%%%%%%%%%%%%%%%%%%%%%%%%
gap_radref = 6.854;                            % [cm] - **Gap between fixed and moving
radial reflector - **cannot be exactly zero
% maximum withdrawal is about 21.275 cm

%%%%%%%%%%%%%%%%%%%%%%%%%%%%%%%%%%%%%%%%%%%%%%%%%%%%%%%%%%%%%%%%%%%%%%%%
%%% Fuel Elements
r_ch = 0.067*cm/2;                             % [cm] - coolant channel inner radius -
Ref 1 p116
r_ch_ref = 0.218*cm/2;                         % [cm] - axial reflector coolant channel
inner radius - Ref 1 p116
t_ch_clad = 0.005*cm;                          % [cm] - coolant channel cladding
thickness (assume 0.005")
p_ch = 0.136*cm;                               % [cm] - triangular lattice pitch for
coolant channels - Ref 1 p116
p_ch_ref = 0.4*cm;                             % [cm] - lattice pitch for axial ref
coolant channels - Ref 1 guess to fit 7
F2F_W = 1.068*cm;                             % [cm] - W element flat-to-flat - Ref 1
p117
F2F_fuel = 1.082*cm;                          % [cm] - fuel element flat-to-flat (Mo or
clad) - Ref 1 p116
F2F_gap = 1.092*cm;                          % [cm] - gap flat-to-flat - Ref 1 p116
t_grid = 0.050*cm;                          % [cm] - support grid web thickness - CAD
model

%%%%%%%%%%%%%%%%%%%%%%%%%%%%%%%%%%%%%%%%%%%%%%%%%%%%%%%%%%%%%%%%%%%%%%%%
%%% Support Grid, Coolant Tubes, and Pressure Vessels
r_core = 8.437*cm;                             % [cm] - outer radius of fueled core -
p113
r_grid = 8.562*cm;                             % [cm] - outer radius of support grid -
p113
r_in_tubes = 8.750*cm;                        % [cm] - inner radius of cooling tubes -
p113
r_in_ipv = 8.950*cm;                          % [cm] - inner radius inner pressure
vessel - p113
t_ipv = 0.125*cm;                             % [cm] - wall thickness of inner pressure
vessel - p113
r_in_case1 = 9.102*cm;                       % [cm] - inner radius of inner reflector
case wall - p113
r_in_ref = 9.194*cm;                          % [cm] - inner radius of reflector - p113
t_ref = 4.000*cm;                             % [cm] - thickness of reflector - p113
r_in_case2 = 13.221*cm;                      % [cm] - inner radius of outer reflector
case wall - p113
t_gap = 0.027*cm;                             % [cm] - gap between reflector case and
reflector - p113
t_case = 0.065*cm;                          % [cm] - wall thickness of reflector case
- p113

```

```

r_in_opv = 13.313*cm;      % [cm] - inner radius of outer pressure
vessel - p113
t_opv = 0.187*cm;        % [cm] - wall thickness of outer pressure
vessel - p113
n = 6;                    %      - number of shim reflector sections

```

```

%%%%%%%%%%%%%%%%%%%%%%%%%%%%%%%%%%%%%%%%%%%%%%%%%%%%%%%%%%%%%%%%%%%%%%%%
%%% MATERIAL PROPERTIES %%%
%%%%%%%%%%%%%%%%%%%%%%%%%%%%%%%%%%%%%%%%%%%%%%%%%%%%%%%%%%%%%%%%%%%%%%%%

```

```

%%% Composition Fractions

```

```

%%%%%%%% Fuel

```

```

v_UO2 = 0.6000;          % [] - volumetric fraction of UO2 in fuel
v_W = 0.3391;           % [] - volumetric fraction of W in W element
v_Mo = 0.3391;          % [] - volumetric fraction of Mo in Mo element
v_Gd2O3 = 0.0609;       % [] - volumetric fraction of gadolinia in fuel
element

```

```

%%%%%%%% Cladding and Support Grid

```

```

v_W_clad = 0.75;        % [] - volumetric fraction of tungsten
v_Re_clad = 0.25;       % [] - volumetric fraction of rhenium
v_W_chan = 1.0;         % [] - volumetric fraction of tungsten in channel
coating

```

```

%%%%%%%% Reflectors

```

```

a_Be_ax = 0.5;          % [] - atomic fraction of Be in BeO
a_O_ax = 0.5;           % [] - atomic fraction of O in BeO
a_Be_rad = 1.0;         % [] - atomic fraction of Be in Be
f_ref = 0.70;           % [] - solid fraction of radial reflector (due to
coolant channels) - Ref 1

```

```

%%%%%%%% Inconel 718

```

```

a_C_inc = 0.001;        % [] - atomic fraction of C in Inco-718 - Ref 2
a_Ni_inc = 0.55;        % [] - atomic fraction of Ni in Inco-718 - Ref 2
a_Cr_inc = 0.21;        % [] - atomic fraction of Cr in Inco-718 - Ref 2
a_Ti_inc = 0.0115;     % [] - atomic fraction of Ti in Inco-718 - Ref 2
a_Al_inc = 0.0080;     % [] - atomic fraction of Al in Inco-718 - Ref 2
a_Fe_inc = 0.125;       % [] - atomic fraction of Fe in Inco-718 - Ref 2
a_Nb_inc = 0.055;       % [] - atomic fraction of Nb in Inco-718 - Ref 2
a_Si_inc = 0.035;       % [] - atomic fraction of Si in Inco-718 - Ref 2

```

```

%%%%%%%% Stainless Steel 316

```

```

a_C_ss = 0.0008;        % [] - atomic fraction of C in SS-316 - Ref 2
a_Cr_ss = 0.17;         % [] - atomic fraction of Cr in SS-316 - Ref 2
a_Ni_ss = 0.12;         % [] - atomic fraction of Ni in SS-316 - Ref 2
a_Mn_ss = 0.02;         % [] - atomic fraction of Mn in SS-316 - Ref 2
a_Mo_ss = 0.025;        % [] - atomic fraction of Mo in SS-316 - Ref 2
a_Si_ss = 0.01;         % [] - atomic fraction of Si in SS-316 - Ref 2
a_P_ss = 0.00045;       % [] - atomic fraction of P in SS-316 - Ref 2
a_S_ss = 0.0003;        % [] - atomic fraction of S in SS-316 - Ref 2
a_Fe_ss = 1 - a_C_ss - a_Cr_ss - a_Ni_ss - a_Mn_ss - a_Mo_ss - a_Si_ss - a_P_ss -
a_S_ss;                 % [] - atomic fraction of Fe in SS-316

```

```

%%% Densities

```

```

%%%%%%%% Fuel

```

```

rho_UO2 = 10.960;       % [g/cc] - Ref 2

```

```

rho_W = 19.3;          % [g/cc] - Ref 2
rho_Mo = 10.200;      % [g/cc] - Ref 2
rho_Gd2O3 = 7.07;    % [g/cc] - Wikipedia
rho_H2 = 0.00234;    % [g/cc] - Ideal gas at 700 psi, 500 K
%%%%%%%% Cladding and Support Grid
rho_Re = 21.02;      % [g/cc] - Wikipedia
%%%%%%%% Reflectors
rho_BeO = 3.010;     % [g/cc] - Ref 2
rho_Be = 1.848;      % [g/cc] - Ref 2
rho_B4C = 2.510;     % [g/cc] - Ref 2
%%%%%%%% Inconel 718
rho_Inco718 = 8.2209; % [g/cc] - Ref 4
%%%%%%%% Stainless Steel 316
rho_SS316 = 7.99;    % [g/cc] - Ref 5

%%% Molecular Weights
%%%%%%%% Fuel
MW_UO2 = 267.253;    % [g/mol] - molecular weight of 90% enr UO2 -
Ref 3 & Wikipedia
MW_W = 183.84;       % [g/mol] - molecular weight of W - Wikipedia
MW_Mo = 95.962;      % [g/mol] - molecular weight of Mo - Wikipedia
MW_Gd2O3 = 362.483; % [g/mol] - molecular weight of Gadolinium
Oxide - Wikipedia
%%%%%%%% Cladding and Support Grid
MW_Re = 186.207;     % [g/mol] - molecular weight of Re - Wikipedia
%%%%%%%% Reflectors
MW_Be = 9.012182;    % [g/mol] - molecular weight of Be - Wikipedia
MW_BeO = 25.01;      % [g/mol] - Wikipedia
MW_B4C = 55.24;      % [g/mol] - molecular weight of B4C - Ref 2
%%%%%%%% Inconel 718
MW_C = 12.01078;     % [g/mol] - molecular weight of C - Wikipedia
MW_Ni = 58.69344;    % [g/mol] - molecular weight of Ni - Wikipedia
MW_Cr = 51.9961;     % [g/mol] - molecular weight of Cr - Wikipedia
MW_Ti = 47.867;      % [g/mol] - molecular weight of Ti - Wikipedia
MW_Al = 26.9815;     % [g/mol] - molecular weight of Al - Wikipedia
MW_Fe = 55.8452;     % [g/mol] - molecular weight of Fe - Wikipedia
MW_Nb = 92.90638;    % [g/mol] - molecular weight of Nb - Wikipedia
MW_Si = 28.0855;     % [g/mol] - molecular weight of Si - Wikipedia
MW_Inco718 = a_C_inc*MW_C + a_Ni_inc*MW_Ni + a_Cr_inc*MW_Cr +
a_Ti_inc*MW_Ti + a_Al_inc*MW_Al + a_Fe_inc*MW_Fe + a_Nb_inc*MW_Nb +
a_Si_inc*MW_Si;      % [g/mol] - molecular weight of Inconel 718
%%%%%%%% Stainless Steel 316
MW_Mn = 54.938045;   % [g/mol] - molecular weight of Mn - Wikipedia
MW_P = 30.973762;    % [g/mol] - molecular weight of P - Wikipedia
MW_S = 32.0655;      % [g/mol] - molecular weight of S - Wikipedia
MW_SS316 = a_C_inc*MW_C + a_Cr_ss*MW_Cr + a_Ni_ss*MW_Ni + a_Mn_ss*MW_Mn
+ a_Mo_ss*MW_Mo + a_Si_ss*MW_Si + a_P_ss*MW_P + a_S_ss*MW_S;    %
[g/mol] - molecular weight of Inconel 718

%%% Caclulations
N = 6.0221415e23;    % [at/mol] - Avagadro's number
%%%%%%%% Fuel

```

```

atdens_U = v_UO2*rho_UO2*N / (MW_UO2*10^24);
% [at/barn-cm] - atom density of U
atdens_O = 2*v_UO2*rho_UO2*N / (MW_UO2*10^24);
% [at/barn-cm] - atom density of O
atdens_W = v_W*rho_W*N / (MW_W*10^24);
% [at/barn-cm] - atom density of W
atdens_Mo = v_Mo*rho_Mo*N / (MW_Mo*10^24);
% [at/barn-cm] - atom density of W
atdens_Gd = 2*v_Gd2O3*rho_Gd2O3*N / (MW_Gd2O3*10^24);
% [at/barn-cm] - atom density of Gd
atdens_O = atdens_O + 3*v_Gd2O3*rho_Gd2O3*N / (MW_Gd2O3*10^24);
% [at/barn-cm] - atom density of O (from UO2 and Gd2O3 combined)
totdens_WUO2 = atdens_U + atdens_O + atdens_W + atdens_Gd;
% [at/barn-cm] - total atom density for WUO2 fuel
totdens_MoUO2 = atdens_U + atdens_O + atdens_Mo + atdens_Gd;
% [at/barn-cm] - total atom density for MoUO2 fuel
%%%%%%%% Cladding and Support Grid
atdens_W_clad = v_W_clad*rho_W*N / (MW_W*10^24);
% [at/barn-cm] - atom density of W in clad
atdens_Re_clad = v_Re_clad*rho_Re*N / (MW_Re*10^24);
% [at/barn-cm] - atom density of Re in clad
totdens_WRe = atdens_W_clad + atdens_Re_clad;
% [at/barn-cm] - total atom density for W-Re clad/grid
totdens_W_chan = v_W_chan*rho_W*N / (MW_W*10^24);
% [at/barn-cm] - atom density of W in channel coating
%%%%%%%% Reflectors
atdens_Be_ax = a_Be_ax*rho_BeO*N / (MW_BeO*10^24);
% [at/barn-cm] - atom density of Be in BeO reflector
atdens_O_ax = a_O_ax*rho_BeO*N / (MW_BeO*10^24);
% [at/barn-cm] - atom density of Be in BeO reflector
totdens_BeO = atdens_Be_ax + atdens_O_ax;
% [at/barn-cm] - total atom density for BeO reflector
totdens_Be = f_ref*(a_Be_rad*rho_Be*N / (MW_Be*10^24));
% [at/barn-cm] - atom density of Be in Be reflector
%%%%%%%% Inconel 718
atdens_C_inc = a_C_inc*rho_Inco718*N / (MW_Inco718*10^24);
% [at/barn-cm] - atom density of C in Inconel 718
atdens_Ni_inc = a_Ni_inc*rho_Inco718*N / (MW_Inco718*10^24);
% [at/barn-cm] - atom density of Ni in Inconel 718
atdens_Cr_inc = a_Cr_inc*rho_Inco718*N / (MW_Inco718*10^24);
% [at/barn-cm] - atom density of C in Inconel 718
atdens_Ti_inc = a_Ti_inc*rho_Inco718*N / (MW_Inco718*10^24);
% [at/barn-cm] - atom density of Ni in Inconel 718
atdens_Al_inc = a_Al_inc*rho_Inco718*N / (MW_Inco718*10^24);
% [at/barn-cm] - atom density of C in Inconel 718
atdens_Fe_inc = a_Fe_inc*rho_Inco718*N / (MW_Inco718*10^24);
% [at/barn-cm] - atom density of Ni in Inconel 718
atdens_Nb_inc = a_Nb_inc*rho_Inco718*N / (MW_Inco718*10^24);
% [at/barn-cm] - atom density of C in Inconel 718
atdens_Si_inc = a_Si_inc*rho_Inco718*N / (MW_Inco718*10^24);
% [at/barn-cm] - atom density of Ni in Inconel 718
totdens_Inco718 = atdens_C_inc + atdens_Ni_inc + atdens_Cr_inc +
atdens_Ti_inc + atdens_Al_inc + atdens_Fe_inc + atdens_Nb_inc +
atdens_Si_inc; % [at/barn-cm] - atom density of Inconel 718

```

```

%%%%%%%%% Stainless Steel 316
atdens_C_ss = a_C_ss*rho_SS316*N / (MW_SS316*10^24);
% [at/barn-cm] - atom density of C in Stainless Steel 316
atdens_Cr_ss = a_Cr_ss*rho_SS316*N / (MW_SS316*10^24);
% [at/barn-cm] - atom density of Cr in Stainless Steel 316
atdens_Ni_ss = a_Ni_ss*rho_SS316*N / (MW_SS316*10^24);
% [at/barn-cm] - atom density of Ni in Stainless Steel 316
atdens_Mn_ss = a_Mn_ss*rho_SS316*N / (MW_SS316*10^24);
% [at/barn-cm] - atom density of Mn in Stainless Steel 316
atdens_Mo_ss = a_Mo_ss*rho_SS316*N / (MW_SS316*10^24);
% [at/barn-cm] - atom density of Mo in Stainless Steel 316
atdens_Si_ss = a_Si_ss*rho_SS316*N / (MW_SS316*10^24);
% [at/barn-cm] - atom density of Si in Stainless Steel 316
atdens_P_ss = a_P_ss*rho_SS316*N / (MW_SS316*10^24);
% [at/barn-cm] - atom density of P in Stainless Steel 316
atdens_S_ss = a_S_ss*rho_SS316*N / (MW_SS316*10^24);
% [at/barn-cm] - atom density of S in Stainless Steel 316
atdens_Fe_ss = a_Fe_ss*rho_SS316*N / (MW_SS316*10^24);
% [at/barn-cm] - atom density of Fe in Stainless Steel 316
totdens_SS316 = atdens_C_ss + atdens_Cr_ss + atdens_Ni_ss +
atdens_Mn_ss + atdens_Mo_ss + atdens_Si_ss + atdens_P_ss + atdens_S_ss
+ atdens_Fe_ss; % [at/barn-cm] - atom density of SS 316

save(matname,
'r_ch','r_ch_ref','t_ch_clad','p_ch','p_ch_ref','F2F_W','F2F_fuel','F2F
_gap','t_grid', ...

'r_core','r_grid','r_in_tubes','r_in_ipv','t_ipv','r_in_case1','r_in_re
f','t_ref','r_in_case2','t_gap','t_case','r_in_opv','t_opv', ...
'gap_radref','n','multiplier', ...

'rho_H2','atdens_U','atdens_O','atdens_W','atdens_Mo','atdens_Gd','todd
ens_WUO2','totdens_MoUO2', ...
'atdens_W_clad','atdens_Re_clad','totdens_WRe','totdens_W_chan',
...
'atdens_Be_ax','atdens_O_ax','totdens_BeO','totdens_Be', ...

'atdens_C_inc','atdens_Ni_inc','atdens_Cr_inc','atdens_Ti_inc','atdens_
Al_inc','atdens_Fe_inc','atdens_Nb_inc','atdens_Si_inc','totdens_Inco71
8', ...

'atdens_C_ss','atdens_Cr_ss','atdens_Ni_ss','atdens_Mn_ss','atdens_Mo_s
s','atdens_Si_ss','atdens_P_ss','atdens_S_ss','atdens_Fe_ss','totdens_S
S316');

complete = 1;

%%%%%%%%%
%%% REFERENCES %%%
%%%%%%%%%
% 1. Argonne National Lab Nuclear Rocket Program Terminal Report, ANL-
7236
% 2. 2008 IAEA Thermophysical Properties of Reactor Materials

```



```

x1 = 0; % Point 1 on center axis
y1 = 0;
z1 = 0;
x2 = 0; % Point 2 on center axis
y2 = 0;
z2 = 1;
x3_1a = cos(theta-sweep); % Point 3 at edge of reflector shim
y3_1a = sin(theta-sweep);
z3_1a = 0;
A1a(i)=y1*(z2-z3_1a)+y2*(z3_1a-z1)+y3_1a*(z1-z2);
B1a(i)=z1*(x2-x3_1a)+z2*(x3_1a-x1)+z3_1a*(x1-x2);
C1a(i)=x1*(y2-y3_1a)+x2*(y3_1a-y1)+x3_1a*(y1-y2);
D1a(i)=(x1*(y2*z3_1a-y3_1a*z2)+x2*(y3_1a*z1-y1*z3_1a)+x3_1a*(y1*z2-
y2*z1));

%%% Shift the 1a plane
%%%%%%%%%%%%%%%%%%%%%%%%%%%%%%%%%%%%%%%%%%%%%%%%%%%%%%%%%%%%%%%%%%%%%%%%%;

% Plane 1b
D1b(i) = D1a(i) + t_gap;

% Plane 1c
D1c(i) = D1a(i) + t_gap + t_case;

% Plane 1d
D1d(i) = D1a(i) + t_gap + t_case + t_web;

% Plane 1e
D1e(i) = D1a(i) + t_gap + t_case + t_web + t_case;

% Plane 1f
D1f(i) = D1a(i) + t_gap + t_case + t_web + t_case + t_gap;

%%%%%%%%%%%%%%%%%%%%%%%%%%%%%%%%%%%%%%%%%%%%%%%%%%%%%%%%%%%%%%%%%%%%%%%%%
%%% 2a Plane
%%%%%%%%%%%%%%%%%%%%%%%%%%%%%%%%%%%%%%%%%%%%%%%%%%%%%%%%%%%%%%%%%%%%%%%%%
x1 = 0; % Point 1 on center axis
y1 = 0;
z1 = 0;
x2 = 0; % Point 2 on center axis
y2 = 0;
z2 = 1;
x3_2a = cos(theta+sweep); % Point 3 at edge of reflector shim
y3_2a = sin(theta+sweep);
z3_2a = 0;
A2a(i)=y1*(z2-z3_2a)+y2*(z3_2a-z1)+y3_2a*(z1-z2);
B2a(i)=z1*(x2-x3_2a)+z2*(x3_2a-x1)+z3_2a*(x1-x2);
C2a(i)=x1*(y2-y3_2a)+x2*(y3_2a-y1)+x3_2a*(y1-y2);
D2a(i)=(x1*(y2*z3_2a-y3_2a*z2)+x2*(y3_2a*z1-y1*z3_2a)+x3_2a*(y1*z2-
y2*z1));

%%% Shift the 2a plane

```

```

%%%%%%%%%%%%%%%%%%%%%%%%%%%%%%%%%%%%%%%%%%%%%%%%%%%%%%%%%%%%%%%%%%%%%%%%

% Plane 1b
D2b(i) = D2a(i) - t_gap;

% Plane 1c
D2c(i) = D2a(i) - t_gap - t_case;

% Plane 1d
D2d(i) = D2a(i) - t_gap - t_case - t_web;

% Plane 1e
D2e(i) = D2a(i) - t_gap - t_case - t_web - t_case;

% Plane 1f
D2f(i) = D2a(i) - t_gap - t_case - t_web - t_case - t_gap;
end

% Save to a mat file
save(matname, 'A1a', 'B1a', 'C1a', 'D1a', 'D1b', 'D1c', 'D1d', 'D1e',
'D1f', ...
'A2a', 'B2a', 'C2a', 'D2a', 'D2b', 'D2c', 'D2d', 'D2e', 'D2f');

complete = 1;

```

Example Input Deck for Parametric Study

Simplified W-UO2 NTR Model

C Cell Card*****

```

1 1 -2.3400e-003          -200    u=1 imp:n=1 $ Coolant channel
2 2 6.3222e-002          200 -201    u=1 imp:n=1 $ Coolant Channel cladding
3 3 6.9469e-002          201 -101    u=1 imp:n=1 $ WUO2 channel section
4 4 7.2478e-002          201 101     u=1 imp:n=1 $ BeO channel section
5 0          -301 304 -300 303 -305 302 lat=2 fill=1 u=2 imp:n=1 $ Channels Lattice Cell
6 0          -400 100 -102 fill=2    imp:n=1    $ Channels Window - filling core
7 5 8.6441e-002          400 -401 100 -101    imp:n=1    $ Radial Reflector
8 0          401:-100:102          imp:n=0    $ Particle Killer 1
9 0          400 -401 101 -102          imp:n=0    $ Particle Killer 2

```

C SURFACE CARD*****

```

100 pz 00.0000          $ Bottom of core
101 pz 37.2000          $ Top of core
102 pz 57.2000          $ Top of axial reflector
200 cz 9.0000e-002      $ Coolant channel radius p116
201 cz 1.0778e-001      $ Coolant channel clad outer radius

```

300 p 1 1.73205 0 3.7800e-001
 301 px 1.8900e-001
 302 p -1 1.73205 0 -3.7800e-001
 303 p 1 1.73205 0 -3.7800e-001
 304 px -1.8900e-001
 305 p -1 1.73205 0 3.7800e-001
 400 cz 18.6000 \$ Core radius
 401 cz 36.6000 \$ Reflector outer radius

C DATA CARD*****

C Source Definition-----

Mode N

kcode 8000 1.0 50 300

ksrc 0.11 0.11 20

C Materials Card-----

C All cross sections evaluated at room temperature.

m1 1001.70c 1.0 \$ Hydrogen

m2 74000.55d 1.0 \$ Tungsten cladding

m3 92235.66c 1.3803e-002 92238.66c 1.0150e-003 8016.66c 3.1782e-002

64000.35d 1.4306e-003 74000.55d 2.1439e-002 \$ W-UO2 fuel

m4 4009.66c 3.6239e-002 8016.66c 3.6239e-002 \$ BeO

mt4 be.o.15t \$ Be S(alpha,beta) for BeO

m5 4009.66c 1.0 \$ Be

mt5 be.64t \$ S(alpha,beta)

C Tally Mesh

FMESH4:N GEOM=REC ORIGIN= 0 -1 0 OUT ik

IMESH= 18.6000 IINTS=20

JMESH= 1

KMESH= 37.2 KINTS=20

FM4 -1.238E15 3 -6

VITA

Name: Brad Appel

Address: Department of Nuclear Engineering
Texas A&M University
3133 TAMU
College Station, TX 77843

Email Address: bradcappel@gmail.com

Education: B.A., Aeronautical and Astronautical Engineering, Purdue University,
2009
M.S., Nuclear Engineering, Texas A&M University, 2012